DISSERTATION

UNDERSTANDING STRUCTURE PROPERTY RELATIONSHIPS IN NIOBIUM OXIDE BASED MATERIALS FOR HIGH-RATE ANODES

Submitted by

Luke David Salzer

Department of Chemistry

In partial fulfillment of the requirements

For the Degree of Doctor in Philosophy

Colorado State University

Fort Collins, Colorado

Fall 2024

Doctoral Committee:

Advisor: Justin Sambur

Yuyang Dong
Chuck Henry
Chris Weinberger

ABSTRACT

UNDERSTANDING STRUCTURE PROPERTY RELATIONSHIPS IN NIOBIUM–BASED OXIDES FOR HIGH-RATE ANODES

With the growing usage of portable electronic devices, electric vehicles, and grid level storage, a diverse set of energy storage devices is required for each application. Current commercial level lithium-ion batteries commonly utilize graphite as the anode material. While graphite possesses impressive energy storage, graphite struggles with high (dis)charge applications. One class of materials of interest to replace graphite are niobium-based oxides, some of which fall into a group of materials called Wadsley-Roth crystallographic shear compounds. Wadsley-Roth (W-R) compounds possess unit cells with *nxm* blocks of edge-shared octahedra, which boast high-rate capabilities, having higher volumetric capacities than graphite at various (dis)charge rates. While various (W-R) compositions of have been synthesized and their electrochemical properties explored, the origin of the excellent rate capabilities and capacities is unclear. Herein, niobium-based anodes for high-rate lithium-ion batteries are investigated to understand the structure-property relationships in W-R materials with different block sizes, levels of disorder, and composition. Additionally, a niobium oxide polymorph falls into a unique class of energy storage materials called pseudocapacitors, which possess high energy density while the charge storage mechanism mimics that of a capacitor. Sections of this work describe current and future investigations of pseudocapacitive niobium oxide to better understand the origin of this interesting material.

Chapter 1 begins with a brief introduction, background, and motivation on the need for high-rate, high-capacity anode materials as an alternative for graphite, to address the growing need for high-power, high-energy density materials. Chapter II describes the synthesis of three structurally similar W-R compounds with different block sizes and investigates the electrochemical performance of each material. Chapters III and IV investigate methods to improve the electrochemical performances of W-R compositions through defects and dopants. Chapter V investigates the pseudocapacitive niobium oxide that also exhibits high-rate capabilities through a process called pseudocapacitance, in which the material possesses electrochemical characteristic similar to both batteries and capacitors. In the final chapter, Chapter VI, concludes the dissertation by describing further directions necessary to better understand the structure property relationships resulting in high-rate, high-capacity niobium-based oxide anodes.

ACKNOWLEDGMENTS

First and foremost, I would like to thank several undergraduate students that have assisted in the work presented here. The first undergraduate I had the pleasure of working with, Brian Diamond, was invaluable in introducing me to the field of batteries. My second and third undergraduate students, Cami Christensen and Claire Gervais, taught me how to be a better mentor and teacher. The days in lab listening to Taylor Swift or playing homemade bingo in the office made the long trek that is graduate school much more enjoyable. I am proud of the work we have done together and know you two will continue to grow into excellent scientists and mentors.

To Dakota Lorenz, Garrett Hotelling, Alex Green, and Macayla Barnes; I would not have had the strength to continue graduate school without your support, both academically and personally. These 5 years have been filled with countless memories and adventures, both good and bad, with even the bad/rainy adventures having a silver lining.

To my lovely girlfriend, Francis Luong, I am continuously in awe of your positivity. Every day with you is a gift and a am eternally grateful for your constant support, even if you fall asleep during my late-night practice talks.

To my family and friends, thank you for shaping me into who I am today outside of the lab. I am in debt to everyone who has asked how I am doing or how graduate school was going. Allowing me to think of anything else but research or graduate school helped me get through it all. I want to thank my parents, sister, and brother-in-law for all the support, cards, and care-packages sent to me over the years and always rooting for me.

To the amazing individuals working in both the Prieto and Neilson groups, thank you for allowing me to work in your labs, ask science questions, and joke around with you all. Specifically,

Dan Windsor, Nathan Nessius, Monika Perez, Kelly Nieto, Brennan McBride, and Thinh Tran, for mentoring me, learning with me, and letting me bounce ideas off each of you on questions I had in lab and life. The spirit of collaboration at Colorado State University made the research presented here both easier and more enjoyable to complete.

Additionally, I would like to thank collaborators from Lehigh University, for their work on the preliminary computational Raman in Chapter III, I truly appreciate all the hard work you all have done.

Next, I want to thank my advisor and mentor, Dr. Justin Sambur. You invited me into your group when my rotations didn't pan out. You adapted a project to better fit my research interests and walked the fine line between challenging me and driving me further and deeper into the science and supporting me when research and the program almost broke me down. Thank you for everything.

To the past and present members of the Sambur group, thank you for all the memories and events. From group breakfasts to champagne in the office, from enjoying relaxing teatimes, yelling and bickering on the West side of the office (the better side), working and learning with all of you has been an interesting and rewarding experience. I want to shout out Rafael Almaraz for being my intramurals soccer captain, weightlifting coach, and Marmot regular with me; as well as stealing all your friends. I'd like to thank those that came before me, Dr. Evans, Dr. Nilsson, Dr. Van Erdewyk, Dr. Toole, and Dr. Banik for all that you have done, proving the quote outside our building by Sir Isaac Newton "If I have seen further than others, it is by standing upon the shoulders of giants".

DEDICATION

This work is dedicated to those in the acknowledgements, as well as my friends and family for their love and support.

To my sister, Dr. Allyson Salzer-Bobka, you were always one step ahead of me in most aspects of life, except for height and comedy, you gave me something to chase after and a challenge to overcome.

To my father and mother, Mark and Jodi Salzer, you two were my first teachers and mentors, instilling a passion for knowledge and learning that led me to pursue an advanced degree. Thank you for all the lessons you tried to teach me, even if I still can't change my oil, I will learn one of these days.

Again, to my lovely girlfriend, Francis Luong, knowing you are always here for me when the research didn't go right and when I went weeks without a success. Your positive attitude was a godsend and got me through. I knew you'd be at home ready to listen to what I did well or wrong. Thank you for everything.

TABLE OF CONTENTS

CHAPTER I: INTRODUCTION, BACKGROUND, AND MOTIVATION FOR NIOBIUM BASED ANODE MATERIALS[1]

1.1 Niobium Oxide Based Anodes for High-Rate Energy Storage

The growing adoption of renewable energy generation technology demands efficient energy storage and rapid delivery systems. To facilitate the transition to a renewable energy-based economy, it is essential to develop new materials capable of storing large quantities of charge with high energy density and delivering it rapidly with high power. Commercial batteries often use graphite as the anode material, but graphite has a significant drawback: lithium tends to deposit on its surface at high (dis)charge rates. This can lead to the growth of lithium dendrites during repeated cycling, which poses a risk of short-circuiting the cell and causing explosions.[3,4] Fundamental research on design principles for safe, high-rate anode materials is crucial. One alternative to graphite anodes is metal oxides, which possess high working potentials (>1 V vs. Li/Li+) that avoid dendrite formation at high rates.[5,6] Among transition metal oxides, niobium oxide-based anodes are particularly promising for replacing graphite. Specifically, niobium-based Wadsley-Roth (W-R) crystallographic shear compounds and the pseudocapacitive T-Nb_2O_5 are materials of interest. W-R shear compounds are of interest because they possess fast Li-ion diffusion coefficients (D_{Li+}), some of which are two orders of magnitude larger than commercialized $Li_4Ti_5O_{12}$ (LCO), allowing for fast (dis)charge rates.[7,8] Lastly, the power density of un-optimized W-R compounds is greater than that of optimized graphite and can exhibit multi-electron reduction (greater than 1 Li^+/transition metal), resulting in capacities greater than theoretically predicted.

---

[1] This chapter is intended to motivate the work in this dissertation. Portions of this chapter are adapted from a National Science Foundation grant (DMR-2046948), cowritten with Luke D. Salzer, Dakota B. Lorenz, R. Colby Evans, Brian Diamond, and Justin B. Sambur.

T-Nb_2O_5 is a material of interest because it falls into a unique class of materials called pseudocapacitors, which are materials that behave like capacitors, while the charge storage mechanism is Faradaic in nature, such as a battery.[9–17] These materials store charge in the bulk of the material, resulting in improved energy density, with a charge storage mechanism not limited by solid-state diffusion, allowing for faster (dis)charge rates. While these materials possess an interesting charge storage mechanism, the exact definition of what makes a material pseudocapacitive is still unclear. Fundamental questions relating to this class of materials include how much charge, and on what time scale is charge inserted into the bulk of material in a rate that is not diffusion limited?

The following sections will further describe the structures of W-R compounds and T-Nb_2O_5, as well as further literature hypotheses on the origins of the impressive electrochemical properties present in both. Additionally, a section will provide a dissertation overview of the research presented in this work.

1.2 Structure-Property Relationships in Wadsley-Roth Crystallographic Shear Anodes

Wadsley-Roth materials were investigated extensively in 1965 when the structural motif of several compounds was uncovered.[18–24] W-R shear structures form $n \times m$ blocks of octahedra with the block edges being linked through edge shared octahedra, and the block center connected through corner shared octahedra. These blocks extend indefinitely in the direction perpendicular to the block plane, with some structures possessing tetrahedral sites on the block corners to fill void spaces, as shown in Figure 1.1. Additionally, work done by Cava et al. investigated several W-R materials and found that lithium can be chemically inserted into the unit cell, setting the stage for electrochemical investigations of these materials.[25]

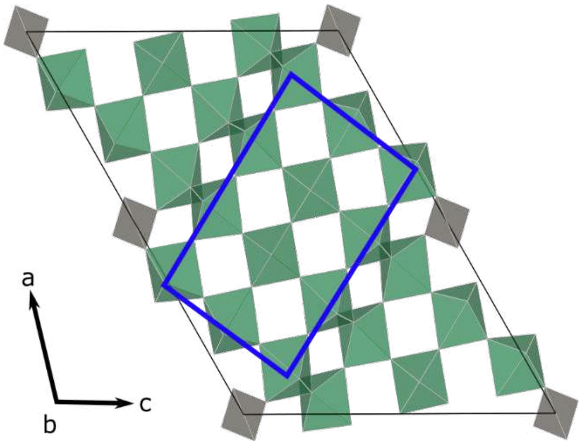

Figure 1.1. Unit cell of $Nb_{12}WO_{33}$, green and grey polyhedra represent niobium octahedra and tungsten tetrahedral coordination environments respectfully. The blue box highlights the 3×4 block size.

While W-R shear structures have been known since the 1960's and that it was possible for lithium to be inserted in these materials since the 1980's, it was not until 2018 that they were shown to be impressive energy storage materials.[7] The material investigated was $Nb_{16}W_5O_{55}$, which possesses approximately 225 mAh/g at a C-rate of C/5, or current rate corresponding to a 5-hour (dis)charge, and exhibited high-rate capabilities storing 171 mAh/g 5C (12 minute (dis)charge) and 148 mAh/g at 20C (3 minute (dis)charge). This fast (dis)charge in $Nb_{16}W_5O_{55}$, is due to high Li-ion diffusion coefficients of approximately 2.1×10^{-12} m^2s^{-1}, and low activation energies of approximately 0.23 eV between lithium storage sites.[7] Figure 1.2 shows a Ragone plot presenting the energy density and power density for $Nb_{16}W_5O_{55}$ and graphite, illustrating the high-energy and high-rate capabilities of W-R materials.

This research sparked a dramatic increase in publications assessing the high-rate capabilities of W-R. Recent work has shown that W-R materials possess compositional freedom, with publications on Ti-Nb-O, Nb-O, Nb-W-O, V-Nb-O, and other systems.[26–33] Many of these possess different block sizes, with $TiNb_2O_7$, $Nb_{12}WO_{33}$, and $H\text{-}Nb_2O_5$ possessing 3×3, 3×4, and

3x4 and 3×5 blocks respectively. Since each of these materials have similar structural features, all belonging to W-R compounds, they each possess impressive electrochemical properties, each storing approximately 225 mAh/g at a C-rate of 1C.[26,29,34] Furthermore, W-R phases exhibit many low energy Li-ion storage sites within the unit cells. Li-ions can easily travel between Li-ion storage sites due to low activation energies between storage sites, resulting in fast Li-ion diffusion and diffusion coefficients on the order of $1x10^{-12}$ to $1x10^{-11}$ m^2/s, comparable with current solid-state electrolytes[26,29,34–36]

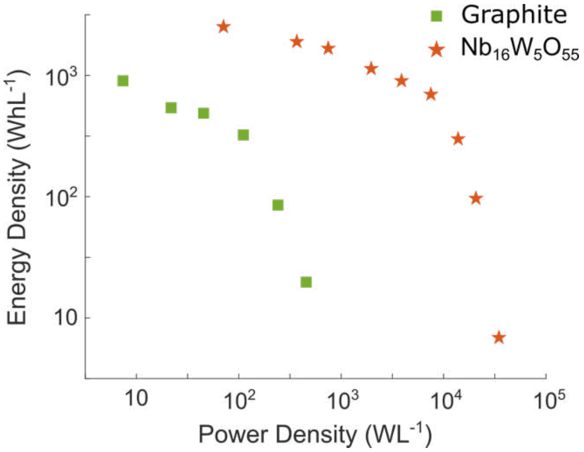

Figure 1.2. Ragone plot comparing the electrochemical performances of graphite and the W-R crystallographic shear material, $Nb_{16}W_5O_{55}$. (Figure adapted with permission from *Nature* **2018**, *559* (7715), 556–563. Copyright 2018, Macmillan Publishers Ltd., part of

While each of these materials has been shown to store large amounts of lithium and electrons, some materials have been shown to store more than the predicted theoretical capacity, which is 1 Li/electron per transition metal. This property is of significant interest because if a transition metal can be reduced multiple times, it would result in higher energy densities. While this electrochemical property has been known in W-R compounds for years, the exact structural motif allowing for multi-electron redox is unknown. Recent work has shown that isostructural PNb_9O_{25} and VNb_9O_{25} possess significantly different electrochemical signatures with just one elemental change, with the structures being shown in Figure 1.3.[37] Specifically, PNb_9O_{25} was found to possess a larger capacity than VNb_9O_{25}, exhibiting multi-electron redox even with the non-redox active phosphorous being present in the unit cell, with PNb_9O_{25} storing 230 mAh/g compared to 175 mAh/g found with VNb_9O_{25} at a C-rate of C/10. Interestingly, when cycled at a slower C-rate of C/20, VNb_9O_{25} can insert more lithium than PNb_9O_{25}, storing approximately 13.5 and 10.3 lithium ions per unit cell on the first discharge respectively. However, upon cycle two, the number of lithium ions inserted in VNb_9O_{25} drops by more than 3, indicating irreversible reduction of vanadium and niobium. This indicates that atomic substitutions in the unit cell may be a method to optimize electrochemical properties.

Moving from atomic substitutions altering the electrochemistry of W-R compounds, the edge-sharing octahedra along the shear plane plays a significant role in the electrochemical properties of certain W-R compounds. Often, the octahedra occupying sites along the shear plane are more distorted than the corner-sharing octahedra in the block center. Once lithiated, the edge-sites undergo structural changes which results in a decrease in the degree of distortions.[38,39] This structural rearrangement can lead to the unit cell parameter perpendicular to the block plane expanding with inserted Li-ions, while the block plane initially expands, then contracts, and then expands again. These lattice parameter contractions result in a near-negligible volume expansion, resulting in low mechanical stress when lithiated, aiding in cycle stability and reversibility. Additionally, recent work has shown that upon lithiation, the metal centers in the edge-sharing sites structural changes results in *d* orbital overlap.[39] This orbital overlap may cause metal-metal bond formation, lowering the energy states of the traditionally non-bonding t_{2g} orbitals forming new, more stable molecular orbitals. The formation and role metal-metal bonding plays on the electrochemical performance in transition metal oxides is an interesting question to explore and may help explain the excellent electrochemical performance of W-R shear compounds.

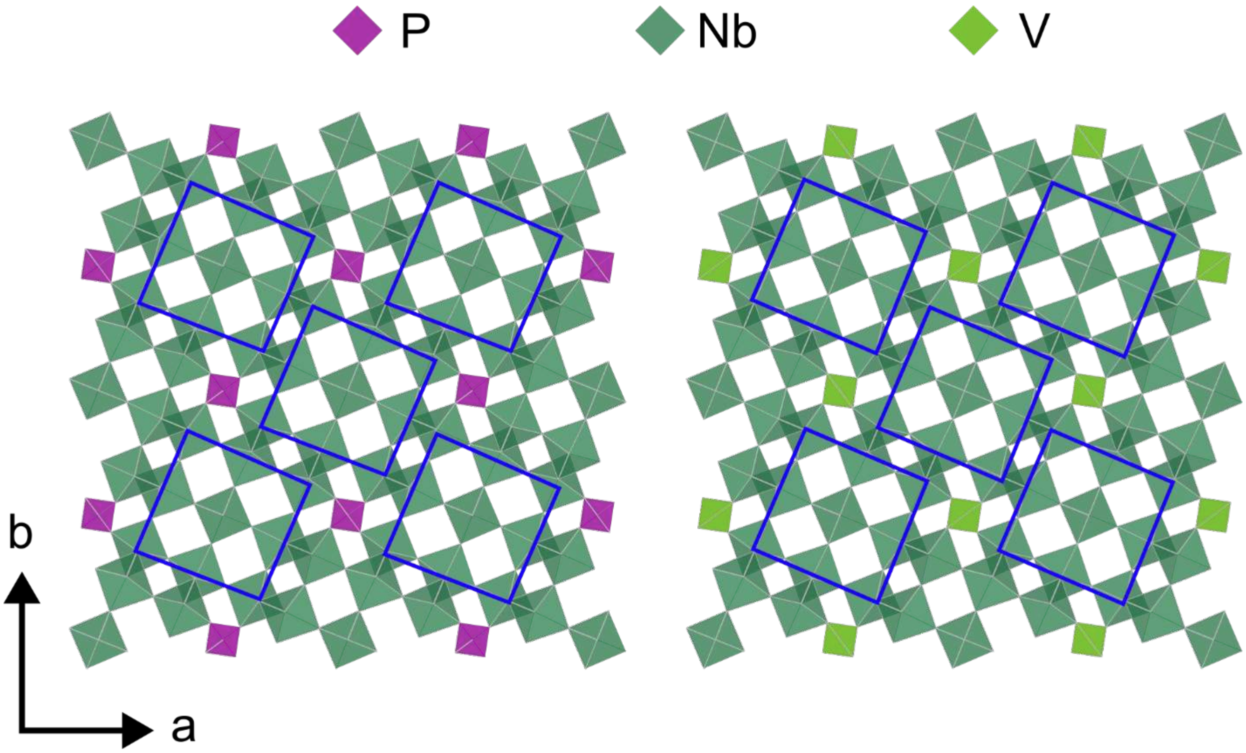

Figure 1.3. Super cells of PNb_9O_{25} and VNb_9O_{25} with phosphorous and vanadium occupying the tetrahedral sites, blue blocks highlight the 3×3 block size.

While W-R crystallographic shear compounds all possess similar structure motifs, there are some structural differences present in the Nb-W-O class of W-R materials. In this group, there have been significant investigations on the 3×4 $Nb_{12}WO_{33}$, 4×4 $Nb_{14}W_3O_{44}$, and 4×5 $Nb_{16}W_5O_{55}$ structures shown in Figure 1.4. As the block size increases, the probability of W occupancy changes, with each composition exhibiting a preference for tungsten occupying the tetrahedral position on the block edges. However, both the 4×4 and 4×5 block sizes show a probability of W occupancy in the block center. Griffith et al. conducted ex-situ X-ray absorption spectroscopy at different levels of lithiation for the 4x5 and found a slight initial preference for tungsten reduction at low levels of lithiation, followed by a monotonic change in the oxidation state of both niobium and tungsten upon further lithiation. Due to W occupying both the block center and tetrahedral sites in the 4x5, the order of reduction as well as lithium site occupancy in these larger block sizes is still unclear, as is the role the tetrahedral site plays.

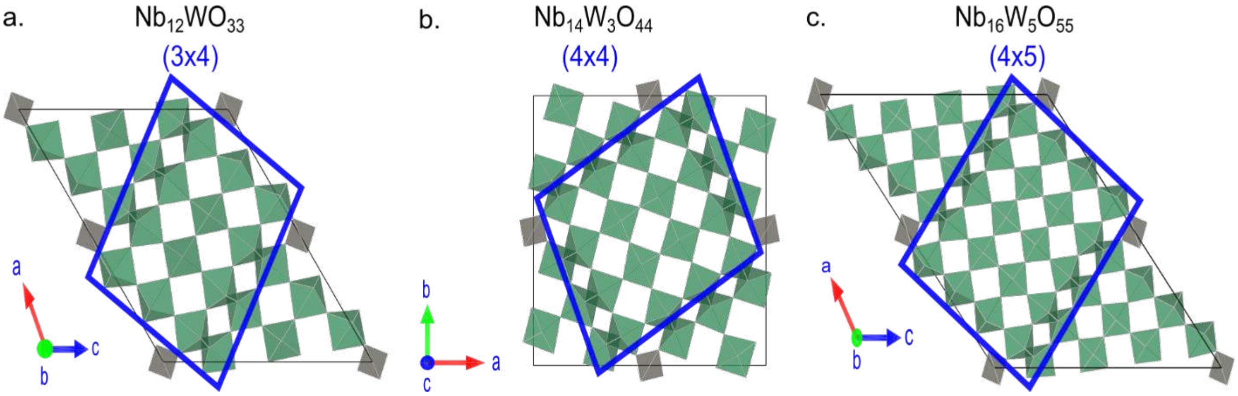

Figure 1.4. Unit cells of (a) $Nb_{12}WO_{33}$, (b) $Nb_{14}W_3O_{44}$, and (c) $Nb_{16}W_5O_{55}$, the blue blocks highlight the 3×4, 4×4, and the 4×5 block sizes respectfully. Figure reused with permission *ACS Appl. Energy Mater.* 2023, 6, 3, 1685–1691, Copyright 2023 American Chemical Society

With the understanding that W-R crystallographic shear compounds possess impressive energy densities and power densities, the motivation to conduct fundamental research to understand the origin behind these properties is clear. In the work presented here, we conduct research to better understand the structure property relationships owing to the fast lithium-ion diffusion, high capacity, and cyclability these materials possess.

1.3 Defining and Understanding Pseudocapacitance

Current electrochemical energy storage materials generally fall within two categories, electric double layer capacitors (EDLCs) or batteries. Figure 1.5 shows a Ragone plot for various electrochemical energy storage technologies, plotting the rate of energy output (as power density, y axis) vs the total energy available (energy density, x axis). EDLC's and other capacitors possess high-power densities, showing they can deliver high (dis)charge rates. This is because capacitive charge storage occurs at surface sites, not limited by solid-state diffusion. Batteries have high energy density because their charge storage mechanism utilizes Faradaic or redox reactions throughout the bulk of the material. However, storing charge in the active materials results in lower (dis)charge rates due to slow solid-state diffusion of inserted ions. Ideally, next generation energy storage materials would possess properties of both capacitors and batteries, possessing high power and energy.

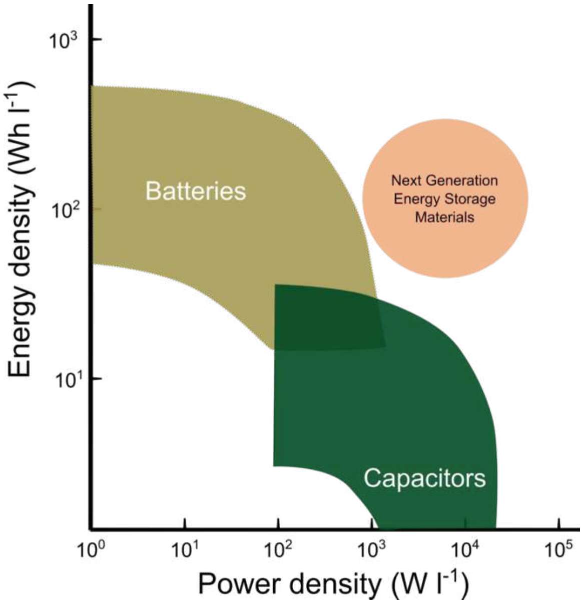

Figure 1.5. Ragone plot comparing the EDLC and battery performance. Figure adapted with permission from *ACS Energy Lett.* 2017, 2, 2581-2590, Copyright 2017 American Chemical Society

Pseudocapacitive materials are of interest for these next generation electrochemical energy storage systems because they possess both high-energy through the reduction of the system through faradaic charge transfer, as well high-rate charging due to the charge storage mechanism being non-diffusion limited, mimicking the electrochemical kinetics of a capacitors. There has been significant research in identifying materials that display pseudocapacitance, which can be an intrinsic feature to a material, such as RuO_2*nH_2O, MnO_2, and Nb_2O_5.[11,40–42] Furthermore, pseudocapacitance can be induced, known as an extrinsic pseudocapacitor through nanostructuring, where the increased surface area and smaller particle sizes results in decreased diffusion distances, allowing for faster charge storage through the following equation.[43–45]

$$\mathrm{t} = L^2/D_{Li+}$$

Where t is the time required to charge or discharge a particle, L is diffusion length, and D_{Li} is the lithium-ion diffusion coefficient. By nanoscaling the material, the diffusion length and time to (dis)charge decrease, resulting in higher power density.[46]

The work conducted by Conway et al. focused on investigating the electrochemistry of materials for energy storage and has helped provide the basis for the main method of stating if a material is pseudocapacitive or not.[14,47] This is through the examination of the scan-rate dependence of the current when running cyclic voltammetry experiments by deconvoluting the current response and surface limited (di/ds = constant = capacitance) or diffusion limited ($di/di^{1/2}$ = constant = battery). Additionally, a combination of these processes can occur, in which the current response is provided by $i(V) = k_1 v + k_2 v^{1/2}$, where k_1 and k_2 are constants, independent of scan rate and v is scan rate. This equation allows for identification of the charge storage mechanism, where a linear plot for $i(V)\ vs\ v$ would indicate surface limited processes, a linear plot for $i(V)\ vs\ v^{1/2}$ indicates a diffusion limited process.[47]

The work done by Dunn et al. attempted to examine the total charge from cyclic voltammetry through the extension of Conway et al, seminal work. [11,47,48] This breaks down the current contributions into the faradaic contribution as well as the non-faradaic or capacitive contribution, including the pseudocapacitive contribution through variable scan rate cyclic voltammetry, according to the following equation.[14,49]

$$i = av^b$$

Where i is peak current (anodic or cathodic peak), v is scan rate, and a and b are adjustable parameters, with the b value being calculated by taking the log of current (i) peak vs. the log of the scan rate (mV/s) shown in the following equation, and finding the slope of the line.

$$\log(i) = b \cdot \log(v) + \log(a)$$

In this analysis, surface limited (capacitor-like) kinetics results in a peak current that changes linearly with scan rate corresponding to a b-value of 1. For a b-value of 0.5, the peak currents are proportional to the square root of the scan rate (v), indicating that the current response is diffusion-limited (battery-like). Simply put, if the current peaks in a CV scale linearly with the scan rate, the material is described as a pseudocapacitor. This analysis is a relatively easy method of investigating if electrochemical energy storage materials exhibit pseudocapacitive properties, where iV curves possessing peaks indicative of charge transfer (redox) can have their charge storage mechanism evaluated. If the power law analysis shows that the b value is 1, the material of interest is storing charge in a non-diffusion limited (or capacitive) mechanism. This approach has been used in investigating a wide variety of materials and has greatly added to the field of pseudocapacitors.

However, while the power-law analysis can be a powerful tool in an electrochemist's toolbox, there are some issues with the widespread use of this technique to assess if a material is pseudocapacitive or not. One issue is an over assignment of materials into the pseudocapacitor class of materials. Commonly, the power-law analysis is conducted, and a b value between 1 (capacitive-like) and 0.5 (battery-like) is obtained, indicating a mix of both non-diffusion and diffusion-limited charge storage mechanisms are occurring. Often, if a material exhibits a b value greater than 0.5, it is assigned to be pseudocapacitive, diluting the class of materials and the definition of pseudocapacitance. Another issue is related to the time in which charge is stored, capacitors possess high-power and can be fully charged and discharged in a matter of seconds.[50] Often, the power-law analysis occurs in slow scan-rates taking minutes to hours to fully (dis)charge. This discrepancy between the time constraints has physical implications, where slow scan-rates may result in materials showing pseudocapacitance. An example of this is with $LiCoO_2$, which is a common cathode material originally researched by Nobel Laureate, John B. Goodenough. Aurbach et al. conducted slow scan rate CV and found that the prototypical battery material displayed current peaks that scaled linearly with scan rate, indicative of pseudocapacitance.[51] There lies the problem, simply because a material displays non-diffusion limited charge storage behavior, is it a pseudocapacitor if the scan rates it shows this phenomena are significantly slower than what it would take to (dis)charge a capacitor?

In addition to this question, there is discontent with the descriptions of the physical processes that occur for pseudocapacitive charge storage. With some proponents insisting that the classical definition of pseudocapacitance. Which is a linear dependence of the charge stored with changing potential in a potential window of interest, in which the charge storage is due to electron transfer mechanisms, and not the adsorption of ions in the electrochemical double layer.[9] Unfortunately, this definition as enlarged to cover other characteristics, some of which are provided below.

- Cyclic voltammetry (CV) experiment non-Faradaic or capacitive like current (i) scales linearly with the potential scan rate (v), while Faradaic, or diffusion-limited current scales linearly with $v^{1/2}$.[42,48]
- Galvanostatic or current controlled experiments, the potential vs capacity profile is linear in capacitive like systems, while diffusion-limited systems possess non-linear profiles with plateaus.[52]
- Impedance experiments a capacitor possess a vertically line in a Nyquist plot, where has more diffusion-limited processes possess deviations from this, with purely diffusion-limited charge storage kinetics exhibiting a 45-degree angle in a Nyquist plot.[13]

Through the utilization of the power-law analysis, the total current varies with scan-rate and implies that increase *v* drives the response toward the capacitive charge storage mechanism, which can be the case, shown in Figure 1.6.[53] However, what is assigned to be pseudocapacitive charge storage could also be associated with a cyclic voltammetry response due to ohmic drop, present in many semiconducting or insulating metal oxides, or slow charge transfer kinetics.[54–56] This indicates that the common power-law analysis can often be improperly utilized if other conditions previously mentioned occur, and that researchers should use caution when utilizing this common method to identify pseudocapacitive materials.

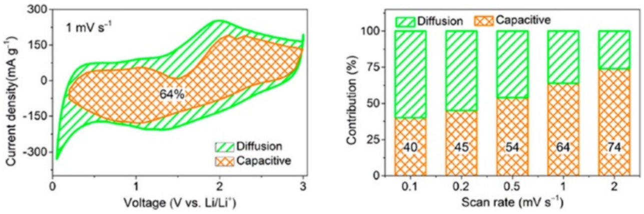

Figure 1.6. Kinetics analysis of the electrochemical behavior toward Li ions for the $NH_3{-}Ti_3C_2Tx$ electrode. electrode at various scan rates from 0.1 to 2 mV s−1. (a) Determination of capacitive contribution from the CV data. (b) Contribution percentage of capacitive (orange) and diffusion-controlled (green) capacities at different rates for $NH_3{-}Ti_3C_2Tx$. Figure reused with permission from *J. Phys. Chem. C* 2019, 123, 2, 1099–1109, Copyright 2018 American Chemical Society

Additionally, Costentin and Savéant have conducted significant research in better understanding the physical processes relating to surface limited, diffusion limited, and pseudocapacitive charge storage mechanisms.[55–57] One important addition was addressing the popular notion that pseudocapacitance arises from multiple faradaic redox processes with a distribution of potentials, resulting in the square, capacitive like cyclic voltammetry. Through their theoretical analysis, the CV responses never mimic a square CV as observed in experimental results and must be due in part to previously mentioned origins.

Overall, pseudocapacitors are a unique class of electrochemical energy storage materials because they can store a significant amount of charge in a short time. However, there are still unanswered questions on what a pseudocapacitor is, the timescales pseudocapacitance is present, and the physical and electrochemical processes occurring. In the work presented here, we attempt to help answer these questions.

1.4 Overview of the Following Dissertation Chapters

Herein, investigation on niobium oxide-based anodes for lithium-ion batteries reveals structure-property relationships and provides information on possible design principles for next generation, energy storage materials as well as contributes to fundamental understanding and descriptions of the electrochemical performances of these materials. The research presented here consists of understanding the role the block-size, crystallinity, and elemental composition plays in lithium diffusion, capacity stored, and cycle stability in W-R crystallographic shear compounds. Additionally, the work here helps clarify the definition of pseudocapacitors by providing descriptions for the electrochemical signatures through cyclic voltammetry.

In Chapter II, our work is aimed at identifying structure property relationships relating to block size in a series of structurally similar W-R crystallographic shear compounds. This work was published in American Chemical Society, Applied Energy Materials (Salzer, L. D.; Diamond, B.; Nieto, K.; Evans, R. C.; Prieto, A. L.; Sambur, J. B. Structure–Property Relationships in High-Rate Anode Materials Based on Niobium Tungsten Oxide Shear Structures. ACS Appl. Energy Mater. 2023, 6 (3), 1685–1691. https://doi.org/10.1021/acsaem.2c03573.) In this work, we synthesized $Nb_{12}WO_{33}$ (3×4), $Nb_{14}W_3O_{44}$ (4×4), and $Nb_{16}W_5O_{55}$ (4×5) via high temperature, solid-state reactions and fabricated coin cells for electrochemical testing. Through galvanostatic cycling and potentiostatic intermittent titration technique (PITT), the capacity stored, cyclability, and lithium-ion diffusivity were investigated. The results indicate that the symmetric, 4×4 compound stores the largest capacity despite having the second highest theoretical capacity and is more reversible. Additionally, PITT reveals that as you increase the block size, the number of low energy tunnels for lithium transport increases, resulting in an increase in lithium-ion diffusion coefficients, resulting in $Nb_{16}W_5O_{55}$ (4×5) possessing the best high-rate capabilities. Furthermore, $Nb_{12}WO_{33}$ (3×4), possessed both the lowest capacities and lithium-ion diffusivity, warranting further work to improve these electrochemical metrics.

Chapter III builds off the work in Chapter II, which attempted to improve the electrochemical performance of $Nb_{12}WO_{33}$. Two methods were attempted to improve the capacity of Nb_{12}WO33, first we systematically substituted molybdenum for tungsten in $Nb_{12}WO_{33}$, resulting in $Mo_xNb_{12}W_{1-x}O_{33}$. Second, we synthesized each substituted composition slowly to improve the crystallinity of the samples and quickly to introduce disorder. In this work we synthesized each sample with high temperature solid-state reactions and fabricated coin cells to test the electrochemistry of each sample. From the galvanostatic cycling we found that the introduction of molybdenum improved the capacity stored for both fast and slow samples. Additionally, each quickly synthesized sample possessed a statistically significantly improvement in capacity stored when compared their slowly synthesized counterparts. The work presented here is being prepared for publication.

Chapter IV is an extension of both Chapter II and III, where we similarly substituted molybdenum for tungsten in $Nb_{14}W_3O_{44}$ (4×4). These samples were made again through high temperature solid state reaction and coin cells were fabricated to assess the electrochemistry. The $Nb_{14}W_3O_{44}$ (4×4) sample is different than $Nb_{12}WO_{33}$ (3×4) through both the increased block size, as well as the interior of the block possessing cation disorder, with a probability of niobium or tungsten occupying different sites. The addition of molybdenum into the unit cell further adds to the structural complexity in which there is now a probability of molybdenum occupying the same sites. Through powder x-ray diffraction (PXRD) and Raman spectroscopy, we believe that both tungsten and molybdenum prefer the tetrahedral site in $Nb_{14}W_3O_{44}$ and $Mo_3Nb_{14}O_{44}$ respectfully. In addition, the Raman spectroscopy of mixed compositions, $MoNb_{14}W_2O_{44}$ and $Mo_2Nb_{14}WO_{44}$, reveals the molybdenum prefers the tetrahedral site over tungsten, hinting at preferential occupancies. Similarly to $Mo_xNb_{12}W_{1-x}O_{33}$, the introduction of molybdenum into $Mo_xNb_{14}W_{3-x}O_{44}$ results in an increase in capacity stored. The work presented here is being prepared for publication.

Chapter V focuses on adding to the current definition of pseudocapacitance. This was done by investigating the pseudocapacitive material, T-Nb_2O_5. T-Nb_2O_5 was synthesized through solid-state syntheses and coin cells were fabricated to test the electrochemistry. These cells were then cycled with slow scan rate cyclic voltammetry (SSCV) to probe the domains in which the charge-storage mechanism is surface-limited or diffusion-limited. SSCV reveals two important features, the first is that the peak separation between anodic and cathodic peaks was lower than predicted for an electrochemically reversible, Nernstian system, underlying the charge storage mechanism mimics that of a self-assembled monolayer. In these systems, the redox active material is chemically bound to the electronically conductive substrate, resulting in no diffusion processes. The second feature revealed through SSCV are peak features that have yet to be observed in previously reported literature, indicating that the electrochemical reduction and oxidation processes are more complex than believed.

The final chapter, Chapter VI, concludes the dissertation by describing further directions to continue understanding the structure property relationships in W-R crystallographic shear compounds and pseudocapacitive materials. Some examples of future research projects are provided here. For W-R materials, it was hypothesized the strength of Jahn-Teller distortions may play a role in the electrochemical performances in ternary metal oxides.[38] Previous work in Chapters III and IV have shown that molybdenum substitution (a stronger second order Jahn-Teller distorted than both niobium and tungsten) has improved the performance of both 3×4 $Nb_{12}WO_{33}$ and 4×4 $Nb_{14}W_3O_{44}$.[58] It would be interesting to systematically investigate the role distortions play on the electrochemistry of W-R materials. Moreover, it is hypothesized that metal-metal bonding can occur in W-R materials when lithiated.[39] A systematic investigation of the role the edge sites play would greatly improve the understanding of W-R compounds. To better understand pseudocapacitive materials, modeling each of the fundamental charge storage processes that could be occurring would greatly add to field. Understanding these fundamental processes and relationships, as well as developing tools, characterization techniques, and models to study niobium-based anode materials, will lay the foundation for next generation energy storage systems with high energy densities, and long cycle life.

1.5 References

(1) Burns, J. C.; Stevens, D. A.; Dahn, J. R. In-Situ Detection of Lithium Plating Using High Precision Coulometry. *J. Electrochem. Soc.* **2015**, *162* (6), A959. https://doi.org/10.1149/2.0621506jes.

(2) Downie, L. E.; Krause, L. J.; Burns, J. C.; Jensen, L. D.; Chevrier, V. L.; Dahn, J. R. In Situ Detection of Lithium Plating on Graphite Electrodes by Electrochemical Calorimetry. *J. Electrochem. Soc.* **2013**, *160* (4), A588. https://doi.org/10.1149/2.049304jes.

(3) Vetter, J.; Novák, P.; Wagner, M. R.; Veit, C.; Möller, K.-C.; Besenhard, J. O.; Winter, M.; Wohlfahrt-Mehrens, M.; Vogler, C.; Hammouche, A. Ageing Mechanisms in Lithium-Ion Batteries. *J. Power Sources* **2005**, *147* (1), 269–281. https://doi.org/10.1016/j.jpowsour.2005.01.006.

(4) Ribière, P.; Grugeon, S.; Morcrette, M.; Boyanov, S.; Laruelle, S.; Marlair, G. Investigation on the Fire-Induced Hazards of Li-Ion Battery Cells by Fire Calorimetry. *Energy Environ. Sci.* **2012**, *5* (1), 5271–5280. https://doi.org/10.1039/C1EE02218K.

(5) Ding, H.; Song, Z.; Zhang, H.; Zhang, H.; Li, X. Niobium-Based Oxide Anodes toward Fast and Safe Energy Storage: A Review. *Mater. Today Nano* **2020**, *11*, 100082. https://doi.org/10.1016/j.mtnano.2020.100082.

(6) Deng, Q.; Fu, Y.; Zhu, C.; Yu, Y. Niobium-Based Oxides Toward Advanced Electrochemical Energy Storage: Recent Advances and Challenges. *Small* **2019**, *15* (32), 1804884. https://doi.org/10.1002/smll.201804884.

(7) Griffith, K. J.; Wiaderek, K. M.; Cibin, G.; Marbella, L. E.; Grey, C. P. Niobium Tungsten Oxides for High-Rate Lithium-Ion Energy Storage. *Nature* **2018**, *559* (7715), 556–563. https://doi.org/10.1038/s41586-018-0347-0.

(8) Griffith, K. J.; Harada, Y.; Egusa, S.; Ribas, R. M.; Monteiro, R. S.; Von Dreele, R. B.; Cheetham, A. K.; Cava, R. J.; Grey, C. P.; Goodenough, J. B. Titanium Niobium Oxide: From Discovery to Application in Fast-Charging Lithium-Ion Batteries. *Chem. Mater.* **2021**, *33* (1), 4–18. https://doi.org/10.1021/acs.chemmater.0c02955.

(9) Brousse, T.; Bélanger, D.; Long, J. W. To Be or Not To Be Pseudocapacitive? *J. Electrochem. Soc.* **2015**, *162* (5), A5185–A5189. https://doi.org/10.1149/2.0201505jes.

(10) Augustyn, V.; Simon, P.; Dunn, B. Pseudocapacitive Oxide Materials for High-Rate Electrochemical Energy Storage. *Energy Environ. Sci.* **2014**, *7* (5), 1597–1614. https://doi.org/10.1039/C3EE44164D.

(11) Conway, B. E. *Electrochemical Supercapacitors: Scientific Fundamentals and Technological Applications*; Springer US, 1999. https://doi.org/10.1007/978-1-4757-3058-6.

(12) Simon, P.; Gogotsi, Y.; Dunn, B. Where Do Batteries End and Supercapacitors Begin? *Science* **2014**, *343* (6176), 1210–1211. https://doi.org/10.1126/science.1249625.

(13) Ko, J. S.; Sassin, M. B.; Rolison, D. R.; Long, J. W. Deconvolving Double-Layer, Pseudocapacitance, and Battery-like Charge-Storage Mechanisms in Nanoscale $LiMn_2O_4$ at 3D Carbon Architectures. *Electrochimica Acta* **2018**, *275*, 225–235. https://doi.org/10.1016/j.electacta.2018.04.149.

(14) Conway, B. E.; Birss, V.; Wojtowicz, J. The Role and Utilization of Pseudocapacitance for Energy Storage by Supercapacitors. *J. Power Sources* **1997**, *66* (1–2), 1–14. https://doi.org/10.1016/S0378-7753(96)02474-3.

(15) Conway, B. E.; Pell, W. G. Double-Layer and Pseudocapacitance Types of Electrochemical Capacitors and Their Applications to the Development of Hybrid Devices. *J. Solid State Electrochem.* **2003**, *7* (9), 637–644. https://doi.org/10.1007/s10008-003-0395-7.

(16) Wang, J.; Dong, S.; Ding, B.; Wang, Y.; Hao, X.; Dou, H.; Xia, Y.; Zhang, X. Pseudocapacitive Materials for Electrochemical Capacitors: From Rational Synthesis to Capacitance Optimization. *Natl. Sci. Rev.* **2017**, *4* (1), 71–90. https://doi.org/10.1093/nsr/nww072.

(17) Gogotsi, Y.; Penner, R. M. Energy Storage in Nanomaterials – Capacitive, Pseudocapacitive, or Battery-Like? *ACS Nano* **2018**, *12* (3), 2081–2083. https://doi.org/10.1021/acsnano.8b01914.

(18) Roth, R. S.; Wadsley, A. D. Multiple Phase Formation in the Binary System Nb_2O_5–WO_3. I. Preparation and Identification of Phases. *Acta Crystallogr.* **1965**, *19* (1), 26–32. https://doi.org/10.1107/S0365110X65002712.

(19) Roth, R. S.; Wadsley, A. D. Multiple Phase Formation in the Binary System Nb_2O_5–WO_3. II. The Structure of the Monoclinic Phases $WNb_{12}O_{33}$ and $W_5Nb_{16}O_{55}$. *Acta Crystallogr.* **1965**, *19* (1), 32–38. https://doi.org/10.1107/S0365110X65002724.

(20) Roth, R. S.; Wadsley, A. D. Multiple Phase Formation in the Binary System Nb_2O_5–WO_3. III. The Structures of the Tetragonal Phases $W_3Nb_{14}O_{44}$ and $W_8Nb_{18}O_{69}$. *Acta Crystallogr.* **1965**, *19* (1), 38–42. https://doi.org/10.1107/S0365110X65002736.

(21) Roth, R. S.; Wadsley, A. D. Multiple Phase Formation in the Binary System Nb_2O_5–WO_3. IV. The Block Principle. *Acta Crystallogr.* **1965**, *19* (1), 42–47. https://doi.org/10.1107/S0365110X65002748.

(22) Andersson, S.; Mumme, W. G.; Wadsley, A. D. Multiple Phase Formation in the Binary System Nb_2O_5–WO_3. V. The Structure of $W_4Nb_{26}O_{77}$, an Ordered Intergrowth of the Adjoining Compounds $WNb_{12}O_{33}$ and $W_3Nb_{14}O_{44}$. *Acta Crystallogr.* **1966**, *21* (5), 802–808. https://doi.org/10.1107/S0365110X66003852.

(23) Allpress, J. G.; Sanders, J. V.; Wadsley, A. D. Multiple Phase Formation in the Binary System Nb_2O_5–WO_3. VI. Electron Microscopic Observation and Evaluation of Non-Periodic Shear Structures. *Acta Crystallogr. B* **1969**, *25* (6), 1156–1164. https://doi.org/10.1107/S0567740869003669.

(24) Allpress, J. G.; Wadsley, A. D. Multiple Phase Formation in the Binary System Nb_2O_5-WO_3 VII. Intergrowth of H-Nb_2O_5 and $WNb_{12}O_{33}$. *J. Solid State Chem.* **1969**, *1* (1), 28–38. https://doi.org/10.1016/0022-4596(69)90005-X.

(25) Cava, R. J. Lithium Insertion in Wadsley-Roth Phases Based on Niobium Oxide. *J. Electrochem. Soc.* **1983**, *130* (12), 2345. https://doi.org/10.1149/1.2119583.

(26) Griffith, K. J.; Seymour, I. D.; Hope, M. A.; Butala, M. M.; Lamontagne, L. K.; Preefer, M. B.; Koçer, C. P.; Henkelman, G.; Morris, A. J.; Cliffe, M. J.; Dutton, S. E.; Grey, C. P. Ionic and Electronic Conduction in $TiNb_2O_7$. *J. Am. Chem. Soc.* **2019**, *141* (42), 16706–16725. https://doi.org/10.1021/jacs.9b06669.

(27) Griffith, K. J.; Senyshyn, A.; Grey, C. P. Structural Stability from Crystallographic Shear in TiO_2-Nb2O$_5$ Phases: Cation Ordering and Lithiation Behavior of $TiNb_{24}O_{62}$. *Inorg. Chem.* **2017**, *56* (7), 4002–4010. https://doi.org/10.1021/acs.inorgchem.6b03154.

(28) Li, T.; Nam, G.; Liu, K.; Wang, J.-H.; Zhao, B.; Ding, Y.; Soule, L.; Avdeev, M.; Luo, Z.; Zhang, W.; Yuan, T.; Jing, P.; Gyu Kim, M.; Song, Y.; Liu, M. A Niobium Oxide with a Shear Structure and Planar Defects for High-Power Lithium Ion Batteries. *Energy Environ. Sci.* **2022**, *15* (1), 254–264. https://doi.org/10.1039/D1EE02664J.

(29) Griffith, K. J.; Forse, A. C.; Griffin, J. M.; Grey, C. P. High-Rate Intercalation without Nanostructuring in Metastable Nb_2O_5 Bronze Phases. *J. Am. Chem. Soc.* **2016**, *138* (28), 8888–8899. https://doi.org/10.1021/jacs.6b04345.

(30) Koçer, C. P.; Griffith, K. J.; Grey, C. P.; Morris, A. J. First-Principles Study of Localized and Delocalized Electronic States in Crystallographic Shear Phases of Niobium Oxide. *Phys. Rev. B* **2019**, *99* (7), 1–11. https://doi.org/10.1103/PhysRevB.99.075151.

(31) Wyckoff, K. E.; Robertson, D. D.; Preefer, M. B.; Teicher, S. M. L.; Bienz, J.; Kautzsch, L.; Mates, T. E.; Cooley, J. A.; Tolbert, S. H.; Seshadri, R. High-Capacity Li^+ Storage through Multielectron Redox in the Fast-Charging Wadsley–Roth Phase $(W_{0.2}V_{0.8})_3O_7$. *Chem. Mater.* **2020**, *32* (21), 9415–9424. https://doi.org/10.1021/acs.chemmater.0c03496.

(32) Cheng, Q.; Chen, J.; Zhao, J.; Li, F. A V-Doped $W_3Nb_{14}O_{44}$ Anode in a Wadsley–Roth Structure for Ultra-Fast Lithium-Ion Half/Full Batteries. *New J. Chem.* **2023**, *47* (42), 19537–19545. https://doi.org/10.1039/D3NJ03462C.

(33) Voskanyan, A. A.; Abramchuk, M.; Navrotsky, A. Entropy Stabilization of TiO-NbO Wadsley-Roth Shear Phases and Their Prospects for Lithium Ion Battery Anode Materials Entropy Stabilization of TiO_2-Nb_2O_5 Wadsley–Roth Shear Phases and Their Wadsley–Roth

Phases Accommodate Variable Cation Charg. **2020**. https://doi.org/10.1021/acs.chemmater.0c01553.

(34) Saritha, D.; Pralong, V.; Varadaraju, U. V.; Raveau, B. Electrochemical Li Insertion Studies on $WNb_{12}O_{33}$—A Shear ReO_3 Type Structure. *J. Solid State Chem.* **2010**, *183* (5), 988–993. https://doi.org/10.1016/j.jssc.2010.03.003.

(35) Koçer, C. P.; Griffith, K. J.; Grey, C. P.; Morris, A. J. Lithium Diffusion in Niobium Tungsten Oxide Shear Structures. *Chem. Mater.* **2020**. https://doi.org/10.1021/acs.chemmater.0c00483.

(36) Griffith, K. J.; Grey, C. P. Superionic Lithium Intercalation through 2×2 nm^2 Columns in the Crystallographic Shear Phase $Nb_{18}W_8O_{69}$. *Chem. Mater.* **2020**, *32* (9), 3860–3868. https://doi.org/10.1021/acs.chemmater.9b05403.

(37) Saber, M.; Preefer, M. B.; Kolli, S. K.; Zhang, W.; Laurita, G.; Dunn, B.; Seshadri, R.; Van der Ven, A. Role of Electronic Structure in Li Ordering and Chemical Strain in the Fast Charging Wadsley–Roth Phase PNb_9O_{25}. *Chem. Mater.* **2021**, *33* (19), 7755–7766. https://doi.org/10.1021/acs.chemmater.1c02059.

(38) Koçer, C. P.; Griffith, K. J.; Grey, C. P.; Morris, A. J. Cation Disorder and Lithium Insertion Mechanism of Wadsley–Roth Crystallographic Shear Phases from First Principles. *J. Am. Chem. Soc.* **2019**, *141* (38), 15121–15134. https://doi.org/10.1021/jacs.9b06316.

(39) Saber, M.; Behara, S. S.; Van der Ven, A. Redox Mechanisms, Structural Changes, and Electrochemistry of the Wadsley–Roth $Li_xTiNb_2O_7$ Electrode Material. *Chem. Mater.* **2023**, *35* (22), 9657–9668. https://doi.org/10.1021/acs.chemmater.3c02003.

(40) Trasatti, S.; Buzzanca, G. Ruthenium Dioxide: A New Interesting Electrode Material. Solid State Structure and Electrochemical Behaviour. *J. Electroanal. Chem. Interfacial Electrochem.* **1971**, *29* (2), A1–A5. https://doi.org/10.1016/S0022-0728(71)80111-0.

(41) Boyd, S.; Ganeshan, K.; Tsai, W.-Y.; Wu, T.; Saeed, S.; Jiang, D.; Balke, N.; van Duin, A. C. T.; Augustyn, V. Effects of Interlayer Confinement and Hydration on Capacitive Charge Storage in Birnessite. *Nat. Mater.* **2021**, *20* (12), 1689–1694. https://doi.org/10.1038/s41563-021-01066-4.

(42) Augustyn, V.; Come, J.; Lowe, M. A.; Kim, J. W.; Taberna, P.-L.; Tolbert, S. H.; Abruña, H. D.; Simon, P.; Dunn, B. High-Rate Electrochemical Energy Storage through Li^+ Intercalation Pseudocapacitance. *Nat. Mater.* **2013**, *12* (6), 518–522. https://doi.org/10.1038/nmat3601.

(43) Li, N.; Zhang, F.; Tang, Y. Hierarchical T-Nb2O5 Nanostructure with Hybrid Mechanisms of Intercalation and Pseudocapacitance for Potassium Storage and High-Performance Potassium Dual-Ion Batteries. *J. Mater. Chem. A* **2018**, *6* (37), 17889–17895. https://doi.org/10.1039/c8ta07987k.

(44) Liu, X.; Liu, G.; Chen, H.; Ma, J.; Zhang, R. Facile Synthesis of Nb_2O_5 Nanobelts Assembled from Nanorods and Their Applications in Lithium Ion Batteries. *J. Phys. Chem. Solids* **2017**, *111*, 8–11. https://doi.org/10.1016/j.jpcs.2017.07.007.

(45) Qin, L.; Liu, Y.; Xu, S.; Wang, S.; Sun, X.; Zhu, S.; Hou, L.; Yuan, C. In-Plane Assembled Single-Crystalline T-Nb_2O_5 Nanorods Derived from Few-Layered Nb_2CT_x MXene Nanosheets for Advanced Li-Ion Capacitors. *Small Methods* **2020**, *4* (12), 1–11. https://doi.org/10.1002/smtd.202000630.

(46) Wong, K.; Dia, S. Nanotechnology in Batteries. *J. Energy Resour. Technol.* **2016**, *139* (1). https://doi.org/10.1115/1.4034860.

(47) Liu, T.-C.; Pell, W. G.; Conway, B. E.; Roberson, S. L. Behavior of Molybdenum Nitrides as Materials for Electrochemical Capacitors: Comparison with Ruthenium Oxide. *J. Electrochem. Soc.* **1998**, *145* (6), 1882. https://doi.org/10.1149/1.1838571.

(48) Wang, J.; Polleux, J.; Lim, J.; Dunn, B. Pseudocapacitive Contributions to Electrochemical Energy Storage in TiO_2 (Anatase) Nanoparticles. *J. Phys. Chem. C* **2007**, *111* (40), 14925–14931. https://doi.org/10.1021/jp074464w.

(49) Brezesinski, T.; Wang, J.; Polleux, J.; Dunn, B.; Tolbert, S. H. Templated Nanocrystal-Based Porous TiO_2 Films for Next-Generation Electrochemical Capacitors. *J. Am. Chem. Soc.* **2009**, *131* (5), 1802–1809. https://doi.org/10.1021/ja8057309.

(50) Evanko, B.; Boettcher, S. W.; Yoo, S. J.; Stucky, G. D. Redox-Enhanced Electrochemical Capacitors: Status, Opportunity, and Best Practices for Performance Evaluation. *ACS Energy Lett.* **2017**, *2* (11), 2581–2590. https://doi.org/10.1021/acsenergylett.7b00828.

(51) Levi, M. D.; Salitra, G.; Markovsky, B.; Teller, H.; Aurbach, D.; Heider, U.; Heider, L. Solid-State Electrochemical Kinetics of Li-Ion Intercalation into $Li_{1-x}CoO_2$: Simultaneous Application of Electroanalytical Techniques SSCV, PITT, and EIS. *J. Electrochem. Soc.* **1999**, *146* (4), 1279–1289. https://doi.org/10.1149/1.1391759.

(52) Gan, Z.; Yin, J.; Xu, X.; Cheng, Y.; Yu, T. Nanostructure and Advanced Energy Storage: Elaborate Material Designs Lead to High-Rate Pseudocapacitive Ion Storage. *ACS Nano* **2022**, *16* (4), 5131–5152. https://doi.org/10.1021/acsnano.2c00557.

(53) Cheng, R.; Hu, T.; Zhang, H.; Wang, C.; Hu, M.; Yang, J.; Cui, C.; Guang, T.; Li, C.; Shi, C.; Hou, P.; Wang, X. Understanding the Lithium Storage Mechanism of Ti_3C_2Tx MXene. *J. Phys. Chem. C* **2019**, *123* (2), 1099–1109. https://doi.org/10.1021/acs.jpcc.8b10790.

(54) Preefer, M. B.; Saber, M.; Wei, Q.; Bashian, N. H.; Bocarsly, J. D.; Zhang, W.; Lee, G.; Milam-guerrero, J.; Howard, E. S.; Vincent, R. C.; Melot, B. C.; Ven, A. V. D.; Seshadri, R.; Dunn, B. S. Multielectron Redox and Insulator-to-Metal Transition upon Lithium Insertion in the

Fast-Charging, Wadsley-Roth Phase PNb_9O_{25}. **2020**. https://doi.org/10.1021/acs.chemmater.0c00560.

(55) Costentin, C.; Porter, T. R.; Savéant, J.-M. Nature of Electronic Conduction in “Pseudocapacitive” Films: Transition from the Insulator State to Band-Conduction. *ACS Appl. Mater. Interfaces* **2019**, *11* (32), 28769–28773. https://doi.org/10.1021/acsami.9b05240.

(56) Costentin, C. Electrochemical Energy Storage: Questioning the Popular $v/v^{1/2}$ Scan Rate Diagnosis in Cyclic Voltammetry. *J. Phys. Chem. Lett.* **2020**, *11* (22), 9846–9849. https://doi.org/10.1021/acs.jpclett.0c02667.

(57) Costentin, C.; Porter, T. R.; Savéant, J.-M. How Do Pseudocapacitors Store Energy? Theoretical Analysis and Experimental Illustration. *ACS Appl. Mater. Interfaces* **2017**, *9* (10), 8649–8658. https://doi.org/10.1021/acsami.6b14100.

(58) Ok, K. M.; Halasyamani, P. S.; Casanova, D.; Llunell, M.; Alemany, P.; Alvarez, S. Distortions in Octahedrally Coordinated d^0 Transition Metal Oxides: A Continuous Symmetry Measures Approach. *Chem. Mater.* **2006**, *18* (14), 3176–3183. https://doi.org/10.1021/cm0604817.

CHAPTER II: STRUCTURE-PROPERTY RELATIONSHIPS IN HIGH-RATE ANODE MATERIALS BASED ON NIOBIUM TUNGSTEN OXIDE SHEAR STRUCTURES[2]

2.1 Overview

$Nb_{16}W_5O_{55}$ emerged as a high-rate anode material for Li-ion batteries in 2018 (Griffith et al., *Nature* **2018**, *559* (7715), 556–563). This exciting discovery ignited research in Wadsley-Roth (W-R) compounds, but systematic experimental studies have not focused on how to tune material chemistry and structure to achieve desirable properties for energy storage applications. In this work, we systematically investigate how structure and composition influences capacity, Li-ion diffusivity, charge-discharge profiles, and capacity loss in a series of niobium tungsten oxide W-R compounds: (3×4)-$Nb_{12}WO_{33}$, (4×4)-$Nb_{14}W_3O_{44}$, and (4×5)-$Nb_{16}W_5O_{55}$. Potentiostatic intermittent titration (PITT) data confirmed that Li-ion diffusivity increases with block size, which can be attributed to an increasing number of tunnels for Li-ion diffusion. The small (3×4)-$Nb_{12}WO_{33}$ block size compound with preferential W ordering on tetrahedral sites exhibits single electron redox and, therefore, the smallest measured capacity despite having the largest theoretical capacity. This observation signals that introducing cation disorder (W occupancy at the octahedral sites in the block center) is a viable strategy to access multi-electron redox behavior in (3×4) $Nb_{12}WO_{33}$. The asymmetric block size compounds (i.e., (3×4) and (4×5) blocks) exhibit the greatest capacity loss after the first cycle, possibly due to Li-ion trapping at a unique low energy

---

[2] This work was published in the American Chemical Society, Applied Energy Materials (Luke D. Salzer; Brian Diamond.; Kelly Nieto; R. Colby Evans; Amy Prieto.; Justin Sambur. *ACS Appl. Energy Mater.* **2023**, 6 (3), 1685–1691). Luke D. Salzer performed experiments, analyzed data, and wrote the manuscript. Brian Diamond performed experiments and analyzed data. Kelly Nieto and assisted with coin cell measurements and discussions. R. Colby Evans assisted with materials synthesis and characterization. Justin Sambur assisted in data analysis and manuscript preparation.

pocket site along the shear plane. Finally, the slope of the charge-discharge profile increases with increasing block size, likely because the total number of energy-equivalent Li-ion binding sites also increases. This unfavorable characteristic prohibits the large block sizes from delivering constant power at a fixed C-rate more so than the smaller block sizes. Based on these findings, we discuss design principles for Li-ion insertion hosts made from W-R materials.

2.2 Introduction

One limitation of graphite anodes in Li-ion batteries is Li metal grows from the electrode surface when the cell is cycled at high rates, resulting in catastrophic failure when metallic dendrites pierce the separator and contact the cathode.[2–5] Transition metal oxides are being explored as safe alternatives to graphite because lithium dendrite formation does not occur under fast charge/discharge conditions.[6,7] Of the potential candidates (e.g., TiO_2, Nb_2O_5, and $Li_4Ti_5O_{12}$ (LTO)), Wadsley-Roth (W-R) crystallographic shear structures are attractive anode materials because they exhibit multi-electron redox (beyond 1.0 Li^+/transition metal) and extraordinarily fast Li-ion diffusion coefficients (D_{Li+}) that are two orders of magnitude greater than commercialized LTO.[1,8] Griffith et al. showed that the power density of an un-optimized W-R compound, $Nb_{16}W_5O_{55}$, exceeded that of optimized graphite.[1] This discovery inspired substantial research effort to understand how the unique structural features of niobium tungsten oxide (NbWO) W-R materials contributes to their high-rate capability in a Li-ion battery.

W-R shear structures consist of $n \times m$ blocks of corner-sharing octahedra connected to neighboring blocks via edge-sharing octahedra (see Scheme 2.1).[9–12] The blocks extend indefinitely in the direction perpendicular to the $n \times m$ block plane. In some structures, tetrahedral sites are present at the block corners to fill voids. These W-R phases exhibit many low energy Li-ion binding sites within the large tunnels of the block structure (Scheme 2.1).[13,14] The large number of energy equivalent sites results in low, 0.2-0.3 eV, activation barriers for Li-ion diffusion and room temperature $D_{\mathrm{Li+}}$ values on the order of 1×10^{-12} to 1×10^{-11} $\mathrm{m^2/s}$, highly competitive with state-of-the-art solid state electrolytes.[13,15]

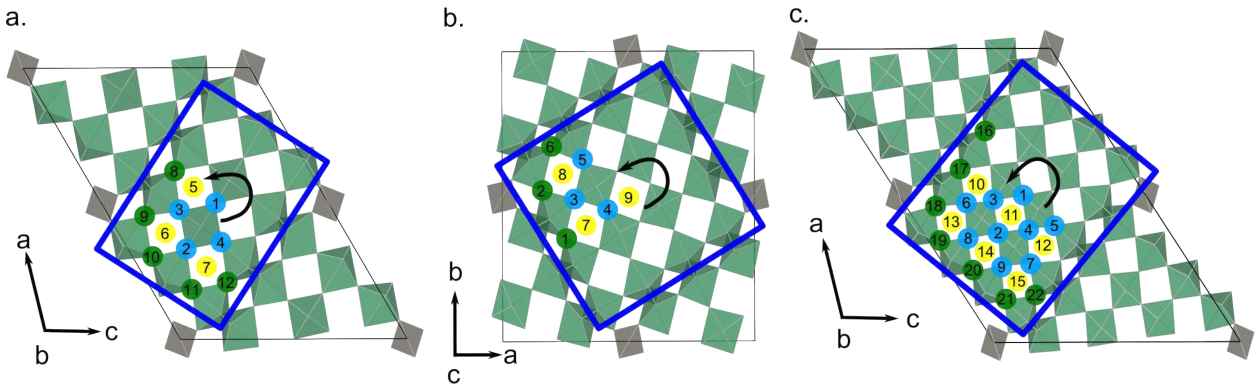

Scheme 2.1. Crystal structures of a) (3×4)-$Nb_{12}WO_{33}$, b) (4×4)-$Nb_{14}W_3O_{44}$, and c) (4×5)-$Nb_{16}W_5O_{55}$. The grey and green polyhedra represent the tetrahedral and octahedral coordination environments, respectively. The blue lines indicate the shear planes and define the block size. The green, yellow, and blue numbered circles represent the pocket, horizontal window, and vertical window Li-ion binding sites according to Koçer et al.[14] (Arrows indicate 2-fold rotation in a) (3×4)-$Nb_{12}WO_{33}$ and c) (4×5)-$Nb_{16}W_5O_{55}$ and a 4-fold rotation in b) (4×4)-$Nb_{14}W_3O_{44}$)

In principle, vast parameter space exists to optimize functional properties via their chemistry, stoichiometry, block size, and characteristic block joining,[12] but few systematic studies focusing on structure-property relationships exist for this exciting class of high-rate energy storage materials. For example, the literature hypothesis states that Li-ion diffusivity increases with increasing W-R block size due to the number of energy equivalent tunnels for long range lithium diffusion.[14] Evaluating this hypothesis is significant because it would establish a key structure/property relationship for researchers developing fast-charging W-R materials. Furthermore, theoretical capacity decreases with increasing block size (Figure A1), but this trend has not been experimentally validated. Confirming this theoretical capacity trend could aid materials discovery efforts by pin-pointing a block size from which to tune chemistry and stoichiometry.

Several research groups have investigated NbWO W-R compounds (e.g., $Nb_{12}WO_{33}$,[12,16,17] $Nb_{26}W_4O_{77}$,[18,19] $Nb_{14}W_3O_{44}$,[12,19,20] $Nb_{16}W_5O_{55}$,[1] and $Nb_{18}W_8O_{69}$[15]), but the performance metrics obtained from those studies reflect a mixture of bulk and nanoscale/structured materials in different electrode formulations and configurations. Capacity loss has been reported in $Nb_{12}WO_{33}$, $Nb_{14}W_3O_{44}$, and $Nb_{16}W_5O_{55}$,[1,20,21] but systematic studies have not focused on the possible Li-ion trapping sites in the different block compounds. In summary, no systematic studies exist that compare functional properties (e.g., capacity, charge/discharge profiles, ionic diffusivity, and capacity loss) versus block size for a nominally equivalent particle morphology and electrochemical cell design.

In this work, we systematically investigated the capacity, capacity loss, charge-discharge curves, and D_{Li+} as a function of block size in the Nb_2O_5-WO_3 system using (3×4)-$Nb_{12}WO_{33}$, (4×4)-$Nb_{14}W_3O_{44}$, and (4×5)-$Nb_{16}W_5O_{55}$. We focused on these compounds because they share the same block connectivity (i.e., joined by tetragonal site at the block corners, Scheme 2.1). Keeping this structural motif consistent is important because the blocks connected by tetragonal sites have different Li-ion binding sites than those that do not.[12] We confirmed the literature hypothesis that D_{Li+} increases with block size. However, the charge/discharge profile becomes steeper and steeper with increasing block size, which hinders those compounds from delivering constant power. We discuss trends in capacity and capacity loss that can be attributed to structural features among the Nb_2O_5-WO_3 series.

2.3 Results and Discussion

W-R compounds were synthesized via high temperature solid state reactions.[1,9,12] Different compositions were accessed by adjusting the mole ratio and heating rate (see Methods for details).[9,12,15] In a typical reaction, stoichiometric ratios of NbO_2 and $WO_{2.9}$ precursors were ground by hand using a mortar and pestle, pressed into a pellet, loaded into a platinum crucible, and heated to 1,200 ºC in air. The powder products were ground in a mortar and pestle for powder X-ray diffraction (XRD) and scanning electron microscopy (SEM) analyses. Figure 2.1 shows XRD data and SEM images of the reaction products that targeted (3×4)-$Nb_{12}WO_{33}$ (space group *C2*), (4×4)-$Nb_{14}W_3O_{44}$ (space group *I4/m*), and (4×5)-$Nb_{16}W_5O_{55}$ (space group C2). Rietveld refinement indicated each sample's phase purity exceeded 90%, consistent with Griffith et al,[22] as well as the following trends that have important consequences for multi-electron redox behavior discussed below: (1) preference for W^{6+} at the tetrahedral site for $Nb_{12}WO_{33}$, (2) W^{6+} occupancy at the octahedral sites in the block center for (4×4)-$Nb_{14}W_3O_{44}$ and (4×5)-$Nb_{16}W_5O_{55}$, and (3) and significant cation disorder for (4×4)-$Nb_{14}W_3O_{44}$ and (4×5)-$Nb_{16}W_5O_{55}$.[14,15,23]

The reactions produced samples with nearly equivalent particle morphologies (Figure 2.1a-c), specifically micron-size particles with subhedral to euhedral columnar crystal habit, in agreement with literature.[1,15] The major axis dimensions of (3×4)-$Nb_{12}WO_{33}$ and (4×4)-$Nb_{14}W_3O_{44}$ samples were nearly identical (1.1 ± 0.2 µm and 1.2 ± 0.3 µm, respectively, for N = 100 particles and the error represents the standard deviation). The average particle size of the (4×5)-$Nb_{16}W_5O_{55}$ sample was slightly larger (1.7 ± 0.4 µm, N=100). In summary, we synthesized a series of W-R samples with similar particle size and morphology so we could compare how the electrochemical properties and ionic diffusivity trends change with increasing block size.

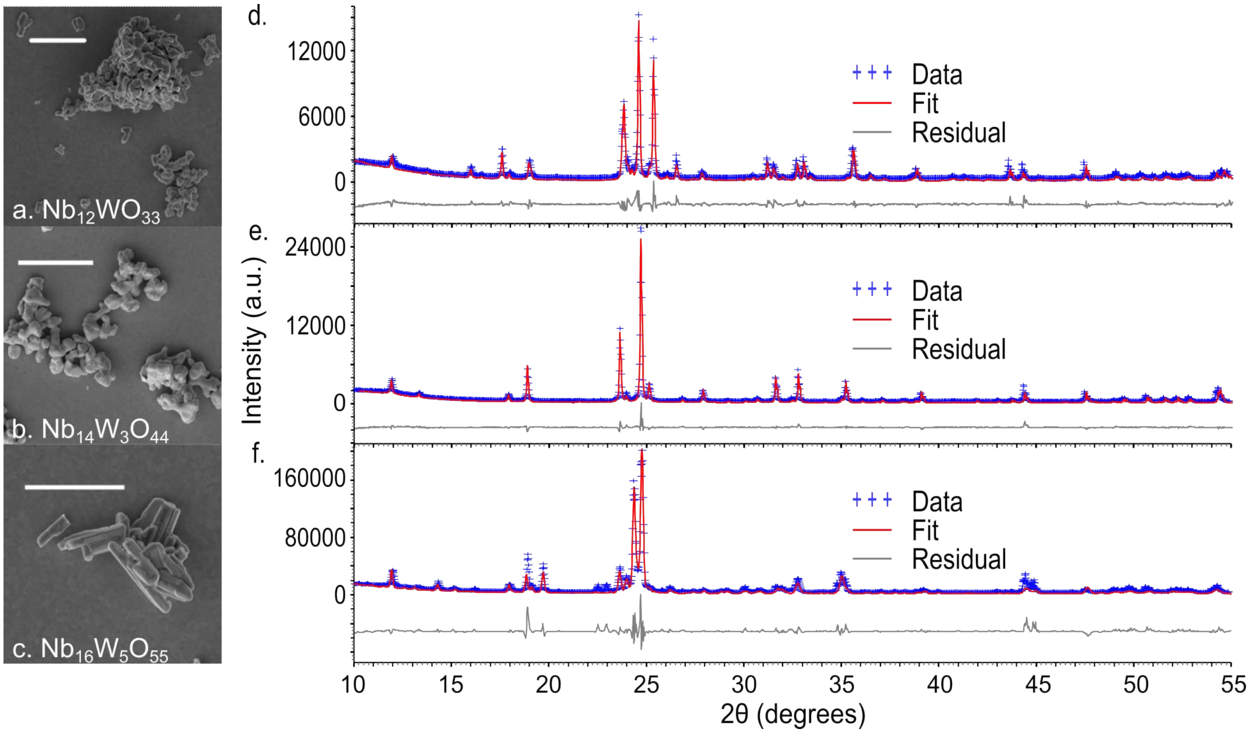

Figure 2.1. Morphology and structural characterization of niobium tungsten oxide W-R compounds. (a-c) SEM images and (e-f) XRD data of (3×4)-$Nb_{12}WO_{33}$, (4×4)-$Nb_{14}W_3O_{44}$, and (4×5)-$Nb_{16}W_5O_{55}$. The solid red lines represent Rietveld refinement results. All scale bars in (a-c) are 10 μm.

Next, we evaluated the electrochemical properties of the W-R compounds as Li-ion insertion hosts under nearly identical conditions. We designed electrodes and chose experimental procedures that maximized the possibility of observing how electrochemical properties change with block size, rather than optimize battery performance. To do so, we constructed coin cells using an 8:1:1 ratio of active material, conductive carbon, and binder because this ratio has been shown to minimize ohmic losses of the intrinsically poorly conducting oxide particles.[24,25] Additionally, we employed slow galvanostatic cycling conditions (<C/3) that further minimize ohmic losses and enhance hidden features in differential capacity plots.

Figure 2.2a-c shows the (dis)charge curves for (3×4)-$Nb_{12}WO_{33}$, (4×4)-$Nb_{14}W_3O_{44}$, and (4×5)-$Nb_{16}W_5O_{55}$, respectively. For all compounds, the discharge curve can be divided into three potential regions (denoted by horizontal lines in Figure 2.2a-c and vertical lines in Figure 2.2d-f).

We discuss the (dis)charge curve of (3×4)-$Nb_{12}WO_{33}$ only because all compounds exhibit the following characteristics. In Region I (Figure 2.2a), the potential rapidly decreases from 3.0 V to 2.0 V vs Li/Li^+ with increasing x in $Li_xNb_{12}WO_{33}$ until an inflection point occurs at $x = 1$. Then, in Region II, the potential gradually drops from 1.90 to 1.75 V with increasing lithiation content until $x = 10$. Finally, in Region III, the potential decreases to 1.0 V. The first discharge capacity is 203 mAh/g, in agreement with literature values for samples synthesized via a high temperature solid state reaction.[16] Upon de-lithiation of (3×4)-$Nb_{12}WO_{33}$, the potential quickly increases from 1.00 to 1.19 V. In Region II, the potential monotonically increases until an inflection point occurs at approximately 1.80 V. Lastly, the potential increases rapidly in Region III from 2.0 to 3.0 V vs Li/Li^+. The first charge capacity is 179 mAh/g, corresponding to 88% coulombic efficiency (CE) after the first cycle (Figure A1.2). The low CE after the first cycle suggests irreversible Li-ion trapping in the host, which has been suggested in the literature and will be discussed below.[13]

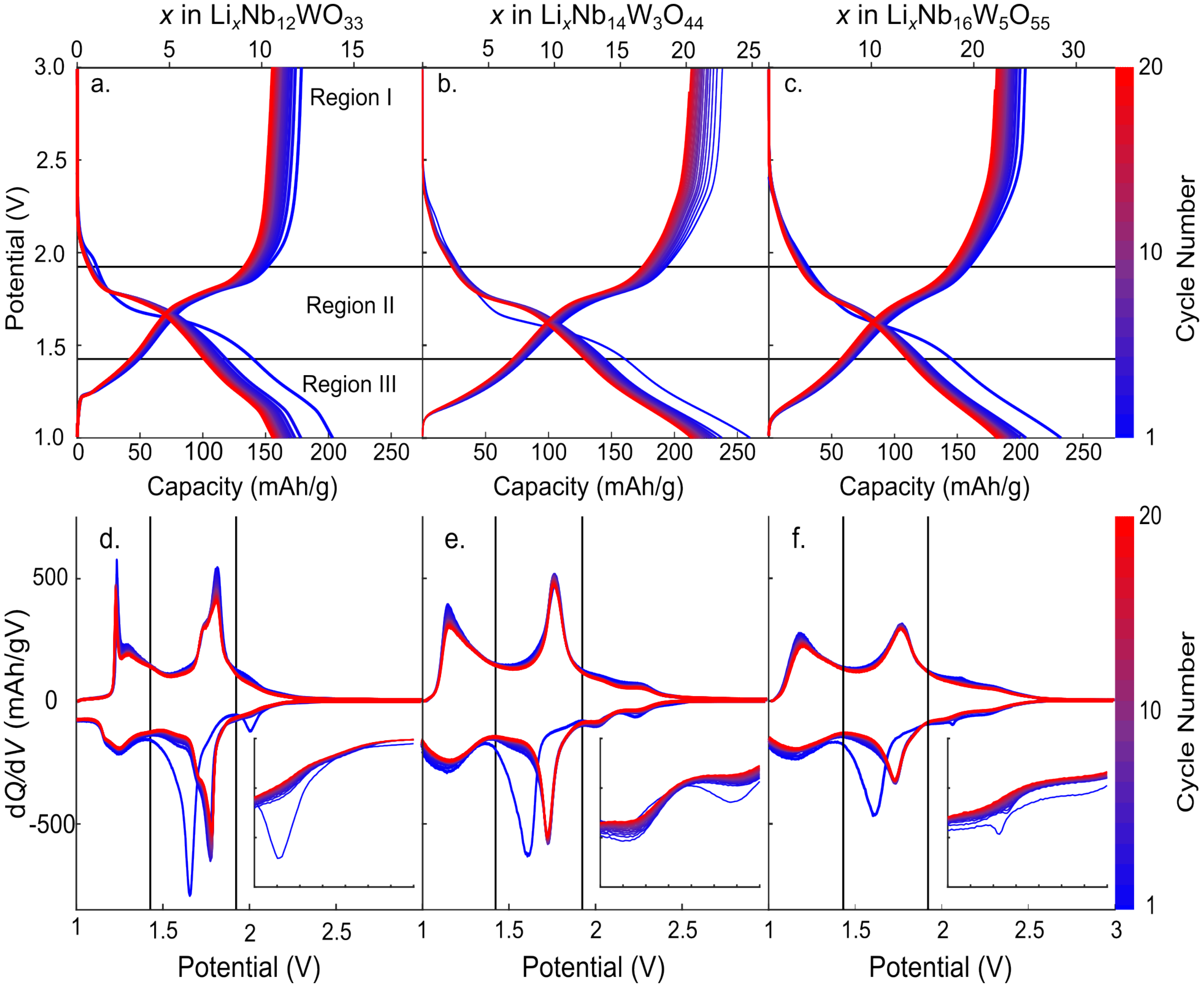

Figure 2.2. Charge/discharge curves (20 cycles at C/3) of a) $Nb_{12}WO_{33}$, b) $Nb_{14}W_3O_{44}$, and c) $Nb_{16}W_5O_{55}$ and differential capacity plots of d) $Nb_{12}WO_{33}$, e) $Nb_{14}W_3O_{44}$, and f) $Nb_{16}W_5O_{55}$. Insets in (d-f) represent the potential range from 1.95 to 2.30 V.

One noticeable trend in the charge-discharge profiles is the increasing sloping profile from left to right in Figure 2.2a-c, which manifests in peak broadening for the Region II peak in the d*Q*/d*V* plots (Figure 2.2d-f). We observe a strong positive correlation between the full width at half maximum (FWHM) of the Region II peak and the total number of Li-ion binding sites in the unit cell (Figure A1.3). Hence, introducing a larger number of energy equivalent Li-ion binding sites likely causes the redox reactions to occur over a broader range of potentials, inducing a steeper voltage profile with increasing block size. The observation indicates a structural limitation of the large block size compounds because flat voltage profiles are highly desirable for delivering constant power in energy storage applications. One strategy to address this sloping voltage profile issue is to tune the redox potentials of the Li-ion binding sites via transition metal doping in the block center or along the shear plane.

Another critical observation from the cycling data Figure 2.1 is the measured capacity does not decrease with block size. We expected to observe a monotonic decrease in capacity with increasing block size (Figure A1.1). However, (4×4)-$Nb_{14}W_3O_{44}$ exhibited the highest specific discharge capacity upon lithiation (260 mAh/g after first discharge), while (3×4)-$Nb_{12}WO_{33}$ and (4×5)-$Nb_{16}W_5O_{55}$ exhibited 203 and 232 mAh/g, respectively (Figure 2.2a-c). To understand the origin of our observations, we examined the ratio of measured capacity to theoretical capacity assuming 1 Li^+/transition metal (Figure A1.4), including literature data for (5×5)-$Nb_{18}W_8O_{69}$ synthesized via a high temperature solid state reaction.[15] Interestingly, (3×4)-$Nb_{12}WO_{33}$ is the only compound that does not exhibit multielectron redox; all other compounds exhibit approximately 1.4 Li^+/transition metal. The structurally unique feature of (3×4)-$Nb_{12}WO_{33}$ is W ordering on the tetrahedral sites, in agreement with literature and observed in our Rietveld analyses.[14] As the block size increases, the probability of W occupancy in the block center increases.[14] Since X-ray absorption spectroscopy measurements of (4×5)-$Nb_{16}W_5O_{55}$ clearly show W is responsible for multielectron redox behavior, we conclude that (3×4)-$Nb_{12}WO_{33}$ exhibits lower capacity than the larger block compounds because tetrahedral W sites do not contribute to multi-electron redox behavior.[1] Indirect evidence for this hypothesis exists in the literature. For example, Saritha et al. compared the capacity of (3×4)-$Nb_{12}WO_{33}$ electrodes synthesized via a high temperature solid state reaction and a low temperature sol-gel route, which reached approximately 19 Li^+/transition metal.[16] The authors observed discharge capacities greater than 1 Li^+/transition metal for the sol gel material, which we believe stems from cation disorder in the material synthesized at low temperature (W occupancy in the block center). Yan et al. also observed multi-electron redox (1.2 Li^+/transition metal) in nanostructured (3×4)-$Nb_{12}WO_{33}$ synthesized via electrospinning followed by sintering at 1000 °C, where significant cation disorder may also be present in the material.[17] In summary, we hypothesize that W occupancy in the block center is responsible for multi-electron redox behavior in the larger block sizes and, therefore, introducing W disorder in (3×4)-$Nb_{12}WO_{33}$ materials is a viable strategy to access >1 Li^+/transition metal.

Next, we analyzed the capacity loss trends as a function of block size (Figure 2.3). The asymmetric block compounds (e.g., $m \neq n$ in (3×4)-$Nb_{12}WO_{33}$ and (4×5)-$Nb_{16}W_5O_{55}$) exhibit greater capacity loss than the symmetric (4×4)-$Nb_{14}W_3O_{44}$ material. Specifically, (3×4)-$Nb_{12}WO_{33}$ and (4×5)-$Nb_{16}W_5O_{55}$) show >12% capacity loss whereas (4×4)-$Nb_{14}W_3O_{44}$ exhibits 8% capacity loss. Distinct features appear in the dQ/dV plots of the "asymmetric" block structure compounds (i.e., (3×4) and (4×5)) that could explain the structural origin of the greater capacity loss. The asymmetric block compounds exhibit a single, sharp irreversible peak in Region I of the initial discharge cycle of the dQ/dV plots (inset Figure 2.1d,f-insets). On the other hand, (4×4)-$Nb_{14}W_3O_{44}$ and (5×5)-$Nb_{18}W_8O_{69}$ exhibit two broad and relatively more reversible peaks in Region I (Figure 2.2e-inset and reference 15). We hypothesize that (3×4)-$Nb_{12}WO_{33}$ and (4×5)-$Nb_{16}W_5O_{55}$ exhibit one peak in Region I because 1 Li^+ inserts into a low energy 5-fold coordinated "pocket" site at the shear plane (site 12 in Scheme 2.1a and site 17 in Scheme 2.1c). Koçer et al.'s first principles calculations suggested that this pocket site is a low energy, highly stable Li-ion binding site that is likely responsible for ion trapping in NWO compounds.[13] An alternative possibility is that the first Li-ion inserts in the symmetry unique site in the block center of the asymmetric compounds (site 1 in Scheme 2.1a,c). These results provide insight into how unit cell symmetry may affect capacity retention and highlight the need for future work to elucidate the lithiation mechanism and site ordering in W-R phases.

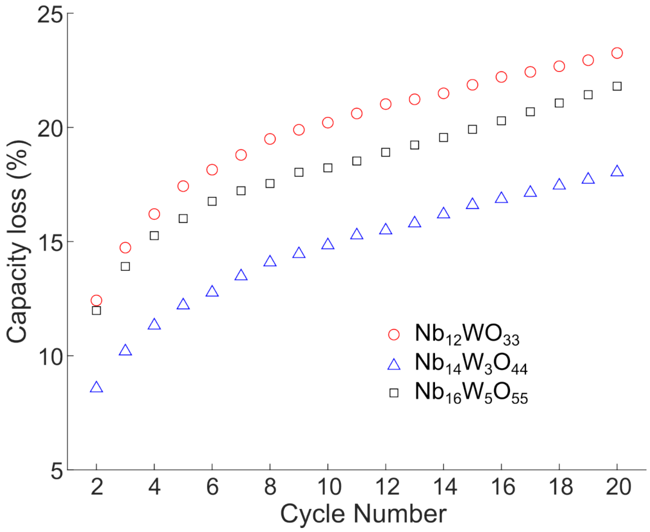

Figure 2.3. Capacity loss, defined as the discharge capacity for each cycle divided by the first discharge capacity, for (3×4)-$Nb_{12}WO_{33}$, (4×4)-$Nb_{14}W_3O_{44}$, and (4×5)-$Nb_{16}W_5O_{55}$.

Finally, we tested the literature hypothesis that Li-ion diffusivity increases with increasing block size.[15] To do so, we performed PITT measurements on cycled coin cells (see Methods) to minimize the influence of cycle-dependent performance that occurs for freshly made coin cells. Adapting the approach of Aurbach et al.,[26] we applied 25 mV potential steps from 1.0 to 2.0 V and fit the current-time data for $t > 30$ min. This condition yields a slope equal to $\frac{D_{Li+}\pi^2}{4L^2}$,[27] where L is the particle length. In this work, we define L as half the major axis dimension as determined by particle size analysis (N = 100 particles) from SEM images. We focus on PITT measurements starting from the unlithiated state because the compounds are more electronically conducting in the lithiated condition, and we suspect the insulating nature of the intrinsic oxides could influence the D_{Li+} values when the potential is swept from 2.0 to 1.0 V. Figure 2.4a shows the resulting D_{Li+} values versus potential for (3×4)-$Nb_{12}WO_{33}$, (4×4)-$Nb_{14}W_3O_{44}$, and (4×5)-$Nb_{16}W_5O_{55}$. D_{Li+} values show a peak-like feature between 1.2-1.3 V, in agreement with literature, and then remain approximately potential independent over the range of 1.5-2.0 V.[1,13,17] The D_{Li+} peak feature could be due to the unique lattice expansion mechanism with increasing *x*. The average Li-ion diffusion coefficient over the potential range of 1.4-1.6 V increases with increasing block size (Figure 2.4b), confirming the literature hypothesis that increasing the number of energy equivalent tunnels in the block structure increases Li-ion diffusivity. This important structure-property relationship holds whether performing PITT experiments or analyses starting from the lithiated state (Figure A1.5).

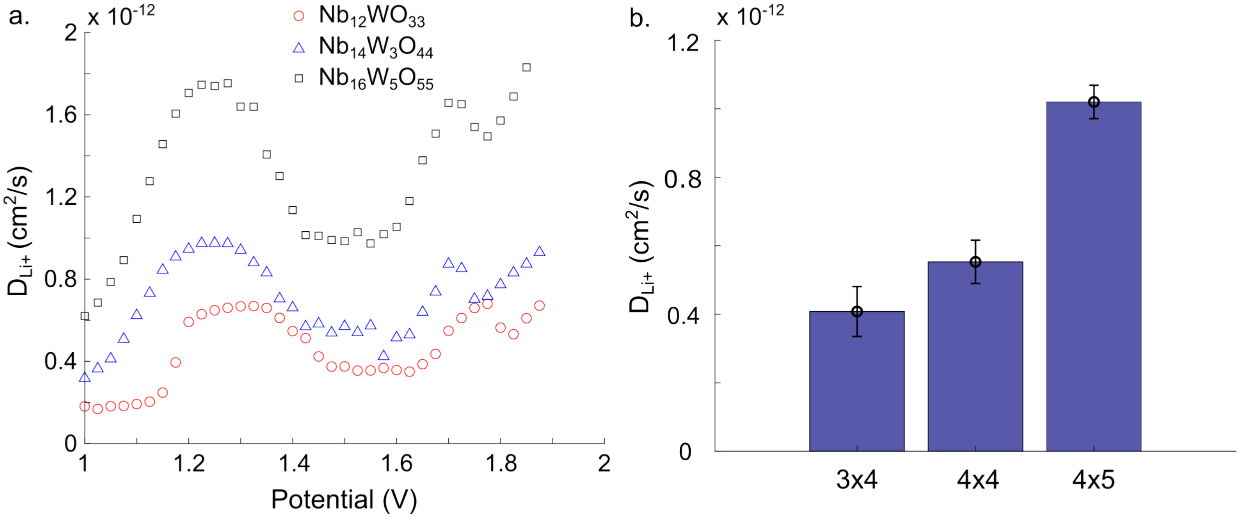

Figure 2.4. (a) Li-ion diffusion coefficient versus applied potential, as determined via PITT measurements for the cathodic sweep from 1.0 to 2.0 V. (b) Average D_{Li+} values for the potential range of 1.4-1.6 V (error bars indicate standard deviation).

2.3 Conclusion

We synthesized a series of NbWO W-R compounds to investigate how block size influences electrochemical properties and performance metrics of interest for high-rate electrochemical energy storage applications. The D_{Li+} values increase with increasing block size, suggesting the larger block size compounds may be superior anode materials for high-rate applications. However, increasing block size does not lead to a monotonic increase in capacity: (4×4)-$Nb_{14}W_3O_{44}$ possesses the largest discharge capacity, followed by (4×5)-$Nb_{16}W_5O_{55}$ and (3×4)-$Nb_{12}WO_{33}$. The low capacity for the (3×4)-$Nb_{12}WO_{33}$ compound stems from its inability to access multi-electron redox behavior, further signaling that octahedral W sites are responsible for multi-electron redox behavior in the larger block sizes. Furthermore, the block symmetry affects capacity retention: the asymmetric (3×4)-$Nb_{12}WO_{33}$ and (4×5)-$Nb_{16}W_5O_{55}$ compounds exhibit greater capacity loss, likely due to a low energy Li-ion trapping site along the shear plane. Lastly, W-R compounds with larger block sizes exhibit steeper and steeper charge/discharge profiles, which limits their ability to deliver constant power in energy storage applications. This sloping voltage profile trend may be due to the larger block sizes possessing more lithium storage sites with a broader range of Li-ion binding energies and environments. The structure-property relationships reported herein should extend to other W-R compounds and, therefore, guide the development of novel W-R compositions for electrochemical energy storage applications.

2.4 Methods

2.4.1 Synthesis and structure characterization

The samples were produced using high tempersature solid-state synthesis following literature protocols.[1,9,12] All three compostions were synthesised from stoichimetric ratios of NbO_2 (Alfa Aesar) and $WO_{2.9}$ (Alfa Aesar); for example, 1.64 g of NbO_2 and 0.25 g of $WO_{2.9}$ were required to synthesize (3×4)-$Nb_{12}WO_{33}$. The solid powders were ground in an agate mortar and pestle and pressed into a pellet using a hydrolic press (Caver Model: 4350.L) at 2 tons of pressure. The pellets were placed in a platinum crucible and heated in air in a Thermo Scientific Lindberg Blue M tube furnace. To access the (3×4)-$Nb_{12}WO_{33}$ and (4×4)-$Nb_{14}W_3O_{44}$ compounds, the pellets were heated from 25°C to 1200°C over a 10 hr period (2 °C/min) and then cooled to 25°C in 10 hours. The (4×5)-$Nb_{16}W_5O_{55}$ compound was prepared by heating the pellet from 25°C to 1,200 ºC at 10 ºC/min and cooling to 25°C. The pellets were ground using a mortar and pestle before materials characterization. The samples were characterized by powder XRD using a Bruker D8

Discover DaVinci – Powder Diffractometer (Cu Kα radiation). Scanning electron microscopy analyses were performed on a JEOL 6500 field emission SEM.

2.4.2 Battery assembly and electrochemical measurements

Half-cell batteries were constructed in an argon glove box using stainless steel coin cells (MTI, CR2032 cases, with a polypropylene sealing gasket), a stainless-steel conical spring, a stainless-steel spacer, a polypropylene (MTI Corp) and glass microfiber (Whatman) separator. These electrodes had an active material:carbon:binder mass ratio of 8:1:1. The metal oxide, conductive carbon (Super P), and polyvinylidene fluoride binder were hand ground in an agate mortar and pestle. The mixture was dispersed in N-methyl pyrrolidone (NMP, Sigma-Aldrich) before doctor-blading a 100 μm-thick film on a copper substrate and dried in a vacuum oven overnight at 150°C. The dried half cells were punched into ½ inch electrodes. These electrodes served as the cathode and lithium metal served as the anode. The electrolyte containing 1M $LiPF_6$ dissolved in a 1:1 volume ratio of ethylene carbonate/dimethyl carbonate (EC/DMC, Sigma Aldrich) was dropped (approximately 80μl) onto the separators. The cells were then pressed with 0.9 tons of pressure using a compact digital pressure controlled electric crimper (MTI MSK-160E).

The coin cells were cycled on an Arbin battery tester (LBT-20084) using the following procedure. The cells rested for 12 h prior to cycling so that the added electrolyte had adequate time to saturate the separators. Following the resting period, the cells were cycled at low C-rates (<C/3), which was calculated for each compound using its theoretical capacity for one-electron transfer per transition metal. The potential window for galvanostatic cycling was 1.0 V to 3.0 V vs Li^+/Li. PITT measurements were conducted using a CHI potentiostat (Model 1200 series) over the potential range of 1.0 to 2.0 V vs. Li/Li^+ in potential steps of 25mV. The current for each potential step was measured for 45 minutes. We fit the *i-t* response for $t > 30$ min, according to literature.[26,27]

A 15-minute wait time was applied after each potential step to allow the cell to reach steady state conditions.

2.5 References

(1) Griffith, K. J.; Wiaderek, K. M.; Cibin, G.; Marbella, L. E.; Grey, C. P. Niobium Tungsten Oxides for High-Rate Lithium-Ion Energy Storage. *Nature* **2018**, *559* (7715), 556–563. https://doi.org/10.1038/s41586-018-0347-0.

(2) Burns, J. C.; Stevens, D. A.; Dahn, J. R. In-Situ Detection of Lithium Plating Using High Precision Coulometry. *J. Electrochem. Soc.* **2015**, *162* (6), A959. https://doi.org/10.1149/2.0621506jes.

(3) Downie, L. E.; Krause, L. J.; Burns, J. C.; Jensen, L. D.; Chevrier, V. L.; Dahn, J. R. In Situ Detection of Lithium Plating on Graphite Electrodes by Electrochemical Calorimetry. *J. Electrochem. Soc.* **2013**, *160* (4), A588. https://doi.org/10.1149/2.049304jes.

(4) Vetter, J.; Novák, P.; Wagner, M. R.; Veit, C.; Möller, K.-C.; Besenhard, J. O.; Winter, M.; Wohlfahrt-Mehrens, M.; Vogler, C.; Hammouche, A. Ageing Mechanisms in Lithium-Ion Batteries. *J. Power Sources* **2005**, *147* (1), 269–281. https://doi.org/10.1016/j.jpowsour.2005.01.006.

(5) Ribière, P.; Grugeon, S.; Morcrette, M.; Boyanov, S.; Laruelle, S.; Marlair, G. Investigation on the Fire-Induced Hazards of Li-Ion Battery Cells by Fire Calorimetry. *Energy Environ. Sci.* **2012**, *5* (1), 5271–5280. https://doi.org/10.1039/C1EE02218K.

(6) Deng, Q.; Fu, Y.; Zhu, C.; Yu, Y. Niobium-Based Oxides Toward Advanced Electrochemical Energy Storage: Recent Advances and Challenges. *Small* **2019**, No. 0, 1804884. https://doi.org/10.1002/smll.201804884.

(7) Ding, H.; Song, Z.; Zhang, H.; Zhang, H.; Li, X. Niobium-Based Oxide Anodes toward Fast and Safe Energy Storage: A Review. *Mater. Today Nano* **2020**, *11*, 100082. https://doi.org/10.1016/j.mtnano.2020.100082.

(8) Griffith, K. J.; Harada, Y.; Egusa, S.; Ribas, R. M.; Monteiro, R. S.; Von Dreele, R. B.; Cheetham, A. K.; Cava, R. J.; Grey, C. P.; Goodenough, J. B. Titanium Niobium Oxide: From Discovery to Application in Fast-Charging Lithium-Ion Batteries. *Chem. Mater.* **2020**, acs.chemmater.0c02955. https://doi.org/10.1021/acs.chemmater.0c02955.

(9) Roth, R. S.; Wadsley, A. D. Multiple Phase Formation in the Binary System Nb_2O_5–WO_3. I. Preparation and Identification of Phases. *Acta Crystallogr.* **1965**, *19* (1), 26–32. https://doi.org/10.1107/S0365110X65002712.

(10) Roth, R. S.; Wadsley, A. D. Multiple Phase Formation in the Binary System Nb_2O_5–WO_3. II. The Structure of the Monoclinic Phases $WNb_{12}O_{33}$ and $W_5Nb_{16}O_{55}$. *Acta Crystallogr.* **1965**, *19* (1), 32–38. https://doi.org/10.1107/S0365110X65002724.

(11) Andersson, S.; Wadsley, A. D. Crystallographic Shear and Diffusion Paths in Certain Higher Oxides of Niobium, Tungsten, Molybdenum and Titanium. *Nature* **1966**, *211* (5049), 581–583. https://doi.org/10.1038/211581a0.

(12) Cava, R. J.; Murphy, D. W.; Zahurak, S. M. Lithium Insertion in Wadsley-Roth Phases Based on Niobium Oxide. *J. Electrochem. Soc.* **1983**, *130* (12), 2345. https://doi.org/10.1149/1.2119583.

(13) Koçer, C. P.; Griffith, K. J.; Grey, C. P.; Morris, A. J. Lithium Diffusion in Niobium Tungsten Oxide Shear Structures. *Chem. Mater.* **2020**, *32* (9), 3980-3989. https://doi.org/10.1021/acs.chemmater.0c00483.

(14) Koçer, C. P.; Griffith, K. J.; Grey, C. P.; Morris, A. J. Cation Disorder and Lithium Insertion Mechanism of Wadsley–Roth Crystallographic Shear Phases from First Principles. *J. Am. Chem. Soc.* **2019**, *141* (38), 15121–15134. https://doi.org/10.1021/jacs.9b06316.

(15) Griffith, K. J.; Grey, C. P. Superionic Lithium Intercalation through 2×2 nm^2 Columns in the Crystallographic Shear Phase $Nb_{18}W_8O_{69}$. *Chem. Mater.* **2020**, *32* (9), 3860-3868. https://doi.org/10.1021/acs.chemmater.9b05403.

(16) Saritha, D.; Pralong, V.; Varadaraju, U. V.; Raveau, B. Electrochemical Li Insertion Studies on $WNb_{12}O_{33}$—A Shear ReO_3 Type Structure. *J. Solid State Chem.* **2010**, *183* (5), 988–993. https://doi.org/10.1016/j.jssc.2010.03.003.

(17) Yan, L.; Lan, H.; Yu, H.; Qian, S.; Cheng, X.; Long, N.; Zhang, R.; Shui, M.; Shu, J. Electrospun $WNb_{12}O_{33}$ Nanowires: Superior Lithium Storage Capability and Their Working Mechanism. *J. Mater. Chem. A* **2017**, *5* (19), 8972–8980. https://doi.org/10.1039/C7TA01784G.

(18) Fuentes, A. F.; de la Cruz, A. M.; Torres-Martínez, L. M. A Study of Lithium Insertion in $W_4Nb_{26}O_{77}$: Synthesis and Characterization of New Phases. *Solid State Ion.* **1996**, *92* (1), 103–111. https://doi.org/10.1016/S0167-2738(96)00374-8.

(19) Fuentes, A. F.; Cruz, A. M. D. L.; Torres-Martinez, L. M. A Comparative Study of Lithium and Sodium Insertion in Two Block Structure Type Phases, $W_3Nb_{14}O_{44}$ and $W_4Nb_{26}O_{77}$. *MRS Online Proc. Libr. Arch.* **1996**, *453*. https://doi.org/10.1557/PROC-453-659.

(20) Fuentes, A. F.; Garza, E. B.; de la Cruz, A. M.; Torres-Martínez, L. M. Lithium and Sodium Insertion in $W_3Nb_{14}O_{44}$, a Block Structure Type Phase. *Solid State Ion.* **1997**, *93* (3), 245–253. https://doi.org/10.1016/S0167-2738(96)00537-1.

(21) Yang, Y.; Zhu, H.; Xiao, J.; Geng, H.; Zhang, Y.; Zhao, J.; Li, G.; Wang, X.-L.; Li, C. C.; Liu, Q. Achieving Ultrahigh-Rate and High-Safety Li+ Storage Based on Interconnected Tunnel Structure in Micro-Size Niobium Tungsten Oxides. *Adv. Mater.* **2020**, *32* (12), 1905295. https://doi.org/10.1002/adma.201905295.

(22) Griffith, K. J.; Forse, A. C.; Griffin, J. M.; Grey, C. P. High-Rate Intercalation without Nanostructuring in Metastable Nb_2O_5 Bronze Phases. *J. Am. Chem. Soc.* **2016**, *138* (28), 8888–8899. https://doi.org/10.1021/jacs.6b04345.

(23) Cheetham, A. K.; Allen, N.C. Cation Distribution in the Complex Oxide, $W_3Nb_{14}O_{44}$; a Time-of-Flight Neutron Diffraction Study. *J Chem Soc Commun* **1983**, 3, 1370-1372.

(24) Jiang, J.; Li, Y.; Liu, J.; Huang, X.; Yuan, C.; Lou, X. W. (David). Recent Advances in Metal Oxide-Based Electrode Architecture Design for Electrochemical Energy Storage. *Adv. Mater.* **2012**, *24* (38), 5166–5180. https://doi.org/10.1002/adma.201202146.

(25) Itou, Y.; Ogihara, N.; Kawauchi, S. Role of Conductive Carbon in Porous Li-Ion Battery Electrodes Revealed by Electrochemical Impedance Spectroscopy Using a Symmetric Cell. *J. Phys. Chem. C* **2020**, *124* (10), 5559–5564. https://doi.org/10.1021/acs.jpcc.9b11929.

(26) Aurbach, D.; Levi, M. D.; Levi, E. A Review on the Solid-State Ionics of Electrochemical Intercalation Processes: How to Interpret Properly Their Electrochemical Response. *Solid State Ion.* **2008**, *179* (21–26), 742–751. https://doi.org/10.1016/j.ssi.2007.12.070.

(27) Wen, C. J.; Boukamp, B. A.; Huggins, R. A.; Weppner, W. Thermodynamic and Mass Transport Properties of “LiAl” *J. Electrochem. Soc.* **1979**, *126* (12), 2258–2266. https://doi.org/10.1149/1.2128939.

CHAPTER III: STRUCTURAL DISORDER AND MOLYBDENUM SUBSTITUTION ENABLE MULTI-ELECTRON REDOX IN THE CRYSTALLOGRAPHIC SHEAR COMPOUND $Mo_xNb_{12}W_{1-x}O_{33}$[3]

3.1 Overview

Transition metal oxide Wadsley-Roth crystallographic shear compounds are promising alternatives to graphite for high-rate Li-ion battery applications, but open questions remain regarding how to tune their structure and composition for desired electrochemical properties such as lower working potential, enhanced capacity, and increased cycle stability. Our work addresses two key questions in a class of niobium oxide-based W-R compounds that outperform graphite in laboratory cells: (1) How does transition metal substitution influence redox mechanisms and the electrochemically active density of states (DOS) that determine the working potential?; (2) How does the degree of second order Jahn-Teller (SOJT) distortion of the transition metal octahedra along the crystallographic shear plane influence the structural stability of the compound under repeated cycling?[1,2] To answer these questions, we systematically investigated a series of nearly phase pure $Mo_xNb_{12}W_{1-x}O_{33}$ and defect-rich D-$Mo_xNb_{12}W_{1-x}O_{33}$ samples, as evidenced by experimental and computational Raman spectroscopy as well as X-ray diffraction and Rietveld refinement analyses. We focused on Mo doping because it exhibits larger SOJT distortion than Nb and W d^0 cations. Galvanostatic cycling revealed that Mo substitution for W alters the electrochemically active DOS and activates multi-electron redox (either Nb^{5+} to Nb^{3+} or Mo^{6+} to

---

[3] Luke D. Salzer performed experiments, analyzed data, and wrote the manuscript. Cami Christensen and Claire Y. Gervais both performed experiments and analyzed data. Dani Lustig assisted with scanning electron microscopy measurements. Gil M. Repa, Zachary J. Knepp, and Prof. Lisa A. Fredin from Lehigh University for the computational Raman work.

Mo^{4+}), likely via a metal-metal bonding redox mechanism involving edge shared Mo-Nb octahedra along the shear plane. The defective samples generally exhibited higher capacities, likely due to the presence of Wadsley defects (e.g., intergrowth of $W_4Nb_{26}O_{77}$ in a matrix of $Nb_{12}WO_{33}$) that further lower Li-ion binding energetics and alter Li-ion transport paths. Mo-rich samples exhibit greater capacity loss with additional cycling, possibly due to the inability of severely distorted Mo octahedra from "rocking" back and forth during lithiation/de-lithiation cycles or particle fracturing incurred at high lithiation levels. These findings are crucial as they inform Wadsley-Roth material design strategies aimed at systematically increasing capacity by optimizing metal-metal bonding energetics along the shear plane and reducing capacity loss through the second order Jahn-Teller effect.

3.2 Introduction

Transition metal oxide Wadsley-Roth (W-R) crystallographic shear compounds are promising anode materials that could replace graphite in high-rate Li-ion battery applications. Wadsley, Roth, Allpress, and Anderson established the structural principles of W-R crystallographic shear structures in the 1960s.[3–10] In 1983, Cava et al. chemically lithiated niobium oxide W-R phases with oxides of titanium, vanadium, tungsten, germanium, and tungsten vanadium oxides.[11] Later, in 2018, Grey and co-workers demonstrated niobium tungsten oxide W-R materials (W-R $Nb_{16}W_5O_{55}$ and a tungsten bronze $Nb_{18}W_{16}O_{93}$) exhibit higher volumetric capacity and superior rate capabilities compared to traditional graphite anodes.[1] A major advantage of niobium oxide-based W-R anode materials is that they operate outside the potential window where lithium dendrites form, positioning them as safe electrodes for high-rate energy storage applications.[12,13] While these W-R phases demonstrate considerable structural and chemical tunability, a significant unresolved question for this class of materials is how to precisely adjust their composition and structure to optimize desired properties such as capacity, operating voltage, and cyclability. Developing robust structure-property relationships is challenging in W-R phases because transition metal cations can occupy various sites within the crystal structure, and even minor changes in site occupancy can greatly impact electrochemical properties. Moreover, defect phases frequently form in these compounds, complicating the attribution of new functional properties to intentional compositional changes or unintended structural modifications.

One interesting feature of W-R compounds is that small compositional changes can greatly alter electrochemical properties. For example, Preefer et al. synthesized isostructural PNb_9O_{25} and VNb_9O_{25} and discovered that these compounds store approximately 11 and 14 electrons and Li-ions per formula unit, respectively, at slow charge rates.[14] However, when the charge/discharge rate increases by an order of magnitude, PNb_9O_{25} still stores approximately 11 electrons per formula unit, while VNb_9O_{25}'s storage capacity decreases to approximately 9 electrons. Other literature examples of this phenomena include Nb-O, W-Nb-O, Ti-Nb-O, P-Nb-O, and V-Nb-O.[1,14–19] This dramatic change in charge stored with one elemental substitution highlights the importance of understanding how structure-property relationships can guide design principles for next-generation energy storage materials.

The structural motif shared by all W-R crystallographic shear compounds is the $n \times m$ blocks of edge-sharing octahedra, where corner-sharing octahedra occupy the block center, with blocks extending perpendicular to the block plane.[3] Additionally, tetrahedral sites can be present in the block corners to fill void spaces. We recently investigated how the block structure influences Li-ion diffusivity, capacity, and cycle stability in 3×4 $Nb_{12}WO_{33}$, 4×4 $Nb_{14}W_3O_{44}$, and 4×5 $Nb_{16}W_5O_{55}$.[20] Li-ion diffusivity increased with block size, in agreement with theoretical predictions,[16,21,22] and the symmetric 4×4 $Nb_{14}W_3O_{44}$ compound exhibited higher capacity and reversibility than the asymmetric 3×4 $Nb_{12}WO_{33}$ and 4×5 $Nb_{16}W_5O_{55}$. Koçer et al. conducted first-principles density functional theory calculations to understand how the crystallographic shear structure promotes cycle stability.[21] Their computational work revealed that the shear plane plays a key role in an anisotropic lattice expansion/contraction mechanism during lithiation/de-lithiation cycles, which buffers the volume expansion of the material. However, it is unclear how transition metal substitution along the shear plane influences structural stability during cycling. A specific question that our work addresses is "*How does the degree of second order Jahn-Teller distortion, or the off-centering of the* d^0 *transition-metal cations that are octahedrally coordinated by oxygen, influence the structural stability of the compound under repeated ion insertion/de-insertion cycles*."

Another important but underexplored open question in W-R niobium oxide anode materials is *how does elemental substitution influence the reduction-oxidation (redox) mechanisms and Li-ion battery performance?* Koçer et al. hypothesized that the impressive capacity of W-R materials originates from the variety of low energy lithium storage sites with different local environments.[21] However, the community lacks rational design principles to alter the Li-ion binding energetics via substitutional doping. One interesting approach is to explore elemental substitution along the shear plane. Recent first-principles electronic structure calculations by Saber et al. revealed an unconventional redox mechanism upon Li-ion insertion in the $Li_xTiNb_2O_7$ W-R phase that results in the formation of metal–metal bonds between Nb octahedra along the shear plane.[14] This metal dimer redox mechanism significantly impacts the structure by shortening cation-pair distances, which subsequently affects the lattice parameters of the host and can impact Li-ion site preferences as the Li concentration changes.[14,21] An interesting open question that our work addresses is "*How does elemental substitution along the shear change the energetics of the* t_{2g} *orbitals involved in* *metal-metal bonding and, therefore, influence the electrochemically active density of states (DOS) and working potential of the electrode?"*. In this work, we chose to study Mo substitution for W because metal-metal bonding has been reported in molybdenum oxides, such as $LiScMo_3O_8$, and because Mo exhibits the larger SOJT distortion than Nb and W d^0 cations.[23–25]

Finally, an overlooked nuance in W-R material synthesis is "*How does the synthetic procedure (e.g., high-temperature solid-state synthesis, sol-gel growth, or microwave synthesis*[20,26,27]*) influence material crystallinity and purity that ultimately determine the functional properties*?" Subtle differences in experimental conditions can lead to the formation of defect phases, like Wadsley defects, which are not easily identifiable by powder X-ray diffraction (PXRD). These defects, which can involve the intergrowth of another W-R phase within the matrix of another (e.g., $W_4Nb_{26}O_{77}$ in a matrix of $Nb_{12}WO_{33}$), can enhance specific capacity, rate capability, and stability, as seen in the crystallographic shear compound H-Nb_2O_5.[28–30] This raises the question: *how does the community determine if a performance increase in W-R materials is due to intended structure or doping changes, or an unintended minor impurity phase*? To address this question, we systematically investigated how Mo substitution for W influences Li-ion insertion electrochemistry of $Mo_xNb_{12}W_{1-x}O_{33}$. Recognizing that the synthetic procedure likely dictates the crystallinity and phase purity of the final products, we also explored how different synthetic conditions impact the phase purity of the compound, including the addition of Mo.

In this work, we aim to better understand how elemental substitutions and synthetic methods affect the electrochemical performance of W-R crystallographic shear compounds. To tackle these critical questions, we systematically investigated $Mo_xNb_{12}W_{1-x}O_{33}$ compounds synthesized via high temperature solid-state reactions with different reaction conditions to deconvolute elemental substitution versus phase purity effects on electrochemical performance.

We discovered that substituting Mo for W activates multi-electron redox behavior, likely because Mo cations can occupy edge-shared octahedral sites along the shear plane and participate in metal-metal bonding with neighboring Nb octahedra. However, the enhanced capacity in Mo-rich compounds is accompanied by poor cycle stability. We attribute the electrochemical irreversibility to the inability of severely distorted octahedra on the shear plane from "rocking" back and forth during lithiation/de-lithiation cycles. Structural disorder also increases the discharge capacity in a series of defect-rich samples, likely due to the presence of Wadsley defects that lower Li-ion binding energetics.

3.3 Experimental

3.3.1 Synthesis of nearly phase pure W-R compounds

Five $Mo_xNb_{12}W_{1-x}O_{33}$ ($x = 0.00, 0.25, 0.50, 0.75, 1.00$) samples were synthesized by first grinding stoichiometric ratios (12:1:0, 48:3:1, 24:1:1, 48:1:3, 12:0:1) of NbO_2 (Alfa Aesar, 99%), $WO_{2.9}$ (Alfa Aesar, 99%), and MoO_3 (Thermo Scientific, 99%), respectively, using an agate mortar and pestle. In this work, x is defined by the molar ratio of starting precursors. The ground mixtures were pressed into pellets with a hydraulic press (Caver Model: 4350.L) using 2 tons of pressure. The $x = 0.00$, 0.25, and 0.50 pellets were heated in a Thermo Scientific Lindberg Blue M tube furnace from room temperature to 1200°C at a rate of 1°C min^{-1}, held at 1200°C for 12 hours, and then cooled to room temperature at a rate of 1°C min^{-1}. The setpoint temperature and ramp rates were adapted from literature.[1,20] The $x = 0.75$ and 1.0 pellets were heated from room temperature to 900°C, held at 900°C for 12 hours, and then cooled to room temperature at a rate of 10°C min^{-1}, following literature.[31]

3.3.2 Synthesis of defect-rich W-R compounds

Four defect-rich samples, denoted as D-$Mo_xNb_{12}W_{1-x}O_{33}$ compounds (x = 0.00, 0.25, 0.75, 1.00), were synthesized by grinding stoichiometric ratios (12:1:0, 48:3:1, 48:1:3, 12:0:1) of NbO_2, $WO_{2.9}$, and MoO_3, respectively, using an agate mortar and pestle. The ground mixtures were pressed into pellets with a hydraulic press at 2 tons of pressure. The x = 0.0 and 0.25 pellets were heated in the same tube furnace from room temperature (~20°C) to 1200°C at a rate of 10°C min^{-1}, held at 1200°C for one minute, and then cooled to room temperature at a rate of 10°C min^{-1}. The x = 0.75 and 1.0 samples were heated from room temperature to 900°C, held at 900°C for one minute, and then cooled to room temperature at a rate of 10°C min^{-1}. We were unable to prepare x = 0.5 defect-rich samples due to growing concerns that the fast 10°C min^{-1} ramp rate would induce furnace damage.

3.3.3 Sample Characterization

The crystal structures of the compounds were characterized by powder x-ray diffraction (PXRD) using a Bruker D8 Discover DaVinci – Powder Diffractometer (Cu Kα radiation). Scanning electron microscopy (SEM) analyses were performed on a JEOL 6500 field emission SEM. Raman spectroscopy was performed on an Olympus IX-73 optical microscope with a 785 nm Oxxius SA LBX-785HPE laser source and a 20× NA0.95 air objective (Olympus PlanFL N20X). The Raman system was calibrated using the Stokes and anti-Stokes peaks of a Si standard sample at –521 and 521 cm^{-1}, respectively.

Simulated diffraction patterns were generated with VESTA using the $Nb_{12}WO_{33}$ crystallographic information file (CIF) obtained from the Inorganic Crystal Structure Database (ICSD coll. Code 23799). The CIF from the ICSD was changed from the C2 space group to C2/m when conducting the Rietveld refinement for each composition, with the overall occupancy of the tetrahedral changed from 1 to 0.5 due to this unit cell change, allowing for the possibility for tetrahedral occupancy at [0.00 0.25 1.00] and [0.00 0.75 1.00].

3.3.4 Computational details

$Nb_{12}WO_{33}$ and $Nb_{12}MoO_{33}$ structures from the Materials Project database were fully optimized (atoms and lattice vectors) at the PBEsol/pob-TZVP-rev2 level of theory with the CRYSTAL17 code. [32] 92 atom supercells were optimized without symmetry on a dense 6x6x6 k-point grid. Frequency calculations were conducted on the optimized structures to determine the phonon frequencies and the normal modes on a computationally feasible 1x6x1 k-point grid. Analytical Raman intensities were calculated in CRYSTAL17 with the INTRAMAN keyword.[32–34] Experimental conditions such as the temperature 300 K and the Raman laser wavelength (532 nm) were taken into account using the RAMANEXP keyword.

3.3.5 Half-cell construction

Coin cell batteries were constructed in an argon glove box using the following components: stainless steel cases (MTI Corp, CR2032), a stainless-steel wave spring (MTI Corp, CR20WS), a stainless-steel spacer (MTI Corp, CR20-Spacer-05), and a glass microfiber (VWR, 691) separator. The metal oxide composite electrode was prepared by grinding an 8:1:1 ratio of W-R particles, conductive carbon (Super P, Alfa Aesar), and polyvinylidene fluoride binder (PVDF, Sigma Aldrich) in an agate mortar and pestle. The metal oxide composite electrode is the cathode and lithium metal is the anode in this coin cell geometry. This mixture was dispersed in N-methyl pyrrolidone (NMP, Sigma-Aldrich) until the solution was slightly viscous. A doctor blade was used to cast a 100 μm-thick film onto a copper substrate. The film was dried overnight in vacuum at 150°C. The dried film was punched into several ½ inch electrodes and transferred into an argon glove box. Coin cells were constructed with the MTI coin cell case using a ½ inch diameter lithium metal electrode and a 5/8th inch diameter separator with 80.0 µL of electrolyte containing 1M $LiPF_6$ dissolved in a 1:1 volume ratio of ethylene carbonate/dimethyl carbonate (EC/DMC, Sigma Aldrich) was pipetted onto the separator. The cathode was placed on the separator after it had become saturated with electrolyte, followed by the stainless-steel spacer, spring, and finally the end cap. The cells were pressed with 0.9 tons of pressure using a compact digital pressure controlled electric crimper (MTI MSK-160E). The cells rested for 12 hours before electrochemical measurements were performed to allow the electrolyte to fully saturate the separator. Data in this study stems from 3 coin cells for $Nb_{12}WO_{33}$, $Mo_{.25}Nb_{12}W_{.75}O_{33}$, $Mo_{.5}Nb_{12}W_{.5}O_{33}$, $Mo_{.75}Nb_{12}W_{.25}O_{33}$, and $MoNb_{12}O_{33}$ and N = 4-, 2-, 3-, and 4-coin cells for D-$Nb_{12}WO_{33}$, D-$Mo_{.25}Nb_{12}W_{.75}O_{33}$, D-$Mo_{.75}Nb_{12}W_{.25}O_{33}$, and D-$MoNb_{12}O_{33}$, respectively.

3.3.5 Electrochemical Testing

The coin cells were cycled on an Arbin battery tester (LBT-20084) at a C-rate of C/3, in which C-rate is the current which a battery is discharged relative to its theoretical capacity. The theoretical capacity is calculated by, $Q_{theoretical} = nF/3.6M$, where n is the number of electrons transferred per formula unit, F is Faraday's constant, 3.6 is a conversion factor between coulombs and mAh/g, and M is the molecular weight. The C-rate was calculated according to following equation: $I = (Q_{theoretical} \times m)/t$, where I is the current applied, m is the mass of active material, and t is time in hours.

3.4 Results

We synthesized two series of $Mo_xNb_{12}W_{1-x}O_{33}$ W-R samples using different reaction conditions in an attempt to deconvolute how intentional chemical substitution effects (i.e., Mo for W) influences electrochemical properties as opposed to unintentional morphology, crystallinity, and/or phase impurity contributions to the electrochemical properties. Researchers typically synthesize niobium tungsten oxide W-R compounds at high temperatures (>900°C) for long times (>12 h), but it remains unclear how specific reaction temperature and time conditions influence the product phase purity and electrochemical cycling behavior in Li-ion containing electrolytes.[1,20,26,35,36] We hypothesize that maintaining high reaction temperatures for long times promotes the formation of phase pure products and minimizes defect formation, such as Wadsley defects or inter-growth of impurity phases that will be discussed in more detail below.[9,16,30] To test this hypothesis, we synthesized two different Mo-substituted W-R samples using the same precursors but different reaction conditions. To do so, we hand-ground stoichiometric ratios of NbO_2, $WO_{2.9}$, and MoO_3 in a mortar and pestle, pressed the powder into a pellet, and heated both samples to the same set point temperature, but with different ramp rates and setpoint temperature hold times. One reaction condition involved slowly heating (1°C min^{-1}) the sample to the setpoint temperature and maintaining that temperature for 12 h. The other reaction condition involved rapid heating (10°C min^{-1}) and maintaining the set point temperature for only 1 min.

Stoichiometric ratios of NbO_2, $WO_{2.9}$, and MoO_3 were ground by hand in a mortar and pestle, pressed into a pellet, and heated to a setpoint temperature using different ramp rates and setpoint temperature hold times. One reaction condition involved slowly heating (1°C min^{-1}) the sample to the setpoint temperature and maintaining that temperature for 12 h. The other reaction condition involved rapid heating (10°C min^{-1}) and maintaining the set point temperature for only 1 min.

Figure 3.1a compares background subtracted experimental PXRD patterns for the $Mo_xNb_{12}W_{1-x}O_{33}$ compounds that were slowly heated and maintained at the setpoint temperature for 12 h to model diffraction patterns for $Nb_{12}WO_{33}$ (CIF collection code 23799, C2 space group) and $MoNb_{12}WO_{33}$ (C2 space group). All peaks in the experimental diffraction patterns match those in the model patterns, indicating that the reaction condition produces the desired W-R product and no residual NbO_2, $WO_{2.9}$, and MoO_3 starting materials remain after the heating procedure. The peak positions do not shift dramatically with increasing x because W and Mo are isovalent (i.e., VI) in the non-lithiated state and both elements have similar ionic and crystal radii. However, the prominent experimental XRD peak positions located between 23° and 26° 2θ differ from the model pattern (see Figure 3.1b). We performed a Rietveld refinement analysis utilizing a C2/m space group to understand the origin of the peak shift (see Experimental section for details). An example of the Rietveld refinement is shown in Figure A2.1, in which the lattice parameters (a, b, c, and β) where refined. We can see the discrepancy between the experimental and model peak positions is explained through the refinement, with the fit peak positions now closely matching the experiment, indicating that our synthesized samples possess unit cells slightly smaller than the CIF acquired from the ICSD. Furthermore, this analysis revealed each sample contained >95 wt % of the desired $Mo_xNb_{12}W_{1-x}O_{33}$ composition. Therefore, we refer to these samples as nearly phase pure.

The samples heated rapidly and for less total time exhibit diffraction peaks that can also be attributed to the C2/m space group (Figure A2.2), indicating that the short reaction condition also yields products with the desired crystallographic shear structure and composition. However, close examination of the PXRD data revealed peak broadening compared to the nearly phase pure samples (Figure 3.1b). To understand the origin of the XRD peak broadening, we performed Rietveld refinement analysis and included several possible phase impurities, several of which are also W-R crystallographic shear compounds that are known to form under these reaction conditions: $Nb_{14}W_3O_{44}$, H-Nb_2O_5, $Nb_{12}O_{29}$, and $Nb_{22}O_{54}$.[15,19,20,30,37] Introducing one possible phase into the Rietveld analysis procedure effectively reduces the error between the data and the fit. However, we could not conclude from Rietveld error analysis alone which impurity phase is most likely present in these samples. We note that characterizing these materials is challenging through PXRD and Rietveld refinement analysis alone is challenging due to the possibility of transition metals occupying different sites, and the similarity of atomic scattering factor between niobium and molybdenum.[38,39] However, literature evidence strongly suggests that the peak broadening effect is likely due to the presence of other W-R phases or structural defects; Li et al. showed similar PXRD peak broadening effects in H-Nb_2O_5 samples that could be attributed to structural defects that could only be confirmed by high resolution electron microscopy.[40] Other possible explanations for the peak broadening include enhanced strain, crystallite size, twinning, and/or stacking faults.[41–46] Particle size effects cannot entirely explain the peak broadening effect because SEM imaging (Figure A2.3-Figure A2.4) and subsequent particle size analysis (Table A2.1-Table A2.2) revealed similar particle morphologies and dimensions, especially for the $MoNb_{12}O_{33}$ samples. Regardless of the exact origin of the peak broadening, we conclude that quickly ramping the temperature to a setpoint and holding the reaction mixture for a short time promotes defect formation. For these reasons, we refer to the samples synthesized rapidly and for a short react time as defect-rich (D-$Mo_xNb_{12}W_{1-x}O_{33}$). We discuss how impurity phases or structural defects could possibly influence the electrochemical properties in the Discussion section.

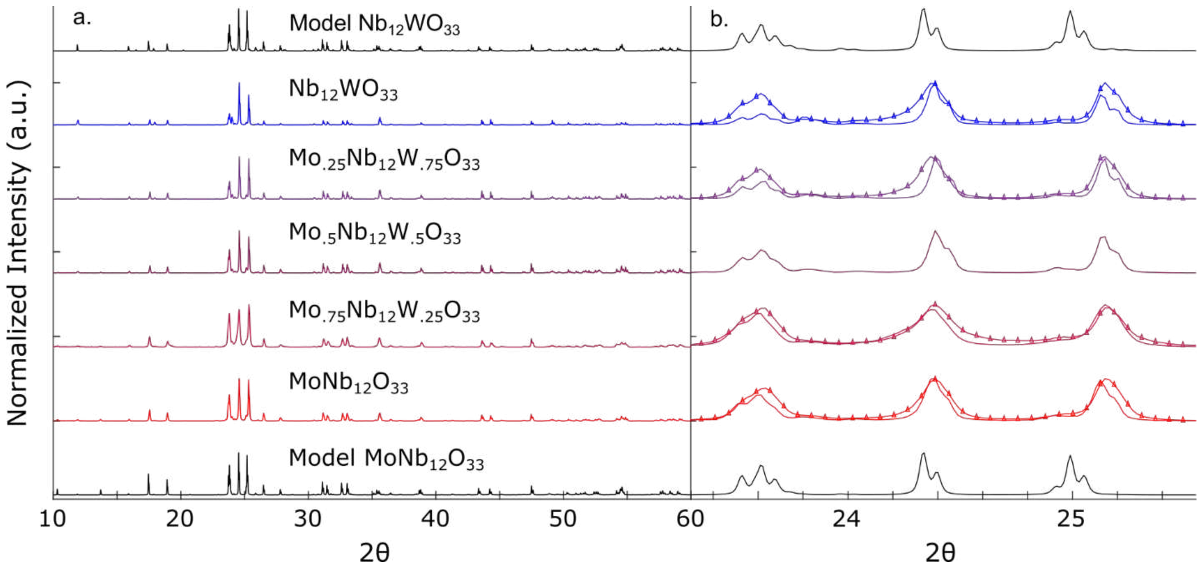

Figure 3.1.1 (a) PXRD patterns of $Mo_xNb_{12}W_{1-x}O_{33}$ compounds synthesized for 12 h. The model $Nb_{12}WO_{33}$ and $MoNb_{12}O_{33}$ patterns were calculated in VESTA software using a crystallographic information file (CIF collection code 23799 with a C2 space group) from the Inorganic Crystal Structure Database (ICSD) (b) Comparison of PXRD patterns in a limited 2θ region for $Mo_xNb_{12}W_{1-x}O_{33}$ compounds synthesized for 12 hours (solid line) and 1 min (solid line connected by triangles). We refer to the samples synthesized for 1 min as defect-rich (D-$Mo_xNb_{12}W_{1-x}O_{33}$) due to the enhanced peak broadening (see main text for details). We normalized the peak intensities in (a-b) with respect to

Next, we utilized Raman spectroscopy to attempt to identify the crystallographic sites that Mo or W atoms occupy in the structure. Density functional theory (DFT) computations predict that Mo^{6+} and W^{6+} + preferentially occupy the tetrahedral sites due to their higher oxidation state than Nb^{5+}.[21] To test this hypothesis, we performed Raman spectroscopy experiments and compared those results to preliminary first principles calculations. We note that assigning and conducting computational Raman spectroscopy is due to the structural complexity of the unit cells.[43] Figure 3.2a-c compares experimental Raman spectra of the nearly phase pure $Nb_{12}WO_{33}$, $Mo_{.5}Nb_{12}W_{.5}O_{33}$, and $MoNb_{12}O_{33}$ samples. Figure A2.5 compares the Raman spectra of $Mo_xNb_{12}W_{1-x}O_{33}$ and D-$Mo_xNb_{12}W_{1-x}O_{33}$ samples. The peak intensity ratios change but the peak positions do not, indicating the local bonding environments are similar between the two synthetic conditions, consistent with the XRD results, showing each samples are similar crystallographic phases. We focus our discussion on the $Mo_xNb_{12}W_{1-x}O_{33}$ spectra because the results and interpretations apply to the D-$Mo_xNb_{12}W_{1-x}O_{33}$ samples too.

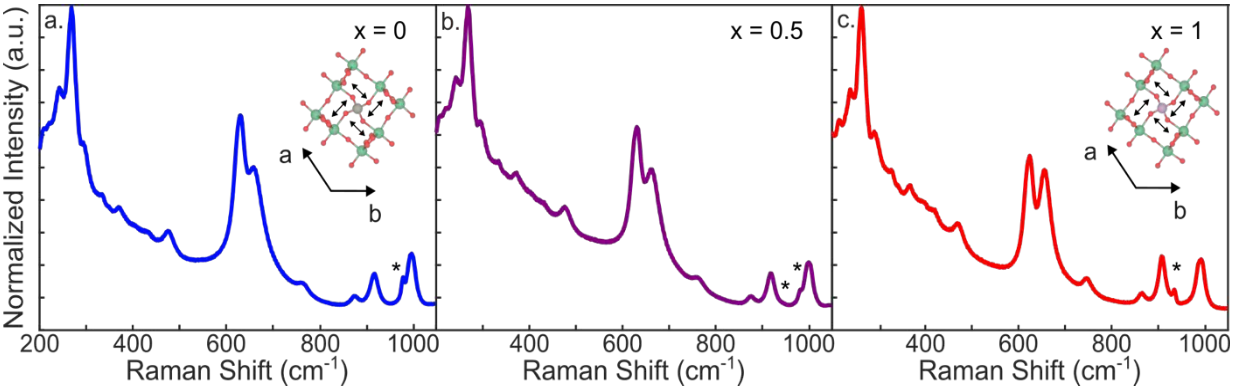

Figure 3.2. Experimental Raman spectra for (a) $Nb_{12}WO_{33}$, (b) $Mo_{.5}Nb_{12}W_{.5}O_{33}$, and (c) $MoNb_{12}O_{33}$.

Distinct modes appear for the x = 0 and x = 1 compositions, which highlights one powerful aspect of experimental and computational Raman spectroscopy. The simulated mode at 979 cm^{-1} corresponds to a W-O stretch in a tetrahedral coordination environment. This mode appears in x = 0 and x = 0.5 spectra (Figure 3.2a-b) but is absent in the W-free compound (Figure 3.2c). On the other hand, the simulated mode at 937 cm^{-1} corresponds to a Mo-O stretch in a tetrahedral coordination environment. This mode appears in x = 0.5 and x = 1.0 (Figure 3.2b-c) but is absent in the Mo-free compound (Figure 3.2a). Hence, we conclude that Mo and W occupy the tetrahedral sites in $Mo_xNb_{12}W_{1-x}O_{33}$, in agreement with computational predictions and neutron diffraction studies.[21,38] Quantifying the tetrahedral site occupancies using Raman spectroscopy alone is challenging and goes beyond the scope of this study. We note that some experimental Raman modes remain unassigned or appear significantly shifted from the theoretically predicted values. These differences are likely because the computational Raman results assumed W and Mo occupy tetrahedral sites, but there is a non-zero probability that these transition metals occupy other sites in the structure.[38] While there is general agreement between simulated and experimental spectra for $Nb_{12}WO_{33}$, there is general disagreement between simulation and experiment in the high frequency range for $MoNb_{12}O_{33}$. The simulated modes appear systematically higher in energy than the experimentally observed peaks. This disagreement could also be due to the fact that simulations use lattice parameters from a database file rather than the values obtained from Rietveld refinement, which could affect the predicted vibrational mode energies. Regardless of the origin of the disagreement between theory and experiment, Raman spectroscopy confirmed that W and Mo atoms can occupy the tetrahedral sites in the unit cell.

Having characterized the structure and transition metal site occupancy of the $Mo_xNb_{12}W_{1-x}O_{33}$ compounds, we investigated their electrochemical behavior and performance as Li-ion insertion hosts. We constructed coin cells by mixing metal oxide host material, conductive carbon, and PVDF polymer binder in an 8:1:1 ratio. This ratio was utilized to help minimize the *iR* loss due to the intrinsically poorly conductive oxide particles and aid in the mechanical stability and electrical contact upon cycling, the ratio was not optimized for battery performance.[48,49] Additionally, we cycled all cells at a slow C/3 rate to minimize *iR* loss effects in the insulating metal oxide electrodes.

Figure 3.3a-e shows the charge/discharge behavior for nearly phase pure $Mo_xNb_{12}W_{1-x}O_{33}$ compounds. The compounds exhibit qualitatively similar voltage profiles upon lithiation/de-lithiation (i.e., discharge/charge cycles). Upon lithiation, the potential quickly decreases from 3 V to approximately 2 V vs Li/Li^+ until a plateau region appears at approximately $y = 1$, where y is the number of Li-ions inserted per formula unit. The plateau region persists to approximately $y = 5$. Then, the potential monotonically decreases until the 1 V voltage cutoff limit defined in our experiment. We observed similar charge-discharge profiles for the D-$Mo_xNb_{12}W_{1-x}O_{33}$ compounds (Figure A2.8).

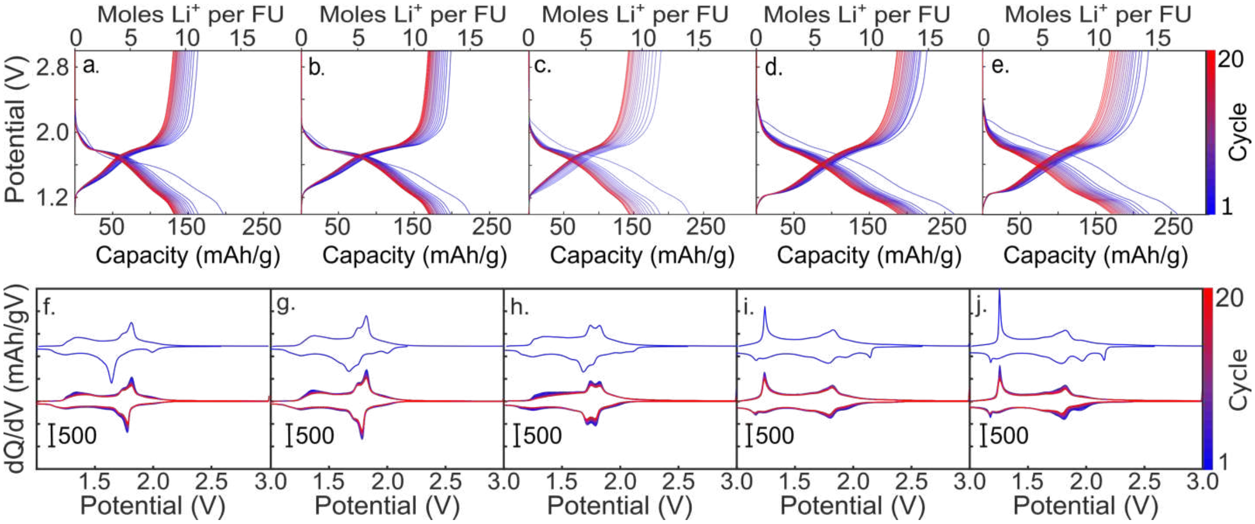

Figure 3.3. (a-e) Charge-discharge behavior for nearly phase pure $Mo_xNb_{12}W_{1-x}O_{33}$ compounds measured at a C/3 rate for 20 cycles. (f-j) Differential capacity plots obtained from the charge-discharge data. The upper blue trace shows the first charge-discharge cycle, and the lower plots represent cycles 2-20.

Although the profiles in Figure 3.3a-e appear qualitatively similar, analyzing the charge-discharge data reveals several *x*-dependent trends. First, the plateau region exhibits a slight negative slope, and the slope value increases with x, as evidenced by broader peaks in dQ/dV plots (Figure 3.3-j). This enhanced sloping profile feature observed for the Mo-rich compounds is problematic for Li-ion battery applications because a continuously decreasing voltage results in continuous power loss during discharge. Second, all samples exhibit a significant capacity loss between cycles 1 and 2 (Figure A2.10a), followed by a continuous capacity fade with additional cycling. The capacity loss rate generally increases with x (Figure A2.10), possibly due to irreversible structural distortions related to distorted Mo octahedra along the shear plane (see Discussion section for further details). However, Figure A2.11 and Figure A2.12 shows after approximately 4 cycles, the average coulombic efficiency and relative capacity loss for each composition for both $Mo_xNb_{12}W_{1-x}O_{33}$ and D-$Mo_xNb_{12}W_{1-x}O_{33}$ begins for plateau, highlighting the reversibility intrinsic to these unoptimized materials. Finally, the most significant observation from Figure 3.3 is that the discharge capacity systematically increases with x (Figure 3.4, filled circles). In fact, the discharge capacity for $Mo_{.75}Nb_{12}W_{.25}O_{33}$ and $MoNb_{12}O_{33}$ exceed the theoretical capacity values for single-electron redox behavior. This trend suggests that substituting Mo for W activates a multi-electron redox behavior whereby transition metal cations undergo multiple reduction events (either Nb^{5+} to Nb^{3+} or Mo^{6+} to Mo^{4+}). Furthermore, we observed that defect-rich samples display similar constant current plots (Figure A2.8) and generally exhibit greater discharge capacity than the nearly phase pure compounds (see open square symbols in Figure 3.4), possibly due to Wadsley defects (see Discussion section).

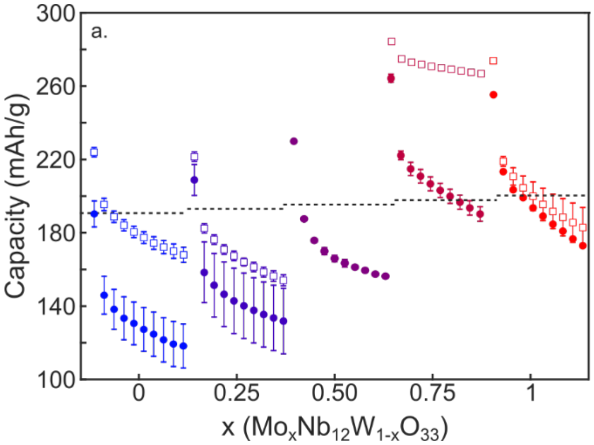

Figure 3.4. Discharge capacity versus cycle number (displaying odd cycles only for clarity) for nearly phase pure $Mo_xNb_{12}W_{1-x}O_{33}$. The data points represent average values (see Experimental Methods), and the error bars represent the standard error of the mean. The filled and hollow markers represent $Mo_xNb_{12}W_{1-x}O_{33}$ and D-$Mo_xNb_{12}W_{1-x}O_{33}$ samples, respectively. The horizontal dashed line indicates the theoretical capacity for each composition, assuming single electron redox per transition metal cation in the unit cell.

Next, we examined the differential capacity (dQ/dV) plots to better understand how Mo-substitution affects the ion insertion electrochemistry and electrochemically accessible density of states (DOS) shown in Figure 3.3f-j. We discuss the positive potential region (potentials greater than 2 V) of the dQ/dV plots first. Upon inserting a single Li-ion per formula unit in the pristine $x = 0$ and $x = 0.25$ samples for the first time (top traces in Figure 3.3f-g), a single peak appears near 2 V (specifically 1.991 and 1.999 V for $x = 0$ and $x = 0.25$ samples, respectively). These negative dQ/dV peaks do not exhibit a corresponding positive dQ/dV feature upon de-lithiation and do not appear in additional cycles (bottom traces in Figure 3.3f-j). Both observations suggest the first Li-ion insertion event is irreversible. The peak broadens in the $x = 0.5$ compound and eventually splits into two discernable peaks for the *x* = 0.75 and *x* = 1.0 compounds. Again, we observed no corresponding positive d*Q*/d*V* feature, suggesting the initial lithiation events are irreversible. In summary, Mo substitution introduces new electrochemically active states at more positive potentials than the W-based compounds.

Next, we discuss the prominent d*Q*/d*V* features between 1.5 and 2.0 V. Upon lithiation, the *x* = 0 compound exhibits a sharp negative d*Q*/d*V* peak at 1.641 V that accounts for approximately 6 Li-ions per formula unit. The corresponding positive d*Q*/d*V* feature appears at significantly more positive potentials (1.8 V). After the significant capacity loss event between cycles 1-2, which we believe is associated with the first Li-ion insertion event, the negative d*Q*/d*V* peak shifts to more positive potentials and occurs at nearly the same potential as the positive 1.7 V d*Q*/d*V* feature during cycle 1. The peak shift for the negative d*Q*/d*V* peak could be explained by an electrical conductivity improvement upon irreversibly introducing 1 Li-ion per formula unit in the initially insulting oxide phase.[20] In this scenario, the dramatic conductivity increase upon lithiation could lower the overpotential associated with filling the electrochemically active DOS. Interestingly, this peak shift effect is most pronounced in the *x* = 0 compound. Substituting Mo for W results in relatively reversible and symmetric d*Q*/d*V* features between 1.5 and 2.0 V, which suggests that the Mo-derived electrochemically active DOS is distinct from W-derived states.

Finally, the region between 1.5 and 1.0 V accounts for approximately, 6-10 Li-ions per formula unit, depending on x. For x < 0.5, a broad peak appears at 1.2 V in the dQ/dV plots (Figure 3.3h). Unlike other peaks at more positive potentials, the negative dQ/dV peak exhibits a corresponding positive peak and neither feature shifts with additional cycle numbers. As Mo content increases, the negative d*Q*/d*V* peak sharpens. Additionally, we observe similar trends in the d*Q*/d*V* plots for D-$Mo_xNb_{12}W_{1-x}O_{33}$, shown in Figure A2.9. These observations suggest a transition from delocalized to localized electrochemically active DOS as Mo substitutes for W (i.e., as x increases). In summary, the dQ/dV plots show that Mo substitution introduces new electrochemically active DOS. The Discussion section considers how the Mo-derived DOS contributes to enhanced capacity.

3.5 Discussion

Here we discuss possible explanations for our 3 key results: (1) defective W-rich W-R samples exhibit greater capacities than nearly phase pure compounds; (2) Mo substitution for W increases capacity and enables multi-electron redox behavior; and (3) Mo substitution enhances capacity fade.

First, we discuss the possible defect phases in the D-$Mo_xNb_{12}W_{1-x}O_{33}$ samples and how those phases could contribute to capacity enhancement. Recall the PXRD patterns for the slowly heated $Mo_xNb_{12}W_{1-x}O_{33}$ samples exhibit narrow, well-defined peaks compared to the rapidly heated D-$Mo_xNb_{12}W_{1-x}O_{33}$ samples (Figure 3.1c-f). The presence of Wadsley defects, or coherent intergrowths of a W-R family member in another matrix, could possibly explain the peak broadening.[8,9,30,50] For example, $Nb_{26}W_4O_{77}$ is an ordered intergrowth of $Nb_{12}WO_{33}$ and $Nb_{14}W_3O_{44}$.[28,29,50] $Nb_{15}W_6O_{55}$ and H-Nb_2O_5 represent other potential defect phases that can form under the reaction conditions employed herein.[1,15,20] These defects may only extend half a unit cell and, therefore, may not appear in PXRD data.

Wadsley defects can enhance Li-ion insertion capacity of W-R electrodes. Li et al. revealed local rearrangements of [NbO_6] octahedra in micrometer-sized H-Nb_2O_5 using high resolution transmission electron microcopy and showed that those planar Wadsley defects resulted in higher specific capacity, rate capability, and stability compared to more crystalline H-Nb_2O_5 and T-Nb_2O_5 electrodes.[30] The authors attributed the higher capacity to strong Li adsorption (i.e., lower binding energy) on planar defects. Specifically, DFT calculations provide lower Li-ion adsorption energies for defective H-Nb_2O_5, when compared to crystalline H-Nb_2O_5, providing support that planar defects can improve the capacity of W-R materials. The authors also claimed that the planar defects relieve strain and minimize volume change, enhancing stability. Similar trends appear in our data (Figure 3.3). Hence, one interesting future direction toward developing structure-property relationships in W-R anode materials is to systematically introduce Wadsley defects and study how their structure, composition, and concentration influence capacity, rate capability, and cycling stability.

Another significant result from this work is that Mo substitution for W increases capacity of W-R electrodes beyond 1 electron per transition metal site. One hypothesis for this capacity increase is that Mo atoms create local Li-ion binding environments that lower Li-ion binding energies.[21] A literature survey conducted by Ok et al. discovered that Mo is prone to a higher degree of distortion compared to Nb and W.[24] Hence, severely distorted Mo octahedra along the shear plane could create local environments with lower Li-ion binding energetics, resulting in higher capacity.[30] However, the same octahedral tilting responsible for enhanced capacity is also likely responsible for cycling instability. During lithiation, the distorted Mo octahedra along the shear plane become less off-centered as the Mo oxidation state decreases from Mo^{6+} to Mo^{5+}.[2,21] We hypothesize that structural stability depends on the ability of Mo octahedra along the shear plane to "rock" back and forth during lithiation/de-lithiation cycles. An interesting future research direction is to test the hypothesis that reversible Mo octahedral tilting is essential for long-term cycling stability.

An alternative explanation for enhanced capacity in $MoNb_{12}O_{33}$ is metal-metal bonding between edge shared transition metal octahedra along the shear plane. Saber et al. recently performed electronic structure calculations as a function of lithiation in $TiNb_2O_7$, another W-R crystallographic shear compound, and discovered metal-metal bonding can occur at low levels of lithiation.[2] Metal-metal bonding occurs between d_{xy} orbitals of the edge shared octahedra along the shear plane, forming bonding and anti-bonding orbitals (see reference 2. The same phenomenon occurs in PNb_9O_{26} and VNb_9O_{26}; lithiation induces Nb-Nb orbital overlap.[14] According to electronic structure calculations, a signature of metal-metal bonding is electronic states below the Fermi level. Experimentally, we observed sharp dQ/dV peaks at positive potentials (>2.0 V in Figure 3.3f-j) upon inserting about 1 Li-ion per formula unit in each W-R compound. Interestingly, a 200-300 mV gap exists between the sharp dQ/dV peaks and the next major dQ/dV feature. This gap could represent the energy gap between the localized states below the Fermi level predicted by Saber et al. Therefore, we assign the high potential dQ/dV peaks to the electrochemically accessible metal-metal bonding states predicted by Saber et al.[2] Filling these localized states with electrons is favorable, but removing electrons from these states is not because we do not observe a corresponding sharp positive dQ/dV peak feature at positive potentials. This electrochemical irreversibility suggests that metal-metal bonding induces permanent structural rearrangements that do not permit full electrochemical oxidation, which could limit optoelectronic device applications such as electrochromic smart windows, as well as effects the initial and subsequent discharge capacities in this study.

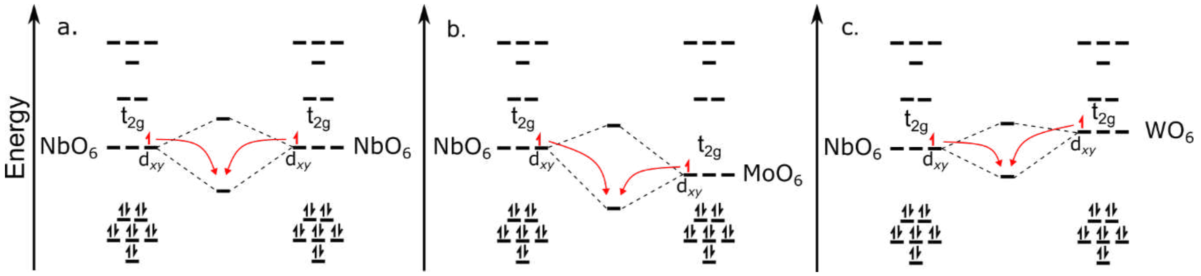

Figure 3.5. Cartoon illustration showing relative energetics upon forming metal-metal bonds between the following edge shared octahedra: (a) NbO_6-NbO_6, (b) NbO_6-MoO_6, and (c) NbO_6-WO_6.

Figure 3.5 schematically shows how the metal-metal bonding mechanism explains why the initial dQ/dV peak shifts to more positive potentials as x increases in $Mo_xNb_{12}W_{1-x}O_{33}$. Figure 3.5a illustrates the homodimer case for two neighboring edge-shared Nb octahedra. Bonding and anti-bonding orbitals form due to metal-metal bonding between two d_{xy} orbitals. The situation changes for the heterodimer Mo-Nb and W-Nb cases. Mo has a lower principal quantum number than W, which shifts the metal-metal bonding orbital to lower energy for Mo-Nb edge shared octahedra versus the W-Nb case (see Figure 3.5b-c). Hence, Mo substitution for W introduces electrochemically active states that accept electrons at more positive potentials than in the W-based niobium oxide compounds. We also hypothesize that fractional occupancy of Mo octahedra along the shear plane is larger than W octahedra because Mo generally forms octahedral structures more readily in environments where steric effects are significant due to its smaller size compared to W. In this scenario, the number density of low-energy bonding states increases with x, and these states are likely responsible for the enhanced capacity in $Mo_xNb_{12}W_{1-x}O_{33}$.

3.6 Conclusion

We synthesized a series of molybdenum substituted Nb-W-O compounds with different levels of disorder to investigate how elemental composition and defects influence the electrochemical performance for high-rate energy storage applications. The discharge capacity increases with increased molybdenum concentrations for both $Mo_xNb_{12}W_{1-x}O_{33}$ and defective D-

$Mo_xNb_{12}W_{1-x}O_{33}$, suggesting that molybdenum substitution is a promising method to improve discharge capacities in Nb-W-O shear compounds. However, increasing molybdenum concentration results in irreversible cycling, with the more molybdenum rich compounds possessing larger capacity decays for both $Mo_xNb_{12}W_{1-x}O_{33}$ and D-$Mo_xNb_{12}W_{1-x}O_{33}$. This irreversibly may be due to a variety of factors, such as Mo substitution lowering the Li-ion binding energies and structural changes during lithiation/delithiation that result in lithium trapping. This is evident in the charge/discharge plots for each composition, which become steeper and more sloped with increasing molybdenum, limiting their ability to deliver constant power in energy storage systems. Another possible explanation for the capacity loss could be due to metal-metal bonding forming low energy orbitals that populate with electrons early when cycling. Molybdenum has a lower principal quantum number than W, which results in lower energy orbitals. These lower energy orbitals result in increasing the potential in which charge is stored and the active material is reduced. By increasing the potential of the reduction event, the potential in which oxidation occurs is also increased. Lastly, each D-$Mo_xNb_{12}W_{1-x}O_{33}$ sample possesses higher discharge capacities when compared to their more crystalline counterparts, indicating that increasing the disorder of the system is a method to alter the electrochemical performance of W-R compounds. The structure-property relationships reported here should extend to other W-R materials and guide the development of future W-R compounds for energy storage applications.

3.7 References

(1) Griffith, K. J.; Wiaderek, K. M.; Cibin, G.; Marbella, L. E.; Grey, C. P. Niobium Tungsten Oxides for High-Rate Lithium-Ion Energy Storage. *Nature* **2018**, *559* (7715), 556–563. https://doi.org/10.1038/s41586-018-0347-0.

(2) Saber, M.; Behara, S. S.; Van der Ven, A. Redox Mechanisms, Structural Changes, and Electrochemistry of the Wadsley–Roth LixTiNb2O7 Electrode Material. *Chem. Mater.* **2023**, *35* (22), 9657–9668. https://doi.org/10.1021/acs.chemmater.3c02003.

(3) Roth, R. S.; Wadsley, A. D. Multiple Phase Formation in the Binary System Nb_2O_5–WO_3. I. Preparation and Identification of Phases. *Acta Crystallogr.* **1965**, *19* (1), 26–32. https://doi.org/10.1107/S0365110X65002712.

(4) Roth, R. S.; Wadsley, A. D. Multiple Phase Formation in the Binary System Nb_2O_5–WO_3. II. The Structure of the Monoclinic Phases $WNb_{12}O_{33}$ and $W_5Nb_{16}O_{55}$. *Acta Crystallogr.* **1965**, *19* (1), 32–38. https://doi.org/10.1107/S0365110X65002724.

(5) Roth, R. S.; Wadsley, A. D. Multiple Phase Formation in the Binary System Nb_2O_5–WO_3. III. The Structures of the Tetragonal Phases $W_3Nb_{14}O_{44}$ and $W_8Nb_{18}O_{69}$. *Acta Crystallogr.* **1965**, *19* (1), 38–42. https://doi.org/10.1107/S0365110X65002736.

(6) Roth, R. S.; Wadsley, A. D. Multiple Phase Formation in the Binary System Nb_2O_5–WO_3. IV. The Block Principle. *Acta Crystallogr.* **1965**, *19* (1), 42–47. https://doi.org/10.1107/S0365110X65002748.

(7) Andersson, S.; Mumme, W. G.; Wadsley, A. D. Multiple Phase Formation in the Binary System Nb_2O_5–WO_3. V. The Structure of $W_4Nb_{26}O_{77}$, an Ordered Intergrowth of the Adjoining Compounds $WNb_{12}O_{33}$ and $W_3Nb_{14}O_{44}$. *Acta Crystallogr.* **1966**, *21* (5), 802–808. https://doi.org/10.1107/S0365110X66003852.

(8) Allpress, J. G.; Sanders, J. V.; Wadsley, A. D. Multiple Phase Formation in the Binary System Nb_2O_5–WO_3. VI. Electron Microscopic Observation and Evaluation of Non-Periodic Shear Structures. *Acta Crystallogr. B* **1969**, *25* (6), 1156–1164. https://doi.org/10.1107/S0567740869003669.

(9) Allpress, J. G.; Wadsley, A. D. Multiple Phase Formation in the Binary System Nb_2O_5-WO_3 VII. Intergrowth of H-Nb2O5 and WNb12O33. *J. Solid State Chem.* **1969**, *1* (1), 28–38. https://doi.org/10.1016/0022-4596(69)90005-X.

(10) Roth, R. S.; Wadsley, A. D. Mixed Oxides of Titanium and Niobium: The Crystal Structure of $TiNb_{24}O_{62}$ (TiO_2-$12Nb_2O_5$). *Acta Crystallogr.* **1965**, *18* (4), 724–730. https://doi.org/10.1107/S0365110X65001664.

(11) Cava, R. J. Lithium Insertion in Wadsley-Roth Phases Based on Niobium Oxide. *J. Electrochem. Soc.* **1983**, *130* (12), 2345. https://doi.org/10.1149/1.2119583.

(12) Ding, H.; Song, Z.; Zhang, H.; Zhang, H.; Li, X. Niobium-Based Oxide Anodes toward Fast and Safe Energy Storage: A Review. *Mater. Today Nano* **2020**, *11*, 100082. https://doi.org/10.1016/j.mtnano.2020.100082.

(13) Deng, Q.; Fu, Y.; Zhu, C.; Yu, Y. Niobium-Based Oxides Toward Advanced Electrochemical Energy Storage: Recent Advances and Challenges. *Small* **2019**, *15* (32), 1804884. https://doi.org/10.1002/smll.201804884.

(14) Preefer, M. B.; Saber, M.; Wei, Q.; Bashian, N. H.; Bocarsly, J. D.; Zhang, W.; Lee, G.; Milam-guerrero, J.; Howard, E. S.; Vincent, R. C.; Melot, B. C.; Ven, A. V. D.; Seshadri, R.; Dunn, B. S. Multielectron Redox and Insulator-to-Metal Transition upon Lithium Insertion in the Fast-Charging, Wadsley-Roth Phase PNb_9O_{25}. **2020**. https://doi.org/10.1021/acs.chemmater.0c00560.

(15) Griffith, K. J.; Forse, A. C.; Griffin, J. M.; Grey, C. P. High-Rate Intercalation without Nanostructuring in Metastable Nb_2O_5 Bronze Phases. *J. Am. Chem. Soc.* **2016**, *138* (28), 8888–8899. https://doi.org/10.1021/jacs.6b04345.

(16) Griffith, K. J.; Grey, C. P. Superionic Lithium Intercalation through 2 × 2 Nm 2 Columns in the Crystallographic Shear Phase $Nb_{18}W_8O_{69}$. *Chem. Mater.* **2020**, *32* (9), 3860–3868. https://doi.org/10.1021/acs.chemmater.9b05403.

(17) Griffith, K. J.; Seymour, I. D.; Hope, M. A.; Butala, M. M.; Lamontagne, L. K.; Preefer, M. B.; Koçer, C. P.; Henkelman, G.; Morris, A. J.; Cliffe, M. J.; Dutton, S. E.; Grey, C. P. Ionic and Electronic Conduction in $TiNb_2O_7$. *J. Am. Chem. Soc.* **2019**, *141* (42), 16706–16725. https://doi.org/10.1021/jacs.9b06669.

(18) Griffith, K. J.; Senyshyn, A.; Grey, C. P. Structural Stability from Crystallographic Shear in TiO_2-Nb_2O_5 Phases: Cation Ordering and Lithiation Behavior of $TiNb_{24}O_{62}$. *Inorg. Chem.* **2017**, *56* (7), 4002–4010. https://doi.org/10.1021/acs.inorgchem.6b03154.

(19) Cheng, Q.; Chen, J.; Zhao, J.; Li, F. A V-Doped $W_3Nb_{14}O_{44}$ Anode in a Wadsley–Roth Structure for Ultra-Fast Lithium-Ion Half/Full Batteries. *New J. Chem.* **2023**, *47* (42), 19537–19545. https://doi.org/10.1039/D3NJ03462C.

(20) Salzer, L. D.; Diamond, B.; Nieto, K.; Evans, R. C.; Prieto, A. L.; Sambur, J. B. Structure–Property Relationships in High-Rate Anode Materials Based on Niobium Tungsten Oxide Shear Structures. *ACS Appl. Energy Mater.* **2023**, *6* (3), 1685–1691. https://doi.org/10.1021/acsaem.2c03573.

(21) Koçer, C. P.; Griffith, K. J.; Grey, C. P.; Morris, A. J. Cation Disorder and Lithium Insertion Mechanism of Wadsley-Roth Crystallographic Shear Phases from First Principles. *J. Am. Chem. Soc.* **2019**, *141* (38). https://doi.org/10.1021/jacs.9b06316.

(22) Koçer, C. P.; Griffith, K. J.; Grey, C. P.; Morris, A. J. Lithium Diffusion in Niobium Tungsten Oxide Shear Structures. *Chem. Mater.* **2020**. https://doi.org/10.1021/acs.chemmater.0c00483.

(23) Burdett, J. K.; Hughbanks, T. Aspects of Metal-Metal Bonding in Early-Transition-Metal Dioxides. *Inorg. Chem.* **1985**, *24* (12), 1741–1750. https://doi.org/10.1021/ic00206a006.

(24) Ok, K. M.; Halasyamani, P. S.; Casanova, D.; Llunell, M.; Alemany, P.; Alvarez, S. Distortions in Octahedrally Coordinated d ^{0} Transition Metal Oxides: A Continuous Symmetry Measures Approach. *Chem. Mater.* **2006**, *18* (14), 3176–3183. https://doi.org/10.1021/cm0604817.

(25) Wyckoff, K. E.; Kaufman, J. L.; Baek, S. W.; Dolle, C.; Zak, J. J.; Bienz, J.; Kautzsch, L.; Vincent, R. C.; Zohar, A.; See, K. A.; Eggeler, Y. M.; Pilon, L.; Van der Ven, A.; Seshadri, R. Metal–Metal Bonding as an Electrode Design Principle in the Low-Strain Cluster Compound $LiScMo_3O_8$. *J. Am. Chem. Soc.* **2022**, *144* (13), 5841–5854. https://doi.org/10.1021/jacs.1c12070.

(26) Saritha, D.; Pralong, V.; Varadaraju, U. V.; Raveau, B. Electrochemical Li Insertion Studies on $WNb_{12}O_{33}$—A Shear ReO_3 Type Structure. *J. Solid State Chem.* **2010**, *183* (5), 988–993. https://doi.org/10.1016/j.jssc.2010.03.003.

(27) Faraji, S.; Ani, F. N. Microwave-Assisted Synthesis of Metal Oxide/Hydroxide Composite Electrodes for High Power Supercapacitors - A Review. *J. Power Sources* **2014**, *263*, 338–360. https://doi.org/10.1016/j.jpowsour.2014.03.144.

(28) Andersson, S.; Mumme, W. G.; Wadsley, A. D. Multiple Phase Formation in the Binary System Nb_2O_5–WO_3. The Structure of $W_4Nb_{26}O_{77}$, an Ordered Intergrowth of the Adjoining Compounds $WNb_{12}O_{33}$ and $W_3Nb_{14}O_{44}$ - Andersson - 1966 - Acta Crystallographica - Wiley Online Library. *Acta Crystallogr.* **1966**, *21*.

(29) Li, D. X.; Kuo, K. H. High-Resolution Electron Microscopy of Defects in $W_4Nb_{26}O_{77}$. *J. Solid State Chem.* **1985**, *56* (2), 236–240. https://doi.org/10.1016/0022-4596(85)90061-1.

(30) Li, T.; Nam, G.; Liu, K.; Wang, J.-H.; Zhao, B.; Ding, Y.; Soule, L.; Avdeev, M.; Luo, Z.; Zhang, W.; Yuan, T.; Jing, P.; Gyu Kim, M.; Song, Y.; Liu, M. A Niobium Oxide with a Shear Structure and Planar Defects for High-Power Lithium Ion Batteries. *Energy Environ. Sci.* **2022**, *15* (1), 254–264. https://doi.org/10.1039/D1EE02664J.

(31) Zhu, X.; Xu, J.; Luo, Y.; Fu, Q.; Liang, G.; Luo, L.; Chen, Y.; Lin, C.; Zhao, X. S. $MoNb_{12}O_{33}$ as a New Anode Material for High-Capacity, Safe, Rapid and Durable Li^+ Storage: Structural Characteristics, Electrochemical Properties and Working Mechanisms. *J. Mater. Chem. A* **2019**, *7* (11), 6522–6532. https://doi.org/10.1039/c9ta00309f.

(32) Dovesi, R.; Erba, A.; Orlando, R.; Zicovich-Wilson, C. M.; Civalleri, B.; Maschio, L.; Rérat, M.; Casassa, S.; Baima, J.; Salustro, S.; Kirtman, B. Quantum-Mechanical Condensed

Matter Simulations with CRYSTAL. *WIREs Comput. Mol. Sci.* **2018**, *8* (4), e1360. https://doi.org/10.1002/wcms.1360.

(33) Maschio, L.; Kirtman, B.; Rérat, M.; Orlando, R.; Dovesi, R. *Ab Initio* Analytical Raman Intensities for Periodic Systems through a Coupled Perturbed Hartree-Fock/Kohn-Sham Method in an Atomic Orbital Basis. I. Theory. *J. Chem. Phys.* **2013**, *139* (16), 164101. https://doi.org/10.1063/1.4824442.

(34) Maschio, L.; Kirtman, B.; Rérat, M.; Orlando, R.; Dovesi, R. *Ab Initio* Analytical Raman Intensities for Periodic Systems through a Coupled Perturbed Hartree-Fock/Kohn-Sham Method in an Atomic Orbital Basis. II. Validation and Comparison with Experiments. *J. Chem. Phys.* **2013**, *139* (16), 164102. https://doi.org/10.1063/1.4824443.

(35) Lakhnot, A. S.; Gupta, T.; Singh, Y.; Hundekar, P.; Jain, R.; Han, F.; Koratkar, N. Aqueous Lithium-Ion Batteries with Niobium Tungsten Oxide Anodes for Superior Volumetric and Rate Capability. *Energy Storage Mater.* **2020**, *27*, 506–513. https://doi.org/10.1016/j.ensm.2019.12.012.

(36) Krumeich, F. The Complex Crystal Chemistry of Niobium Tungsten Oxides. *Chem. Mater.* **2022**, *34* (3), 911–934. https://doi.org/10.1021/acs.chemmater.1c03723.

(37) Cava, R. J.; Batlogg, B.; Krajewski, J. J.; Poulsen, H. F.; Gammel, P.; Peck, W. F.; Rupp, L. W. Electrical and Magnetic Properties of $Nb_2O_{5-\delta}$ Crystallographic Shear Structures. *Phys. Rev. B* **1991**, *44* (13), 6973–6981. https://doi.org/10.1103/PhysRevB.44.6973.

(38) Cheetham, A. K.; Allen, N.C. Cation Distribution in the Complex Oxide, $W_3Nb_{14}O_{44}$; a Time-of-Flight Neutron Diffraction Study. *J Chem Soc Commun* **1983**, 3.

(39) Maslen, E. N.; Fox, A. G.; O'Keefe, M. A. Atomic Scattering Factor. *Int. Tables Crystallogr. Vol. C* **2006**, *C*, 554–595. https://doi.org/10.1107/97809553602060000600.

(40) Hahn, B. P.; Long, J. W.; Mansour, A. N.; Pettigrew, K. A.; Osofsky, M. S.; Rolison, D. R. Electrochemical Li-Ion Storage in Defect Spinel Iron Oxides: The Critical Role of Cation Vacancies. *Energy Environ. Sci.* **2011**, *4* (4), 1495–1502. https://doi.org/10.1039/c0ee00819b.

(41) Muniz, F. T. L.; Miranda, M. a. R.; Morilla dos Santos, C.; Sasaki, J. M. The Scherrer Equation and the Dynamical Theory of X-Ray Diffraction. *Acta Crystallogr. Sect. Found. Adv.* **2016**, *72* (3), 385–390. https://doi.org/10.1107/S205327331600365X.

(42) Nath, D.; Singh, F.; Das, R. X-Ray Diffraction Analysis by Williamson-Hall, Halder-Wagner and Size-Strain Plot Methods of CdSe Nanoparticles- a Comparative Study. *Mater. Chem. Phys.* **2020**, *239*, 122021. https://doi.org/10.1016/j.matchemphys.2019.122021.

(43) Yogamalar, R.; Srinivasan, R.; Vinu, A.; Ariga, K.; Bose, A. C. X-Ray Peak Broadening Analysis in ZnO Nanoparticles. *Solid State Commun.* **2009**, *149* (43), 1919–1923. https://doi.org/10.1016/j.ssc.2009.07.043.

(44) Balogh, L.; Ribárik, G.; Ungár, T. Stacking Faults and Twin Boundaries in Fcc Crystals Determined by X-Ray Diffraction Profile Analysis. *J. Appl. Phys.* **2006**, *100* (2), 023512. https://doi.org/10.1063/1.2216195.

(45) Warren, B. E. X-Ray Studies of Deformed Metals. *Prog. Met. Phys.* **1959**, *8*, 147–202. https://doi.org/10.1016/0502-8205(59)90015-2.

(46) Pujar, V. V.; Cawley, J. D. Effect of Stacking Faults on the X-Ray Diffraction Profiles of β-SiC Powders. *J. Am. Ceram. Soc.* **1995**, *78* (3), 774–782. https://doi.org/10.1111/j.1151-2916.1995.tb08246.x.

(47) Chen, D.; Wang, J. H.; Chou, T. F.; Zhao, B.; El-Sayed, M. A.; Liu, M. Unraveling the Nature of Anomalously Fast Energy Storage in T-Nb2O5. *J. Am. Chem. Soc.* **2017**, *139* (20), 7071–7081. https://doi.org/10.1021/jacs.7b03141.

(48) Jiang, J.; Li, Y.; Liu, J.; Huang, X.; Yuan, C.; Lou, X. W. (David). Recent Advances in Metal Oxide-Based Electrode Architecture Design for Electrochemical Energy Storage. *Adv. Mater.* **2012**, *24* (38), 5166–5180. https://doi.org/10.1002/adma.201202146.

(49) Itou, Y.; Ogihara, N.; Kawauchi, S. Role of Conductive Carbon in Porous Li-Ion Battery Electrodes Revealed by Electrochemical Impedance Spectroscopy Using a Symmetric Cell. *J. Phys. Chem. C* **2020**, *124* (10), 5559–5564. https://doi.org/10.1021/acs.jpcc.9b11929.

(50) Allpress, J. G.; Roth, R. S. The Effect of Annealing on the Concentration of Wadsley Defects in the Nb_2O_5-WO_3 System. *J. Solid State Chem.* **1971**, *3* (2), 209–216. https://doi.org/10.1016/0022-4596(71)90030-2.

(51) Ok, K. M.; Halasyamani, P. S.; Casanova, D.; Llunell, M.; Alemany, P.; Alvarez, S. Distortions in Octahedrally Coordinated D0 Transition Metal Oxides: A Continuous Symmetry Measures Approach. *Chem. Mater.* **2006**, *18* (14), 3176–3183. https://doi.org/10.1021/cm0604817.

CHAPTER IV: INVESTIGATING THE ROLE MOLYBDENUM SUBSTITUTION PLAYS IN THE ELECTROCHEMICAL PERFORMANCE OF WADSLEY-ROTH NIOBIUM TUNGSTEN OXIDE ANODE MATERIALS[4]

4.1 Overview

Wadsley-Roth (W-R) crystallographic shear compounds are a promising class of materials to replace graphite for high-rate Li-ion battery applications. These materials have complex crystal structures and can include a wide range of elements from the periodic table. This complexity offers exciting opportunities but also poses significant challenges in understanding structure-property relationships. Simply changes such as transition metal substitution can significantly alter electrochemical properties. The difficulty in understanding the origin of these effects due to the many possible transition metal sites in the crystal structure is an important question to address. Systematic studies of these materials are challenging because transition metal cations can occupy different sites within the unit cell, and even small changes in site occupancy can greatly change electrochemical properties. In this work, we systematically investigate how transition metal doping influences capacity and cycle stability in a series of molybdenum substituted W-R compounds. $Mo_xNb_{14}W_{3-x}O_{44}$ compositions were synthesized via high temperature solid-state reactions before physically characterized and assembled into cells. Galvanostatic cycling revealed that discharge capacities increased with molybdenum concentration in $Mo_xNb_{14}W_{3-x}O_{44}$. One potential explanation of this capacity increase could be due to molybdenum being more prone to octahedral distortions, lowering the Li-ion binding energies in the material and allowing more lithium to

---

[4] Luke D. Salzer performed experiments, analyzed data, and wrote the manuscript. Claire Y. Gervais and Cami Christensen both performed experiments and analyzed data. Dani Lustig assisted with scanning electron microscopy measurements.

intercalate and further reduce the transition metals. While molybdenum substitution is shown to be a method to improve the capacities of W-R materials, the more molybdenum rich samples display larger capacity decays and higher irreversibility with additional cycling. This could be due to larger unit cell changes when the transition metal centers along the shear plane reorganize upon lithiation and delithiation, resulting in lithium trapping or particle fracture. Lastly, the slope of the charge-discharge curves increases with increasing molybdenum concentration, likely due to changes in the Li-ion binding sites and energies. This limits molybdenum rich compositions from delivering constant power at a fixed C-rate more than tungsten rich compounds. With these results in mind, we address design principles for next generation energy storage materials.

4.2 Introduction

Renewable energy generation in the United States is predicted to increase from 500,000 GWh in 2015 to 600,000 GWh in 2030, and with this energy generation, electric energy storage is also going to increase.[1] One class of materials of interest for next generation energy storage are Wadsley-Roth crystallographic shear compounds, which are a promising anode material to replace graphite for high-power battery applications. While Wadsley, Roth, and others established the structural principles of W-R crystallographic shear structures in the 1960s, researchers did not use a niobium tungsten oxide W-R structures in lab scale Li-ion batteries until 2018.[2–9] In this work, W-R materials possessed higher volumetric capacity and better rate capabilities when compared to commercial level graphite anodes.[10] Additionally, W-R materials operate outside the potential window where lithium dendrites form, making them safer alternative anodes for energy storage applications.[11,12]

The structural motif shared by all W-R crystallographic shear compounds is the $n \times m$ blocks of edge-sharing octahedra. Corner-sharing octahedra occupy the block center, with blocks extending indefinitely perpendicular to the block plane.[2] Additionally, tetrahedral sites can be present in the block corners to fill void spaces. These blocks can be a variety of sizes ranging from 3×3 to 5×5 as well as possessing mixed block sizes, such as H-Nb_2O_5 having alternating layers of 3×4 and 3×5.[11–17] Another feature of interest for niobium oxide based W-R compounds is they possess a large degree of compositional freedom, with doping being a common strategy to alter their electrochemical performance.[17–26] With this compositional freedom, there has been research to understand the structure of these materials, which often possess some degree of cation disorder that can affect the electrochemical performance. $Nb_{14}W_3O_{44}$, which has a 4×4 block structure with a tetrahedral site, possess Nb and W cation disorder in the block center, where computational and experimental work has been conducted to elucidate cation site preferences in the unit cell.[27,28] The role cation disorder has in the local environments and Li-ion binding energies in relation to the electrochemical performance of the material is still an open question that is challenging to address. Furthermore, elemental substitutions and doping has been shown to drastically change the electrochemical performance of W-R materials, as shown in work conducted by Cheng et al. In this work, they synthesized $V_{0.28}Nb_{13.72}W_3O_{44}$ and $Nb_{14}W_3O_{44}$ and found that they stored approximately 300 and 250 mAh/g when charged and discharge at 1C respectively, and that the V substituted samples continues to outperform $Nb_{14}W_3O_{44}$ at a variety of (dis)charging rates. These significant changes in electrochemical performance with a slight elemental substitution highlights how important understanding structure property relationships is for next-generation energy storage materials.

An important question in W-R niobium oxide anode materials is how elemental substitution influences the battery performance. Recent computations reveal a unique redox mechanism upon Li-ion intercalation in $Li_xTiNb_2O_7$, another W-R phase, that results in the formation of metal−metal bonds between Nb octahedra along the shear plane.[29] These metal-metal bonds impact the structure by shortening cation distances, subsequently changing the lattice parameters of the unit cell and impacts Li-ion site preferences.[22,30] One question is how do the orbitals involved in metal-metal bonding affect the potential charge is stored in the electrode? Additionally, changing transition metals in the unit cell will affect the mechanical stability of the compounds, especially with additional cycling. Lastly, the role octahedral distortions play on the electrochemical performance and structural stability of the substituted compounds on repeated cycling is still an open question. In this work, we chose to study Mo substitution for W because metal-metal bonding has been reported in molybdenum oxides, such as $LiScMo_3O_8$, and because Mo exhibits the larger degree of distortions when compared to W.[31–33]

Koçer et al. conducted density functional theory calculations to understand the structural principles that contribute to the high-power applications W-R materials possess.[30] Their work showed lattice expansion/contraction during cycling, which lowers the volume expansion of the material. Koçer et al. also hypothesized that the impressive capacity originates from the variety of low energy lithium storage sites with different local environments.[34] Researchers have attributed the high-rate capabilities of these materials to their open tunnel-like structure, which facilitates fast lithium-ion transport with low activation energy.[13,34] Recent work examined how the number of tunnels in the unit cell influence the performance of three structurally similar Nb-W-O Wadsley-Roth materials: 3×4 $Nb_{12}WO_{33}$, 4×4 $Nb_{14}W_3O_{44}$, and 4×5 $Nb_{16}W_5O_{55}$.[13] The findings revealed that increasing the block size results in higher diffusion coefficients, supporting the literature hypothesis that Li-ion diffusivity increases with block size.[17,30,34] This research demonstrated that the symmetric 4×4 $Nb_{14}W_3O_{44}$ possesses higher capacity and reversibility than the asymmetric

3×4 $Nb_{12}WO_{33}$ and 4×5 $Nb_{16}W_5O_{55}$, indicating that block structure significantly influences the electrochemical performance of W-R compounds.

In this work, we aim to better understand how elemental substitutions affect the electrochemical performance of W-R crystallographic shear compounds. To answer this question, here we systematically synthesized $Mo_xNb_{14}W_{3-x}O_{44}$ via high temperature solid-state reactions. Following materials synthesis and characterization, electrochemical cells were fabricated and tested to assess for differences in performance for each $Mo_xNb_{14}W_{3-x}O_{44}$ compound.

4.3 Experimental

4.3.1 Synthesis of W-R Compounds

The samples were synthesized via high temperature solid state synthesis reactions following previous literature.[13,35] Stoichiometric ratios of black NbO_2 (Alfa Aesar, 99%), dark blue $WO_{2.9}$ (Alfa Aesar, 99%), and teal MoO_3 (Alfa Aesar, 99%) powders were ground in an agate mortar and pestle to create the precursors for $Nb_{14}W_3O_{44}$, $MoNb_{14}W_2O_{44}$, $Mo_2Nb_{14}WO_{44}$, and $Mo_3Nb_{14}O_{44}$. For example, 0.283g of NbO_2, 0.0757g of $WO_{2.9}$ and 0.0236g of MoO_3 were required to synthesize $MoNb_{14}W_2O_{44}$. The combined powders were pressed into pellets using a hydraulic press (Caver Model: 4350.L) at 2 tons of pressure. The pellets were placed in an alumina crucible and platinum boat and heated, open to air, in a Thermo Scientific Lindberg Blue M tube furnace. $Nb_{14}W_3O_{44}$ was heated from 25°C for 10 hours to 1200°C, held for 4 hours and cooled to 25°C in 10 hours. $MoNb_{14}W_2O_{44}$ was heated at a rate of rate of 10°C min^{-1} to 900°C, with a hold time of 4 hours, and cooled naturally to 25°C. $Mo_2Nb_{14}WO_{44}$ was heated at a rate of 10°C min^{-1}, to 800°C, with a hold time of 6 hours, and cooled naturally to 25°C. $Mo_3Nb_{14}O_{44}$ was heated to 700°C at a rate of 10°C min^{-1}, with a hold time of 4 hours, and cooled naturally to 25°C.

4.3.2 Sample Characterization

The metal oxide powders were suspended in ethanol and drop-casted onto a Si B-doped zero diffraction slide. The samples were characterized by powder X-ray diffraction (XRD) using a Bruker D8 Discover DaVinci-Powder Diffractometer (Cu Kα radiation). Rietveld refinement was performed using Bruker's Diffrac.Topas software using CIF files from Inorganic Crystal Structure Database (ICSD), generated by JP-Minerals VESTA software. Scanning electron microscopy (SEM) analyses were performed on a JEOL 6500 field emission SEM. Raman spectroscopy was performed on an Olympus IX-73 optical microscope with a 532 nm Ondax THz- laser source. A 20X Na0.95 air objective (Olympus PlanFL N20X) was used to focus incident light on the sample, which was simply prepared by placing sample powder on a glass microscope slide. Scattered light passed through a Horiba iHR550 imaging spectrometer (1800 gr/mm) and was detected on a Synapse back-illuminated deep depletion charge-coupled device (CCD). The system was calibrated using the Stokes and anti-Stokes shift of a Si wafer, occurring at 521 and -521 cm^{-1}, respectively. A general spectrum was obtained between 200 and 1100 cm^{-1} in accordance with literature parameters. Additional spectra were taken in ranges from 575 to 725 cm^{-1}, and 850 to 1050 cm^{-1} to better investigate peaks of interest.

Simulated diffraction patterns we visualized through VESTA, utilizing a crystallographic information file (CIF) of $Nb_{14}W_3O_{44}$, with a I-4 space group, downloaded from the Inorganic Crystal Structure Database (ICSD coll. Code 23801). The CIF from the ICSD was changed from the I-4 space group to I4/m when conducting the Rietveld refinement for each composition, with the overall occupancy of the tetrahedral changed from 1 to 0.5 due to this unit cell change, allowing for the possibility for a tetrahedral site at [1.00 0.5 0.75] and [1.00 0.5 0.25].

4.3.3 Half-cell construction

Half-cell batteries were constructed in an argon glove box using the following components: stainless steel cases (MTI Corp, CR2032), a stainless-steel wave spring (MTI Corp, CR20WS), a stainless-steel spacer (MTI Corp, CR20-Spacer-05), and a glass microfiber (VWR, 691) separator were used. The metal oxide composite electrode was prepared by grinding an 8:1:1 ratio of W-R particles, conductive carbon (Super P, Alfa Aesar), and polyvinylidene fluoride binder (PVDF, Sigma Aldrich) in an agate mortar and pestle. The metal oxide composite electrode is the cathode and lithium metal is the anode in this half-cell geometry. This mixture was dispersed in N-methyl pyrrolidone (NMP, Sigma-Aldrich) until the solution was slightly viscous. The slurry was doctor-bladed onto a copper substrate to cast a 100 μm-thick film. The film was dried overnight in vacuum at approximately 150°C. The dried film was punched into several ½ inch electrodes and transferred into an argon glove box. Coin cells were constructed with the MTI coin cell case using a ½ inch diameter lithium metal electrode, and a 5/8th inch diameter separator was laid on top. 80.0 μL of electrolyte containing 1M $LiPF_6$ dissolved in a 1:1 volume ratio of ethylene carbonate/dimethyl carbonate (EC/DMC, Sigma Aldrich) was pipetted onto the separator. The cathode was placed on the separator after it had become saturated with electrolyte, followed by the stainless-steel spacer, spring, and finally the end cap. The cells were pressed with 0.9 tons of pressure using a compact digital pressure controlled electric crimper (MTI MSK-160E). The cells rested for 12 hours before electrochemical measurements were performed to allow the electrolyte to fully saturate the separator.

4.3.4 Electrochemical Testing

The coin cells were cycled on an Arbin battery tester (LBT-20084) at a C-rate of C/3, in which C-rate is the current which a battery is discharged relative to its theoretical capacity. The theoretical capacity is calculated by, $Q_{theoretical} = nF/3.6M$, where n is the number of electrons transferred per formula unit, F is Faraday's constant, 3.6 is a conversion factor between coulombs and mAh/g, and M is the molecular weight. The C-rate was calculated according to following equation: $I = (Q_{theoretical} \times m)/t,$ where I is the current applied, m is the mass of active material, and t is time in hours. In this study, some of the data from the galvanostatic cycling is from multiple cells, with n= 5-, 6-, 5-, and 7-coin cells for $Nb_{14}W_3O_{44}$, $MoNb_{14}W_2O_{44}$, $Mo_2Nb_{14}WO_{44}$, and $Mo_3Nb_{14}O_{44}$ respectively.

4.4 Results

In this work, we investigated how substituted molybdenum for tungsten influences the electrochemical performance of $Mo_xNb_{14}W_{3-x}O_{44}$ synthesized via high-temperature solid-state reactions. Prior work conducted by Koçer et al. suggests that the strength of the second order Jahn-Teller (SOJT) distortion may play a role in the charge storage capabilities of mixed transitional metal W-R crystallographic shear compounds.[27,32]

In a typical reaction, stoichiometric ratios of NbO_2, $WO_{2.9}$, and MoO_3 were mixed in an agate mortar and pestle, pressed into a pellet, and heated to a setpoint temperature (see Experimental Methods for details). Each composition was synthesized at different temperatures to minimize phase impurities such as $Nb_{12}WO_{33}$.[13,36] Figure 4.1 shows the background subtracted PXRD data for each composition, and a simulated pattern generated through VESTA, with the crystallographic information file (CIF) from the Inorganic Crystal Structure Database (ICSD), collection code 23801 and the I4/m space group. All peaks from the simulated diffraction patterns are present in the experimental patterns, indicating each synthesized sample is the correct crystallographic phase. Additionally, Rietveld refinement was conducted on each composition, using the same CIF, to elucidate possible phase impurities. Each composition was greater than 90% phase pure, with $MoNb_{14}W_2O_{44}$ and $Mo_2Nb_{14}WO_{44}$ possessing slight impurities shown by the shoulder present on the peak 25.32° and the small peak at 17.56° 2θ. This phase impurity was indexed to be $Nb_{12}WO_{33}$ or $H\text{-}Nb_2O_5$, which can also be synthesized in the same temperature regime.[13,14,16,36,37] We note that characterizing these materials is challenging through PXRD and Rietveld refinement due to the possibility of transition metals occupying different sites and the similarity of atomic scattering factor between niobium and molybdenum.[28,38] Additionally, $H\text{-}Nb_2O_5$, $Nb_{12}WO_{33}$, or $Nb_{16}W_5O_{55}$ can form under these reaction conditions, further adding to the challenge of characterizing these materials.[13,14,19]

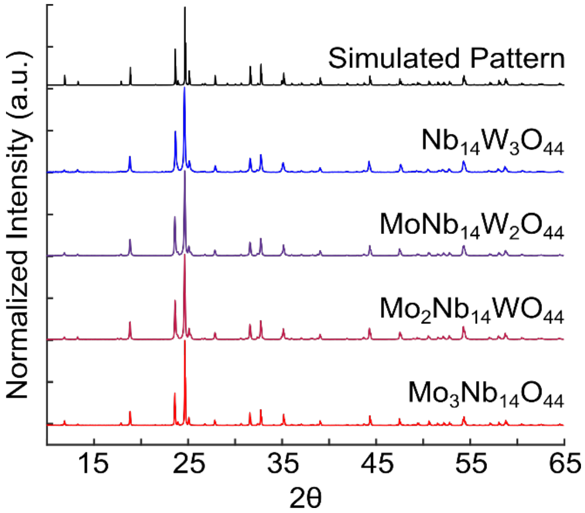

Figure 4.1. PXRD patterns of $Mo_xNb_{14}W_{3-x}O_{44}$ compounds. The simulated $Nb_{14}W_3O_{44}$ pattern was calculated in VESTA using a crystallographic information file (CIF collection code 23801 and the I-4 space group) from the Inorganic Crystal Structure Database (ICSD)

Following PXRD, Raman spectroscopy was conducted to illicit more structural information based on differences in the binding environments between compositions. Figure 4.2a. shows a survey Raman spectra from 200 to 1050 cm^{-1}. When comparing the Raman spectra for

$Mo_xNb_{14}W_{3-x}O_{44}$ shown in the low wavenumber region (200-450 cm^{-1}) $Nb_{14}W_3O_{44}$ and $MoNb_{14}W_2O_{44}$ both possess a shoulder and intense peak at approximately 240 and 260 cm^{-1} respectively. The more molybdenum rich compositions possess broader peaks, with $Mo_2Nb_{14}WO_{44}$ displaying a similar shoulder at 240 cm^{-1}, a main peak at 260 cm^{-1}, and a shoulder at 305 cm^{-1}. $Mo_3Nb_{14}O_{44}$ is very similar to $Mo_2Nb_{14}WO_{44}$, however the shoulder at 305 cm^{-1} continues to increase in intensity and becomes a clear peak. This systematic increase in intensity with molybdenum concentration may be due to vibrational modes of molybdenum occupying block center or tetrahedral sites and will be discussed in the Discussion section. Comparing the spectra from 450-875 cm^{-1}, each composition displays peak at approximately 480 cm^{-1}. Additionally, each composition shows a clear peak at approximately 635 cm^{-1}, and a shoulder at approximately 750 cm^{-1} which is more intense and broadens as the molybdenum ratio increases. Lastly, Figure 4.2b. displays systematic changes with molybdenum introduction. Each composition possesses a peak at 900 cm^{-1} and approximately 970 cm^{-1} though higher molybdenum concentrations result in a slight red shift. Furthermore, $Nb_{14}W_3O_{44}$ displays a shoulder at 970 cm^{-1}, whereas the molybdenum substituted compositions possess a shoulder at 930 cm^{-1}. Previous work on a related W-R crystallographic shear compound, $Nb_{12}WO_{33}$, assigns this vibrational mode to tungsten occupying the tetrahedral site and molybdenum occupying the tetrahedral site respectively. Due to the shoulder being present at 930 cm^{-1} for $MoNb_{14}W_2O_{44}$, $Mo_2Nb_{14}WO_{44}$, and $Mo_3Nb_{14}O_{44}$ indicates a preference for Mo over W occupying the tetrahedral site.

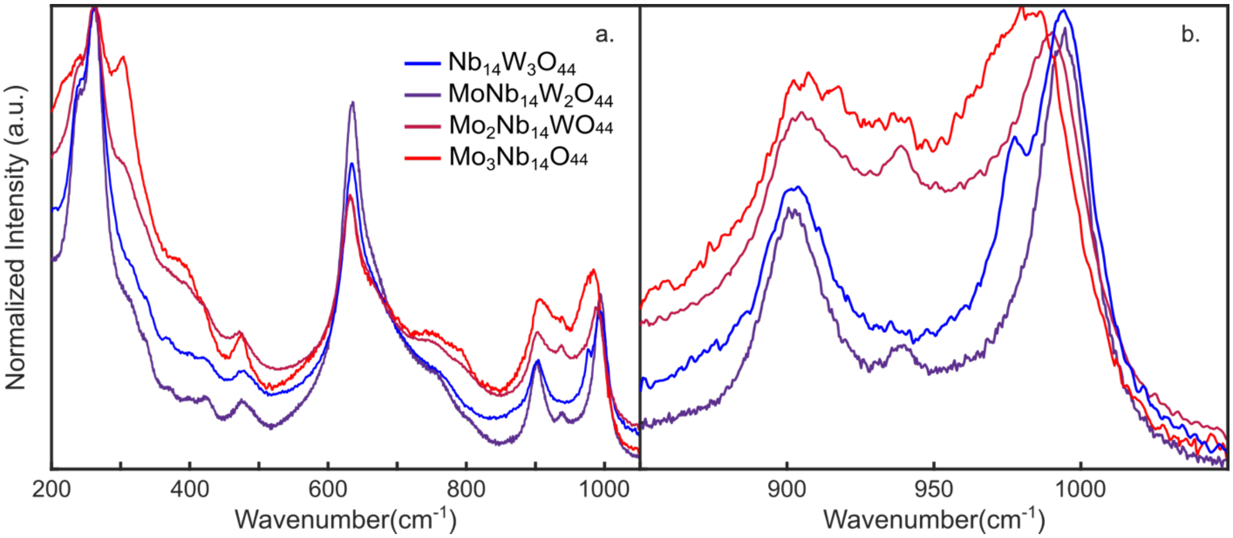

Figure 4.2. (a) Survey Raman spectra comparison of $Mo_xNb_{14}W_{3-x}O_{44}$ and (b) comparison of a focused region for $Mo_xNb_{14}W_{3-x}O_{44}$

The last physical characterization technique conducted was scanning electron microscopy (SEM) to evaluate the particle structure and size. SEM analysis, shown Figure 4.3, shows particles with no clear morphology for each composition and that the particles tend to agglomerate following the precursors being pressed into pellets and heated. Furthermore, particle sizes were analyzed and shown in Figure A3.1, with the largest average being $Nb_{14}W_3O_{44}$ (2.92 µm), then $Mo_3Nb_{14}O_{44}$ (2.02 µm), $MoNb_{14}W_2O_{44}$ (0.883 µm), and $Mo_2Nb_{14}WO_{44}$ (0.624 µm) is the smallest.

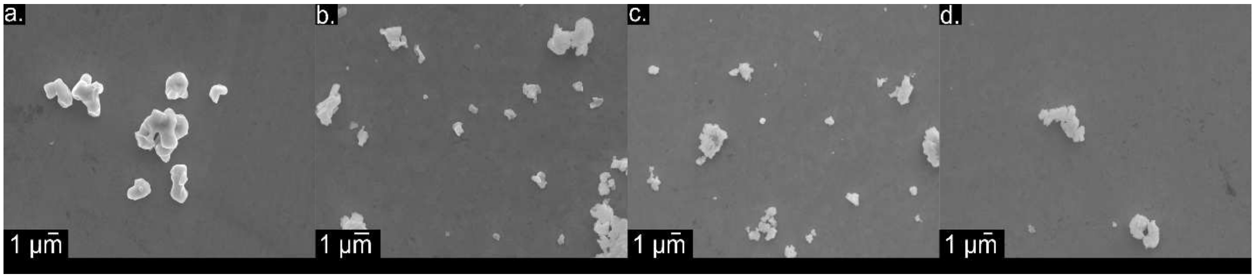

Figure 4.3. SEM images of (a) $Nb_{14}W_3O_{44}$, (b) $MoNb_{14}W_2O_{44}$, (c) $Mo_2Nb_{14}WO_{44}$, and (d) $Mo_3Nb_{14}O_{44}$

Having characterized the structure of the $Mo_xNb_{14}W_{3-x}O_{44}$ compounds, we investigated their electrochemical behavior and performance as Li-ion insertion hosts. The electrochemical performance was investigated by fabricating coin cells based off of established methods in an 8:1:1 ratio of active material, conductive carbon, and PVDF binder.[17] These additives where utilized to help minimize the *iR* loss due to the poorly conductive metal oxide particles and aid in the mechanical stability and electrical contact upon cycling, the ratio was not optimized for battery performance.[35,39,40] Each electrochemical cell underwent galvanostatic cycling at a C-rate of C/3 to allow time for the (dis)charge storage processes to occur and to further minimize the *iR* loss effects.

Figure 4.4a-d. shows the (dis)charge curves for $Nb_{14}W_3O_{44}$, $MoNb_{14}W_2O_{44}$, $Mo_2Nb_{14}WO_{44}$, and $Mo_3Nb_{14}O_{44}$ respectively. Each of these compositions display similarly sloped voltage profiles upon lithiation/delithiation. On the initial lithiation, the voltage quickly decreases from 3V to approximately 2.2 V vs Li/Li^+ before charge is stored. $Nb_{14}W_3O_{44}$ displays a plateau from 1.75 V to 1.5 V before the profile decays again down to 1 V, storing the lowest specific capacity of 221mAh/g. With the addition of molybdenum, the profiles become significantly more sloped, with slight inflection points throughout the lithiation process before the voltage decreases to 1 V. $Mo_2Nb_{14}WO_{44}$ and $MoNb_{14}W_2O_{44}$ store approximately 263mAh/g, and $Mo_3Nb_{14}O_{44}$ stores approximately 306mAh/g. This enhanced sloping profile feature observed as a function of molybdenum concentration is problematic for Li-ion battery applications because a continuously decreasing voltage results in continuous battery power loss during discharge.

Each material fails to reach the initial discharge capacity with $Nb_{14}W_3O_{44}$, $MoNb_{14}W_2O_{44}$, $Mo_2Nb_{14}WO_{44}$, and $Mo_3Nb_{14}O_{44}$ with the subsequent charging step. On cycle 2, each material exhibits some capacity loss, with $Nb_{14}W_3O_{44}$, $MoNb_{14}W_2O_{44}$, $Mo_2Nb_{14}WO_{44}$, and $Mo_3Nb_{14}O_{44}$ storing 199, 232, 227, and 285 mAh/g respectively. Upon continued cycling, each material displays a monotonic capacity loss, with $Mo_3Nb_{14}O_{44}$ displaying the largest change in charge stored, losing 116 mAh/g (38%) between cycle 1 and 20, shown in Figure 4.4. The capacity loss rate generally increases with x (Figure A3.2), potentially due to structural changes related to distorted Mo octahedra. Figure 4.5 illustrates the effect molybdenum substitution has on the discharge capacity, with an increase in capacity observed on average with increasing molybdenum. Additionally, the capacity loss is clearly seen to be greater for the molybdenum rich compositions, explanations for both the increase in capacity and capacity loss will be addressed in the Discussion section. Figure A3.3a,b shows after approximately 4 cycles the average coulombic efficiency and relative capacity loss for each $Mo_xNb_{14}W_{3-x}O_{44}$ composition begins for plateau, with the tungsten rich compositions possessing slightly higher coulombic efficiencies, highlighting the intrinsic reversibility of these unoptimized materials.

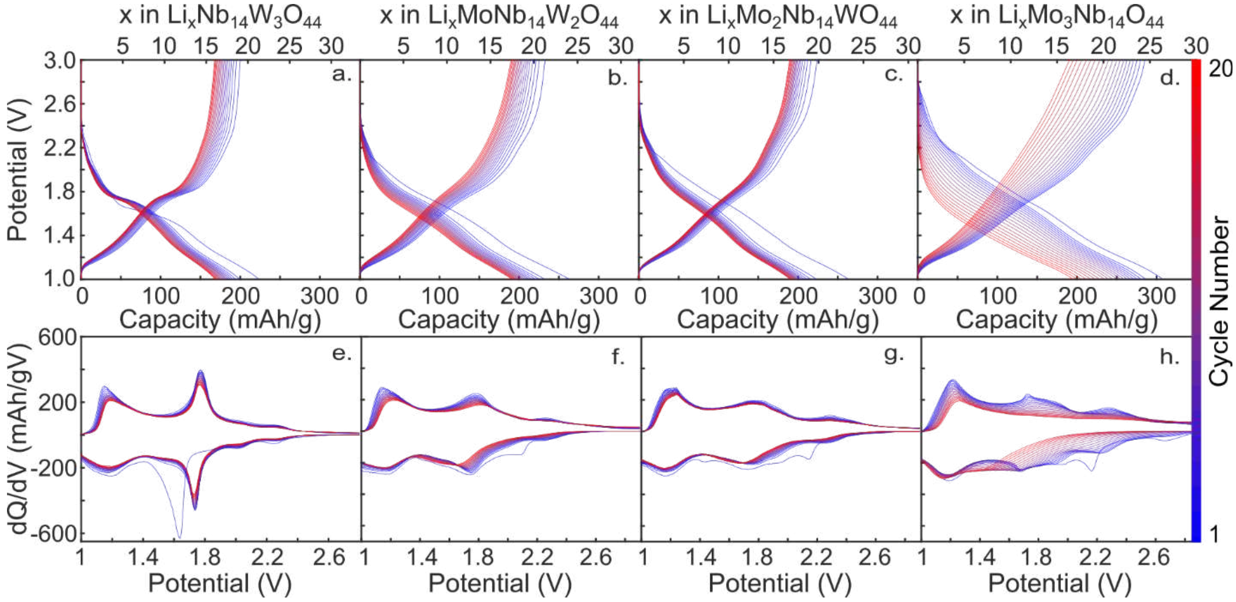

Figure 4.4. Charge/discharge curves at a C-rate of C/3 for (a) $Nb_{14}W_3O_{44}$, (b) $MoNb_{14}W_2O_{44}$, (c) $Mo_2Nb_{14}WO_{44}$, and (d) $Mo_3Nb_{14}O_{44}$. d*Q*/d*V* plots for (e) $Nb_{14}W_3O_{44}$, (f) $MoNb_{14}W_2O_{44}$, (g) $Mo_2Nb_{14}WO_{44}$, and (h) $Mo_3Nb_{14}O_{44}$.

Next, we analyzed the differential capacity (d*Q*/d*V*) plots to assess how molybdenum concentration affects the ion insertion processes. Figure 4.4e-h displays the d*Q*/d*V* plots for $Nb_{14}W_3O_{44}$, $MoNb_{14}W_2O_{44}$, $Mo_2Nb_{14}WO_{44}$, and $Mo_3Nb_{14}O_{44}$ respectively. We discuss the positive potential region (2V-3V vs. Li/Li^+) for cycle one first. $Nb_{14}W_3O_{44}$ has two peaks in this Region, with the peak at 2.24V being slightly more intense than the peak at 2.01V. $MoNb_{14}W_2O_{44}$ is similar, with a peak at 2.27V and a more intense feature at 2.10V. Both $Mo_2Nb_{14}WO_{44}$ and $Mo_3Nb_{14}O_{44}$

display similar features, with $Mo_2Nb_{14}WO_{44}$ displaying an inflection point at approximately 2.65V, while $Mo_3Nb_{14}O_{44}$ shows a clear peak feature. Additionally, both these compounds show a peak at approximately 2.20 V that becomes sharper with increased molybdenum concentration. Upon continued lithiation, $Nb_{14}W_3O_{44}$ and $MoNb_{14}W_2O_{44}$ possesses a single, intense peak in the mid potential region (1.4V-2.0V vs. Li/Li^+). As the molybdenum concentration increases, the intensity of this peak decreases dramatically, and slight inflection points appear and become more pronounced for both $Mo_2Nb_{14}WO_{44}$ and $Mo_3Nb_{14}O_{44}$. Lastly, in the low potential region (1.0. V-1.4V vs. Li/Li^+), each material displays a single, broad peak.

On the charge step $Nb_{14}W_3O_{44}$ possesses 2 prominent peaks, one in both the low potential region at 1.17 V and mid potential region at 1.79 V, and some slight inflection points in the high potential region. With increasing molybdenum ratio, the peaks in the low potential region look similar, and the peak in the mid potential region becomes less intense and broader. Additionally, $Mo_3Nb_{14}O_{44}$ possesses a small peak at approximately 1.789V and a shoulder from approximately 1.8V-2.0V in the mid potential region. Lastly, the small inflection points shown in $Nb_{14}W_3O_{44}$ in the high potential region increase in intensity as molybdenum concentration increases, with both $Mo_2Nb_{14}WO_{44}$ and $Mo_3Nb_{14}O_{44}$ displaying clear peaks at approximately 2.35V.

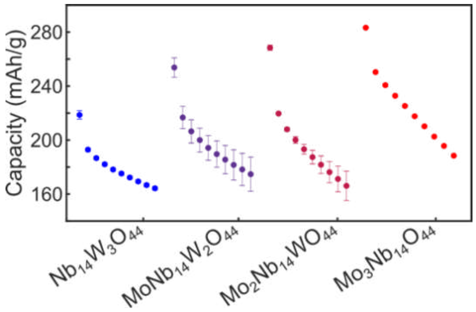

Figure 4.5. Discharge capacity versus cycle number (displaying odd cycles only for clarity) for $Mo_xNb_{14}W_{3-x}O_{44}$. The data points represent average values, and the error bars represent the standard error of the mean.

With repeated cycling, there are clear changes in the d*Q*/d*V* plots for each composition. The intense peak in the mid potential region for $Nb_{14}W_3O_{44}$ shifts from approximately 1.62V to 1.77V and becomes less intense from cycle one to two, but subsequent cycling appears to be the most reversible out of all compositions, with some loss in intensity from cycles 2-20 for $Nb_{14}W_3O_{44}$. For both $MoNb_{14}W_2O_{44}$ and $Mo_2Nb_{14}WO_{44}$, the dQ/dV plots lose intensity upon repeated cycling, specifically in the high potential region, and shows some irreversibility with additional cycling. Lastly, $Mo_3Nb_{14}O_{44}$ displays the greatest differences between cycle 1 and subsequent cycling, losing the peak 2.65V, and a peak at approximately 2.20V shifts to more positive potentials while becoming less intense. Furthermore, both the high and mid potential features completely disappear after several cycles, with the only feature remaining on cycle 20's discharge being the broad peak in the low potential region. This dramatic change in the dQ/dV, as well as the changes in the constant current plots, highlight the cycle irreversibility that is correlated molybdenum concentration. Possible explanations for the changes in dQ/dV plots will be addressed in the Discussion section.

4.5 Discussion

Here we discuss possible explanations for our key results: (1) Mo substitution for W in $Mo_xNb_{14}W_{3-x}O_{44}$ compounds enables multi-electron redox; (2) Mo substitution increases capacity fade.

First, we discuss potential explanations for why molybdenum substitution for W increases the discharge capacity beyond the theoretical maximum capacity for 1 electron per transition metal. One hypothesis is that Mo atoms present in the unit cell alter the local Li-ion binding environments and therefore lowers the Li-ion binding energies. A literature survey conducted by Ok et al. discovered that Mo is much more prone to octahedral distortions when compared to both Nb and W.[32] This higher degree of distortions present in the block center and block edge could create local storage sites with lower Li-Ion binding energies, leading to higher capacities.[27,41,42] The distortions responsible for improved capacity may also lead to cycle irreversibility. During lithiation, the distorted Mo octahedra will become less off-centered as the molybdenum is reduced from Mo^{6+} to Mo^{5+}.[29,30] We hypothesize that the structural stability depends on the ability of Mo octahedral to shift from distorted and non-distorted arrangements during lithiation and delithiation. Previous experimental and computational work conducted on the structurally similar W-R compound, $Nb_{12}WO_{33}$ hypothesizes that the shoulder features present in the Raman spectroscopy data shown in Figure 4.2b is due in part to W occupying the tetrahedral site for $Nb_{14}W_3O_{44}$ or Mo for the molybdenum substituted samples, indicating that the higher oxidation state transition metals are occupying the tetrahedral site. This indicates that the tetrahedral sites play an important role in the charge and lithium storage mechanisms in W-R shear structures and warrants future investigations. Other interesting research directions arise to test that the role distortions play in the long term cycling stability of W-R crystallographic shear compounds, such as synthesizing W-R materials with weak distorters, such as Zr, and to conduct in-situ measurements to analyze the degree of distortions during lithiation.[30,32]

Another explanation for the enhanced capacity as molybdenum concentration increases in $Mo_xNb_{14}W_{3-x}O_{44}$ could be due to differences in electronegativity between Mo and W that improve the electronic conductivity earlier in the cycling.[43] Experimentally, we observe features present in the dQ/dV plots in the high potential regions (>2.0 V vs. Li/Li^+ in Figure 4.4e-h) for each W-R compound. In this region, we see that the first peak present shifts to more positive potentials with increasing Mo concentration. This could be due to Mo being more electronegative than Nb and W, resulting in lower energy electronic states.[44] These lower energy states would alter the density of states (DOS), resulting in differences in the band gap or isolated states present in the band gap that will be filled at more positive potentials for reduction.[22,29,30]

Another possible explanation for the enhanced capacity in molybdenum substituted W-R compounds is metal-metal bonding. Saber et al. conducted computations as a function of lithiation in another W-R compound, $TiNb_2O_7$.[29] In this work, they discovered that metal-metal bonding can occur at low levels of lithiation between d_{xy} orbitals of the edge shared octahedra along the shear plane, forming bonding and anti-bonding orbitals. This phenomena can occur in other W-R compounds, such as PNb_9O_{26} and VNb_9O_{26}, where lithiation induces Nb-Nb orbital overlap.[22] From the electronic structure calculations, metal-metal bonding results in electronic states below the Fermi level. Moreover, neutron diffraction reveals that the experimental tungsten site occupancy of $Nb_{14}W_3O_{44}$ differs from computationally predicted, allowing for tungsten occupying edge sites.[28] This trend most likely extends to molybdenum as well, given the similar ionic and crystal radii, as well as the same oxidation state. Experimentally, we observe features present in the dQ/dV plots in the high potential regions (>2.0 V vs. Li/Li^+ in Figure 4.4e-h) for each W-R compound. Furthermore, these is a large gap between the features present in the high and mid potential regions that could represent the localized state in the band gap and the conduction band predicted by Saber et al. Occupying these states with electrons may be favorable, but removing electrons from these states is not because we do not observe a corresponding positive dQ/dV peak feature at positive potentials when oxidizing the samples. The irreversible cycling suggests that metal-metal bonds induce permanent structural rearrangements that prevent fully oxidizing the material, limiting discharge capacities.

4.6 Conclusion

In this work, we synthesized a series of molybdenum substituted Nb-W-O compounds to better understand how elemental composition influences the electrochemical performance for high-rate energy storage applications. The discharge capacity increases with increased molybdenum concentrations in $Mo_xNb_{14}W_{3-x}O_{44}$, suggesting that molybdenum substitution is a promising method to improve discharge capacities in Nb-W-O shear compounds. While increasing molybdenum concentration improves charge stored, it also results in irreversible cycling, with the more molybdenum rich compounds possessing larger capacity decays. This irreversibly may be due to a several factors, such as Mo substitution lowering Li-ion binding energies throughout the unit cell and structural rearrangements during lithiation/delithiation that result in lithium trapping. This is shown in the charge/discharge plots for each composition, which become significantly more sloped with increasing molybdenum, limiting the ability to deliver constant power in energy storage systems. Another possible explanation for the capacity loss could be due to metal-metal bonds forming, resulting in lower energy orbitals that populate with electrons when cycling. Molybdenum has a lower principal quantum number than W and is more electronegative, which results in lower energy orbitals when metal-metal bonding occurs. Lower energy orbitals result in increasing the potential in which charge is stored and the active material is reduced and by increasing the potential of the reduction event, the potential in which oxidation occurs is also increased. The structure-property relationships reported here should extend to other W-R materials and guide the development of future W-R compounds for energy storage applications.

4.7 References

(1) Aslani, A.; Wong, K.-F. V. Analysis of Renewable Energy Development to Power Generation in the United States. *Renew. Energy* **2014**, *63*, 153–161. https://doi.org/10.1016/j.renene.2013.08.047.

(2) Roth, R. S.; Wadsley, A. D. Multiple Phase Formation in the Binary System Nb_2O_5–WO_3. I. Preparation and Identification of Phases. *Acta Crystallogr.* **1965**, *19* (1), 26–32. https://doi.org/10.1107/S0365110X65002712.

(3) Roth, R. S.; Wadsley, A. D. Multiple Phase Formation in the Binary System Nb_2O_5–WO_3. II. The Structure of the Monoclinic Phases $WNb_{12}O_{33}$ and $W_5Nb_{16}O_{55}$. *Acta Crystallogr.* **1965**, *19* (1), 32–38. https://doi.org/10.1107/S0365110X65002724.

(4) Roth, R. S.; Wadsley, A. D. Multiple Phase Formation in the Binary System Nb_2O_5–WO_3. III. The Structures of the Tetragonal Phases $W_3Nb_{14}O_{44}$ and $W_8Nb_{18}O_{69}$. *Acta Crystallogr.* **1965**, *19* (1), 38–42. https://doi.org/10.1107/S0365110X65002736.

(5) Roth, R. S.; Wadsley, A. D. Multiple Phase Formation in the Binary System Nb_2O_5–WO_3. IV. The Block Principle. *Acta Crystallogr.* **1965**, *19* (1), 42–47. https://doi.org/10.1107/S0365110X65002748.

(6) Andersson, S.; Mumme, W. G.; Wadsley, A. D. Multiple Phase Formation in the Binary System Nb_2O_5–WO_3. V. The Structure of $W_4Nb_{26}O_{77}$, an Ordered Intergrowth of the Adjoining Compounds $WNb_{12}O_{33}$ and $W_3Nb_{14}O_{44}$. *Acta Crystallogr.* **1966**, *21* (5), 802–808. https://doi.org/10.1107/S0365110X66003852.

(7) Allpress, J. G.; Sanders, J. V.; Wadsley, A. D. Multiple Phase Formation in the Binary System Nb_2O_5–WO_3. VI. Electron Microscopic Observation and Evaluation of Non-Periodic Shear Structures. *Acta Crystallogr. B* **1969**, *25* (6), 1156–1164. https://doi.org/10.1107/S0567740869003669.

(8) Allpress, J. G.; Wadsley, A. D. Multiple Phase Formation in the Binary System Nb_2O_5-WO_3 VII. Intergrowth of H-Nb_2O_5 and $WNb_{12}O_{33}$. *J. Solid State Chem.* **1969**, *1* (1), 28–38. https://doi.org/10.1016/0022-4596(69)90005-X.

(9) Roth, R. S.; Wadsley, A. D. Mixed Oxides of Titanium and Niobium: The Crystal Structure of $TiNb_{24}O_{62}$ (TiO_2-$12Nb_2O_5$). *Acta Crystallogr.* **1965**, *18* (4), 724–730. https://doi.org/10.1107/S0365110X65001664.

(10) Griffith, K. J.; Wiaderek, K. M.; Cibin, G.; Marbella, L. E.; Grey, C. P. Niobium Tungsten Oxides for High-Rate Lithium-Ion Energy Storage. *Nature* **2018**, *559* (7715), 556–563. https://doi.org/10.1038/s41586-018-0347-0.

(11) Ding, H.; Song, Z.; Zhang, H.; Zhang, H.; Li, X. Niobium-Based Oxide Anodes toward Fast and Safe Energy Storage: A Review. *Mater. Today Nano* **2020**, *11*, 100082. https://doi.org/10.1016/j.mtnano.2020.100082.

(12) Deng, Q.; Fu, Y.; Zhu, C.; Yu, Y. Niobium-Based Oxides Toward Advanced Electrochemical Energy Storage: Recent Advances and Challenges. *Small* **2019**, *15* (32), 1804884. https://doi.org/10.1002/smll.201804884.

(13) Salzer, L. D.; Diamond, B.; Nieto, K.; Evans, R. C.; Prieto, A. L.; Sambur, J. B. Structure–Property Relationships in High-Rate Anode Materials Based on Niobium Tungsten Oxide Shear Structures. *ACS Appl. Energy Mater.* **2023**, *6* (3), 1685–1691. https://doi.org/10.1021/acsaem.2c03573.

(14) Cava, R. J.; Batlogg, B.; Krajewski, J. J.; Poulsen, H. F.; Gammel, P.; Peck, W. F.; Rupp, L. W. Electrical and Magnetic Properties of $Nb_2O_{5-\delta}$ Crystallographic Shear Structures. *Phys. Rev. B* **1991**, *44* (13), 6973–6981. https://doi.org/10.1103/PhysRevB.44.6973.

(15) Takami, N.; Ise, K.; Harada, Y.; Iwasaki, T.; Kishi, T.; Hoshina, K. High-Energy, Fast-Charging, Long-Life Lithium-Ion Batteries Using $TiNb_2O_7$ Anodes for Automotive Applications. *J. Power Sources* **2018**, *396*, 429–436. https://doi.org/10.1016/j.jpowsour.2018.06.059.

(16) Griffith, K. J.; Forse, A. C.; Griffin, J. M.; Grey, C. P. High-Rate Intercalation without Nanostructuring in Metastable Nb_2O_5 Bronze Phases. *J. Am. Chem. Soc.* **2016**, *138* (28), 8888–8899. https://doi.org/10.1021/jacs.6b04345.

(17) Griffith, K. J.; Grey, C. P. Superionic Lithium Intercalation through 2×2 nm^2 Columns in the Crystallographic Shear Phase $Nb_{18}W_8O_{69}$. *Chem. Mater.* **2020**, *32* (9), 3860–3868. https://doi.org/10.1021/acs.chemmater.9b05403.

(18) Griffith, K. J.; Wiaderek, K. M.; Cibin, G.; Marbella, L. E.; Grey, C. P. Niobium Tungsten Oxides for High-Rate Lithium-Ion Energy Storage. *Nature* **2018**, *559* (7715), 556–563. https://doi.org/10.1038/s41586-018-0347-0.

(19) Griffith, K. J.; Forse, A. C.; Griffin, J. M.; Grey, C. P. High-Rate Intercalation without Nanostructuring in Metastable Nb_2O_5 Bronze Phases. *J. Am. Chem. Soc.* **2016**, *138* (28), 8888–8899. https://doi.org/10.1021/jacs.6b04345.

(20) Griffith, K. J.; Seymour, I. D.; Hope, M. A.; Butala, M. M.; Lamontagne, L. K.; Preefer, M. B.; Koçer, C. P.; Henkelman, G.; Morris, A. J.; Cliffe, M. J.; Dutton, S. E.; Grey, C. P. Ionic and Electronic Conduction in $TiNb_2O_7$. *J. Am. Chem. Soc.* **2019**, *141* (42), 16706–16725. https://doi.org/10.1021/jacs.9b06669.

(21) Griffith, K. J.; Senyshyn, A.; Grey, C. P. Structural Stability from Crystallographic Shear in TiO_2-Nb_2O_5 Phases: Cation Ordering and Lithiation Behavior of $TiNb_{24}O_{62}$. *Inorg. Chem.* **2017**, *56* (7), 4002–4010. https://doi.org/10.1021/acs.inorgchem.6b03154.

(22) Preefer, M. B.; Saber, M.; Wei, Q.; Bashian, N. H.; Bocarsly, J. D.; Zhang, W.; Lee, G.; Milam-guerrero, J.; Howard, E. S.; Vincent, R. C.; Melot, B. C.; Ven, A. V. D.; Seshadri, R.; Dunn, B. S. Multielectron Redox and Insulator-to-Metal Transition upon Lithium Insertion in the Fast-Charging, Wadsley-Roth Phase PNb_9O_{25}. **2020**. https://doi.org/10.1021/acs.chemmater.0c00560.

(23) Cheng, Q.; Chen, J.; Zhao, J.; Li, F. A V-Doped $W_3Nb_{14}O_{44}$ Anode in a Wadsley–Roth Structure for Ultra-Fast Lithium-Ion Half/Full Batteries. *New J. Chem.* **2023**, *47* (42), 19537–19545. https://doi.org/10.1039/D3NJ03462C.

(24) Liu, H.; Chen, C. Wadsley–Roth Phase $CoNb_{11}O_{29}$ as a High-Performance Anode for Lithium-Ion Batteries. *J. Mater. Chem. A* **2024**, *12* (9), 5414–5421. https://doi.org/10.1039/D3TA07865E.

(25) Yang, C.; Yu, S.; Ma, Y.; Lin, C.; Xu, Z.; Zhao, H.; Wu, S.; Zheng, P.; Zhu, Z. Z.; Li, J.; Wang, N. Cr^{3+} and Nb^{5+} Co-Doped $Ti_2Nb_{10}O_{29}$ Materials for High-Performance Lithium-Ion Storage. *J. Power Sources* **2017**, *360*, 470–479. https://doi.org/10.1016/j.jpowsour.2017.06.026.

(26) Wyckoff, K. E.; Robertson, D. D.; Preefer, M. B.; Teicher, S. M. L.; Bienz, J.; Kautzsch, L.; Mates, T. E.; Cooley, J. A.; Tolbert, S. H.; Seshadri, R. High-Capacity Li^+ Storage through Multielectron Redox in the Fast-Charging Wadsley–Roth Phase $(W_{0.2}V_{0.8})_3O_7$. *Chem. Mater.* **2020**, *32* (21), 9415–9424. https://doi.org/10.1021/acs.chemmater.0c03496.

(27) Koçer, C. P.; Griffith, K. J.; Grey, C. P.; Morris, A. J. Cation Disorder and Lithium Insertion Mechanism of Wadsley–Roth Crystallographic Shear Phases from First Principles. *J. Am. Chem. Soc.* **2019**, *141* (38), 15121–15134. https://doi.org/10.1021/jacs.9b06316.

(28) Cheetham, A. K.; Allen, N.C. Cation Distribution in the Complex Oxide, $W_3Nb_{14}O_{44}$; a Time-of-Flight Neutron Diffraction Study. *J Chem Soc Commun* **1983**, 3.

(29) Saber, M.; Behara, S. S.; Van der Ven, A. Redox Mechanisms, Structural Changes, and Electrochemistry of the Wadsley–Roth $Li_xTiNb_2O_7$ Electrode Material. *Chem. Mater.* **2023**, *35* (22), 9657–9668. https://doi.org/10.1021/acs.chemmater.3c02003.

(30) Koçer, C. P.; Griffith, K. J.; Grey, C. P.; Morris, A. J. Cation Disorder and Lithium Insertion Mechanism of Wadsley-Roth Crystallographic Shear Phases from First Principles. *J. Am. Chem. Soc.* **2019**, *141* (38). https://doi.org/10.1021/jacs.9b06316.

(31) Burdett, J. K.; Hughbanks, T. Aspects of Metal-Metal Bonding in Early-Transition-Metal Dioxides. *Inorg. Chem.* **1985**, *24* (12), 1741–1750. https://doi.org/10.1021/ic00206a006.

(32) Ok, K. M.; Halasyamani, P. S.; Casanova, D.; Llunell, M.; Alemany, P.; Alvarez, S. Distortions in Octahedrally Coordinated d^0 Transition Metal Oxides: A Continuous Symmetry Measures Approach. *Chem. Mater.* **2006**, *18* (14), 3176–3183. https://doi.org/10.1021/cm0604817.

(33) Wyckoff, K. E.; Kaufman, J. L.; Baek, S. W.; Dolle, C.; Zak, J. J.; Bienz, J.; Kautzsch, L.; Vincent, R. C.; Zohar, A.; See, K. A.; Eggeler, Y. M.; Pilon, L.; Van der Ven, A.; Seshadri, R. Metal–Metal Bonding as an Electrode Design Principle in the Low-Strain Cluster Compound $LiScMo_3O_8$. *J. Am. Chem. Soc.* **2022**, *144* (13), 5841–5854. https://doi.org/10.1021/jacs.1c12070.

(34) Koçer, C. P.; Griffith, K. J.; Grey, C. P.; Morris, A. J. Lithium Diffusion in Niobium Tungsten Oxide Shear Structures. *Chem. Mater.* **2020**. https://doi.org/10.1021/acs.chemmater.0c00483.

(35) Li, R.; Liang, G.; Zhu, X.; Fu, Q.; Chen, Y.; Luo, L.; Lin, C. $Mo_3Nb_{14}O_{44}$: A New Li+ Container for High-Performance Electrochemical Energy Storage. *ENERGY Environ. Mater.* **2021**, *4* (1), 65–71. https://doi.org/10.1002/eem2.12098.

(36) Saritha, D.; Pralong, V.; Varadaraju, U. V.; Raveau, B. Electrochemical Li Insertion Studies on $WNb_{12}O_{33}$—A Shear ReO_3 Type Structure. *J. Solid State Chem.* **2010**, *183* (5), 988–993. https://doi.org/10.1016/j.jssc.2010.03.003.

(37) Yan, L.; Lan, H.; Yu, H.; Qian, S.; Cheng, X.; Long, N.; Zhang, R.; Shui, M.; Shu, J. Electrospun $WNb_{12}O_{33}$ Nanowires: Superior Lithium Storage Capability and Their Working Mechanism. *J. Mater. Chem. A* **2017**, *5* (19), 8972–8980. https://doi.org/10.1039/C7TA01784G.

(38) Maslen, E. N.; Fox, A. G.; O'Keefe, M. A. Atomic Scattering Factor. *Int. Tables Crystallogr. Vol. C* **2006**, *C*, 554–595. https://doi.org/10.1107/97809553602060000600.

(39) Jiang, J.; Li, Y.; Liu, J.; Huang, X.; Yuan, C.; Lou, X. W. (David). Recent Advances in Metal Oxide-Based Electrode Architecture Design for Electrochemical Energy Storage. *Adv. Mater.* **2012**, *24* (38), 5166–5180. https://doi.org/10.1002/adma.201202146.

(40) Itou, Y.; Ogihara, N.; Kawauchi, S. Role of Conductive Carbon in Porous Li-Ion Battery Electrodes Revealed by Electrochemical Impedance Spectroscopy Using a Symmetric Cell. *J. Phys. Chem. C* **2020**, *124* (10), 5559–5564. https://doi.org/10.1021/acs.jpcc.9b11929.

(41) Koçer, C. P.; Griffith, K. J.; Grey, C. P.; Morris, A. J. Lithium Diffusion in Niobium Tungsten Oxide Shear Structures. *Chem. Mater.* **2020**. https://doi.org/10.1021/acs.chemmater.0c00483.

(42) Li, T.; Nam, G.; Liu, K.; Wang, J.-H.; Zhao, B.; Ding, Y.; Soule, L.; Avdeev, M.; Luo, Z.; Zhang, W.; Yuan, T.; Jing, P.; Kim, M. G.; Song, Y.; Liu, M. A Niobium Oxide with a Shear Structure and Planar Defects for High-Power Lithium Ion Batteries. *Energy Environ. Sci.* **2022**, *15* (1), 254–264. https://doi.org/10.1039/D1EE02664J.

(43) Markervich, E.; Salitra, G.; Levi, M. D.; Aurbach, D. Capacity Fading of Lithiated Graphite Electrodes Studied by a Combination of Electroanalytical Methods, Raman

Spectroscopy and SEM. *J. Power Sources* **2005**, *146* (1), 146–150. https://doi.org/10.1016/j.jpowsour.2005.03.107.

(44) Moltved, K. A.; Kepp, K. P. The Chemical Bond between Transition Metals and Oxygen: Electronegativity, d-Orbital Effects, and Oxophilicity as Descriptors of Metal–Oxygen Interactions. *J. Phys. Chem. C* **2019**, *123* (30), 18432–18444. https://doi.org/10.1021/acs.jpcc.9b04317.

CHAPTER V: INVESTIGATING PSEUDOCAPACITIVE T-Nb_2O_5 THROUGH SLOW SCAN RATE CYCLIC VOLTAMMETRY

5.1 Overlook

Current electrochemical energy storage technology is based on materials possessing either high energy, such as batteries, or high power, such as capacitors. There is an increased need for next generation energy storage materials that display both high energy and high power. One class of energy storage materials of interest are pseudocapacitors, which store charge via faradaic processes in a non-diffusion limited charge storage mechanism, resulting in high energy density at fast (dis)charge rates. One promising pseudocapacitive material is T-Nb_2O_5, which operates in potential windows where lithium dendrites are unlikely to form, making it a safer alternative to graphite. In this work, we conducted slow scan rate cyclic voltammetry (SSCV) on T-Nb_2O_5 to better understand the pseudocapacitive charge storage mechanism. SSCV reveals peak separation below the electrochemical reversible peak separation predicted by the Nernst equation. One potential explanation of this is Li-ion intercalation into the bulk throughout the CV, resulting in no diffusion limitations and a square iV curve. Additionally, SSCV shows additional reduction peaks that have yet to be observed, highlighting the complex charge storage process in T-Nb_2O_5. However, cycling T-Nb_2O_5 to more negative potentials result in either irreversible reduction the carbonate-based electrolyte or irreversible phase changes, altering the iV curves of subsequent cyclic voltammetries.

5.2 Introduction

Due to the push for a renewable energy-based society, there is an increasing need for high-power and high-energy storage materials that can outperform current capacitors or commercial batteries. Electric double layer capacitors (EDLCs) possess high power density because they can be (dis)charged quickly compared to traditional batteries. However, they have lower energy density due to their reliance on maximizing surface area. A capacitor's charge storage mechanism relies on non-faradaic surface adsorption of the electrolyte, which provides fast energy storage and long lifetimes.[1] However, batteries possess higher volumetric energy density compared to EDLCs by utilizing Faradaic, reduction-oxidation (redox), reactions to store energy in the bulk of the material.[1,2] While batteries have high energy, they fail to provide high-power because they cannot be (dis)charged quickly. This is due to kinetic limitations from slow diffusion into the bulk of the material.[3–5] Additionally, cycling a traditional battery with a graphite anode at high-rates can result in the formation of dangerous lithium dendrites, potentially resulting in the battery short circuiting.[6,7]

Due to the need for materials with high energy and power density, understanding design principles that can improve lithium diffusion kinetics safely to replace graphite is of extreme importance. An interesting class of materials that possess high energy and power density are pseudocapacitors. Pseudocapacitive materials possess both high-energy through the reduction of the system through faradaic charge transfer, similar to a battery, as well high-rate charging due to the charge storage mechanism being non-diffusion limited, mimicking the electrochemical kinetics of a capacitors.[8–11] A family of materials of interest are transition metal oxides, which operate outside the voltage range at which dendrite formation occurs, resulting in improved safety, but lowers the potential window these cells can operate in.[12] One pseudocapacitive material of interest is the niobium oxide, T-Nb_2O_5. Schafer et al. investigated the structure of T-Nb_2O_5 in 1966 by describing the unit cell parameters and other structural aspects of various Nb_2O_5 polymorphs.[13] Additionally, Kato et al. conducted structural characterizations in 1975, where the space group of

T-Nb_2O_5 was determined (Pbam, International Crystal Systems database (ICSD), Collection Code 1840) and a more detailed description of the unit cell was provided.[14]

Augustyn et al. has shown that T-Nb_2O_5 possesses excellent high-rate capabilities, outperforming lithium titanate ($Li_4Ti_5O_{12}$) which is a commercial scale high-rate battery.[15] In their work, they conducted variable scan rate cyclic voltammetry (CV) to identify the scan rate at which T-Nb_2O_5 no longer operates like a pseudocapacitor. This was done by assuming that the current obeys a power-law relationship with the scan rate, in which a and b are adjustable parameters:[16]

$$i = av^b \qquad (1)$$

where I is the peak current (either anodic or cathodic), v is the scan rate, and b is the power law exponent. From this equation, the b parameter for both the cathodic and anodic peaks can be calculated by taking the log of peak current (i) for either anodic or cathodic peaks vs. the log of the scan rate (Equation 2) and finding the slope of the line.

$$\log(i) = b \cdot \log(v) + \log(a) \qquad (2)$$

In this analysis, surface limited (capacitor-like) kinetics result in a peak current that scales linearly with scan rate, corresponding to a b-value of 1. For a b-value of 0.5, the peak currents are proportional to the square root of the scan rate, indicating that the current response is diffusion-limited (battery-like).[17,18]

Simply put, if the current peaks in a CV scale linearly with the scan rate, the material is described as a pseudocapacitor. This analysis is a relatively easy method of investigating if electrochemical energy storage materials exhibit pseudocapacitive properties, where iV curves with peaks indicative of redox can have their charge storage mechanism assessed. If the power law analysis shows that the b value is 1, the material of interest is storing charge in a surface-limited (capacitive) mechanism. This approach has been used in investigating a wide variety of materials and as greatly added to the field of pseudocapacitors.

In this work, we conducted slow scan rate cyclic voltammetry (SSCV) to further investigate the electrochemical performance of T-Nb_2O_5 to better understand the pseudocapacitive response the material possesses. Through SSCV, new reduction peaks were observed at more negative potentials that are normally hidden due to *iR* drop and diffusion limitations that expand upon the lithiation and charge transfer processes in T-Nb_2O_5. Additionally, SSCV reveals that the peak separation is below what is predicted for an electrochemical reversible process predicted through the Nernst equation, highlighting the unique charge storage mechanisms in pseudocapacitive materials.

5.3 Experimental

5.3.1 Synthesis of T-Nb_2O_5

The samples were synthesized via high temperature solid state synthesis reactions following previous literature.[19] NbO_2 (Alfa Aesar, 99%) powder was ground in an agate mortar and pestle and then pressed into pellets using a hydraulic press (Caver Model: 4350.L) at 2 tons of pressure. The pellets were placed in an aluminum crucible and platinum boat and heated, open to air, in a Thermo Scientific Lindberg Blue M tube furnace. Samples were heated from 25°C at a rate of 10°C/min to 525°C, held for 100 hours and allowed to cool naturally in the oven, before the pellet was ground again for characterization.

5.3.2 Sample Characterization

The metal oxide powders were suspended in ethanol and drop-casted onto a Si B-doped zero diffraction slide. The samples were characterized by powder X-ray diffraction (XRD) using a Bruker D8 Discover DaVinci-Powder Diffractometer (Cu Kα radiation). Rietveld refinement was performed using Bruker's Diffrac.Topas software using CIF files from Inorganic Crystal Structure Database (ICSD).

5.3.3 Half-cell construction

Half-cell batteries were constructed in an argon glove box using the following components: stainless steel cases (MTI Corp, CR2032), a stainless-steel wave spring (MTI Corp, CR20WS), a stainless-steel spacer (MTI Corp, CR20-Spacer-05), and a glass microfiber (VWR, 691) separator were used. The metal oxide composite electrode was prepared by grinding a 5:4:1 ratio of niobium oxide particles, conductive carbon (Super P, Alfa Aesar), and polyvinylidene fluoride binder (PVDF, Sigma Aldrich) in an agate mortar and pestle. The metal oxide composite electrode is the cathode and lithium metal is the anode in this half-cell geometry. This mixture was dispersed in N-methyl pyrrolidone (NMP, Sigma-Aldrich) until the solution was slightly viscous. The slurry was doctor-bladed onto a copper substrate to cast a 100 μm-thick film. The film was dried overnight in a vacuum at approximately 120°C. The dried film was punched into several ¼ inch diameter electrodes and transferred into an argon glove box. Coin cells were constructed with the MTI coin cell case using a ½ inch diameter lithium metal electrode, and a 5/8 inch diameter separator was laid on top. Approximately, 80.0 μL of electrolyte containing 1M $LiClO_4$ dissolved in propylene carbonate (PC, Sigma Aldrich) or 1M $LiPF_6$ dissolved in a 1:1 volume ratio of ethylene carbonate/dimethyl carbonate (EC/DMC, Sigma Aldrich) was pipetted onto the separator. The cathode was placed on the separator after it had become saturated with electrolyte, followed by the stainless-steel spacer, spring, and finally the end cap. The cells were pressed with 0.9 tons of pressure using a compact digital pressure controlled electric crimper (MTI MSK-160E). The cells rested for 12 hours before electrochemical measurements were performed to allow the electrolyte to fully saturate the separator.

5.3.4 Electrochemical Testing

The coin cells were cycled on an Arbin battery tester (LBT-20084) at a C-rate of 1C or C/3, in which C-rate is the current which a battery is discharged relative to its theoretical capacity. The theoretical capacity is calculated by, $Q_{theoretical} = nF/3.6M$, where n is the number of electrons transferred per formula unit, F is Faraday's constant, 3.6 is a conversion factor between coulombs and mAh/g, and M is the molecular weight. The C-rate was calculated according to following equation: $I = (Q_{theoretical} \times m)/t$, where I is the current applied, m is the mass of active material, and t is time in hours. Following constant current cycling, slow scan-rate cyclic voltammetry was conducted on a CH instrument (CHI 1240 and CHI 1010A) and Autolab potentiostat (PGSTAT128N).

5.4 Results

In this work, we investigated the pseudocapacitive material, T-Nb_2O_5 via slow scan-rate cyclic voltammetry. Prior work conducted by Augustyn et al. shows that T-Nb_2O_5 possesses a charge storage mechanism that is not limited my diffusion, and mimics a surface-limited mechanism similar to electrochemical double layer capacitors (EDLCs).[15]

In a typical reaction, NbO_2 was mixed in an agate mortar and pestle, pressed into a pellet, and heated to a setpoint temperature (see Experimental Methods for details). Figure 5.1 shows the powder x-ray diffraction pattern for T-Nb_2O_5, while the Rietveld refinement utilized a crystallographic information file (CIF) from the Inorganic Crystal Structure Database (ICSD) (collection code 1840, and Pbam space group). Through comparing the model diffraction and

Rietveld refinement with the experimental data, the correct phase of T-Nb_2O_5 was indeed synthesized.

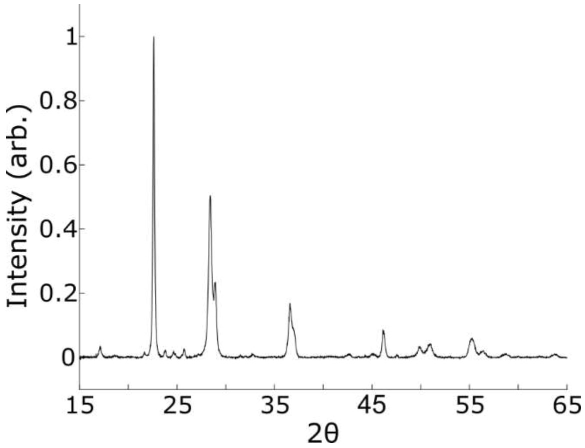

Figure 5.1. PXRD pattern of T-Nb_2O_5.

Having characterized the structure of the T-Nb_2O_5, we investigated the electrochemical behavior, and performance has Li-ion insertion hosts. The electrochemical performance was investigated by fabricating coin cells in a 5:4:1 ratio of active material, conductive carbon, and PVDF binder. These additives where utilized to help minimize the *iR* loss due to the poorly conductive metal oxide particles and aid in the mechanical stability and electrical contact upon cycling, the ratio was not optimized for battery performance.[20–22] Each electrochemical cell underwent galvanostatic cycling at a C-rate of C/3 or 1C to allow time for the (dis)charge storage processes to occur and to further minimize the *iR* loss effects.

Figure 5.2a-d. shows the (dis)charge curves for T-Nb_2O_5 in different potential windows and with two different electrolytes. When the lower potential window is limited to 1.2V vs. Li/Li^+ for both Figure 5.2a,c the (dis)charge curves look very similar, possessing a sloped curve on lithiation and delithiation, with a significant decrease in charge stored from cycle 1 to 2, and a monotonic capacity loss from cycle 2-20. Comparing the two cells that were cycled to a lower potential limit of 1.0V vs. Li/Li^+ (Figure 5.2b,d), the (dis)charge curves look different than the cells cycled in the more narrow potential window. Each cell displays a large discharge capacity loss after cycle 1, and a monotonic capacity loss with additional cycling. However, these cells each display a unique feature, where after the potential drop from 1.2V vs. Li/Li^+ there is an additional plateau at approximately 1.1V vs. Li/Li^+, resulting in a larger discharge capacity. This feature is only observed once for each cell and potential origins will be addressed in the Discussion section. We note that the specific capacities differ with each cell and attribute that to challenges getting accurate masses due to the fabrication of smaller electrodes.

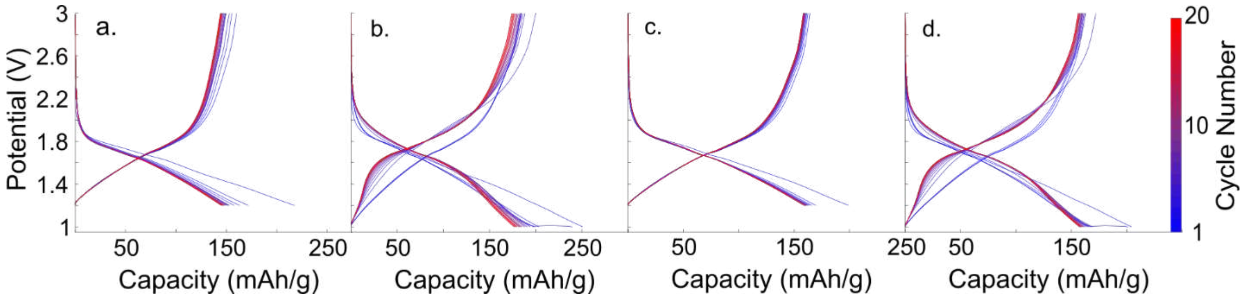

Figure 5.2. (a and b) Constant current measurement using 1M $LiClO_4$ in PC and (c and d) 1M $LiPF_6$ in a 1:1 ratio of EC:DMC.

Following galvanostatic cycling, slow scan rate cyclic voltammetry (SSCV) was conducted on these cells to further investigate the charge storage mechanism of T-Nb_2O_5. Figure 5.3 shows the CVs and normalized CVs for a variety of scan rates ranging from 1.5 to 400 μV/s for a cell using 1M $LiClO_4$ in PC. The *iV* curves look like the traditional description of a pseudocapacitive material, possessing a capacitive-like, square CV with clear redox peaks. When the scan-rate increases, the redox peaks become less clear, and the curves become more sloped and less square-like. Also, when looking at the *iV* curves as a function of scan rate, the cathodic peaks and anodic peaks shift to more negative and positive potentials with increased scan rate respectively, potentially due to *iR* drop or diffusion limitations. Lastly, both the cathodic and anodic peaks display a clear peak and shoulder feature that is lost with faster scan rates. Figure A4.*1*shows SSCV *iV* curves on an additional cell and shows similar trends, while Figure A4.2 shows a comparison of two different cells, showing reproducibility.

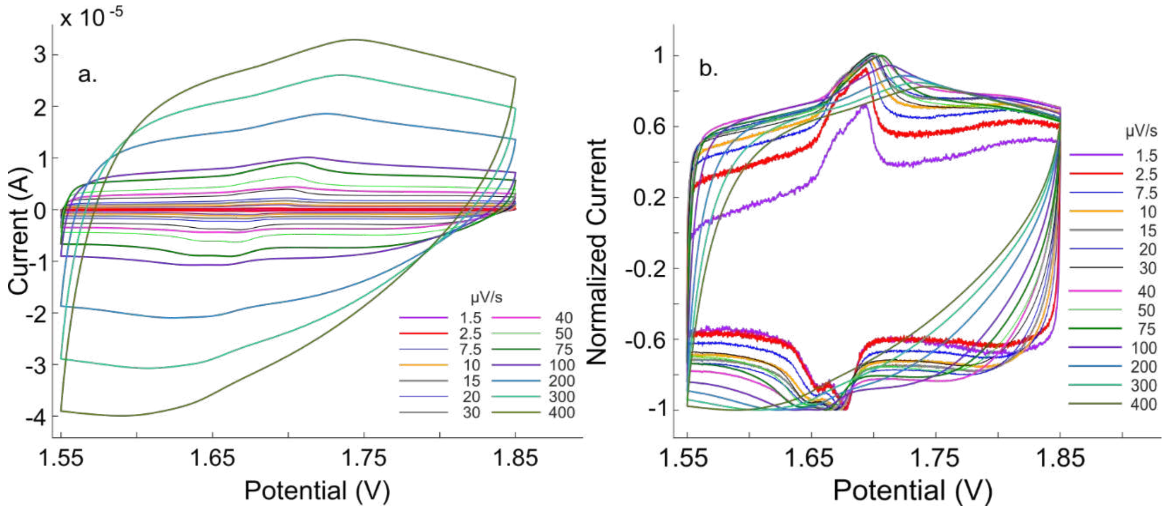

Figure 5.3. (a) Variable scan rate cyclic voltammetry on a T-Nb_2O_5 half-cell. (b) Cyclic voltammetry normalized with respect to the maximum cathodic current.

Figure 5.4 shows the power-law analysis from the previous CVs and shows that the b-values for the cathodic and anodic peaks is 0.9695 and 0.9665 respectively. These values near one indicate that the charge storage processes are not limited by diffusion and that the material is behaving as a pseudocapacitor.

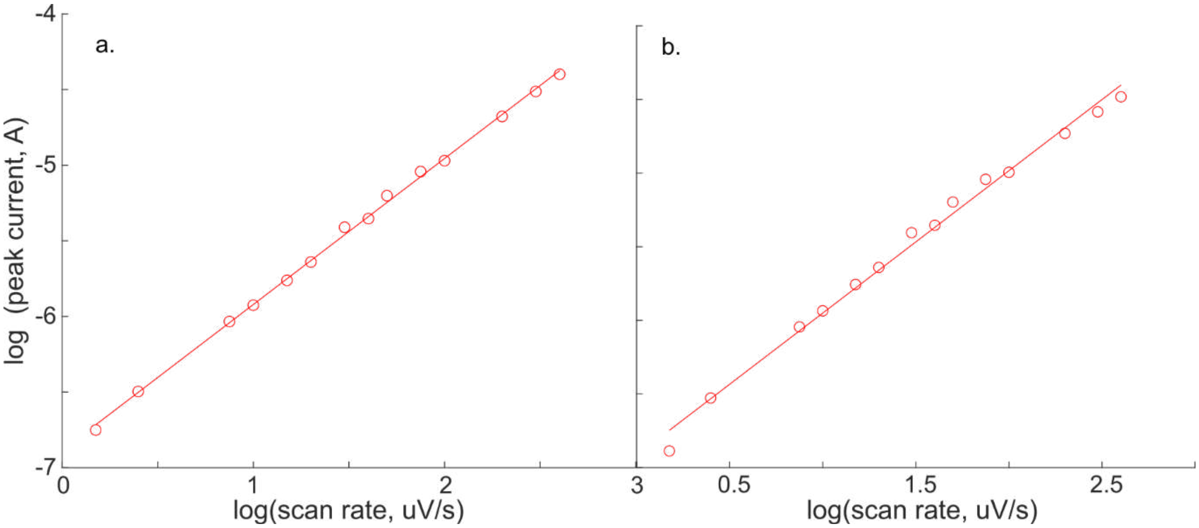

Figure 5.4. (a) Power-law analysis for the cathodic peak, the slope is 9695. (b) Power-law analysis for the anodic peak, slope is 0.9665.

Further analysis of the CVs beyond the power-law analysis reveals another interesting feature, which is the potential at which the peaks are observed. Figure 5.5 plots the peak separation vs scan rate and reveals that at scan rates below 100 μV/s, the peak separation is below 57 mV, which is predicted for a one-electron, electrochemically reversible reaction predicted by the Nernst equation. This unique feature will be addressed in detail in the Discussion section.

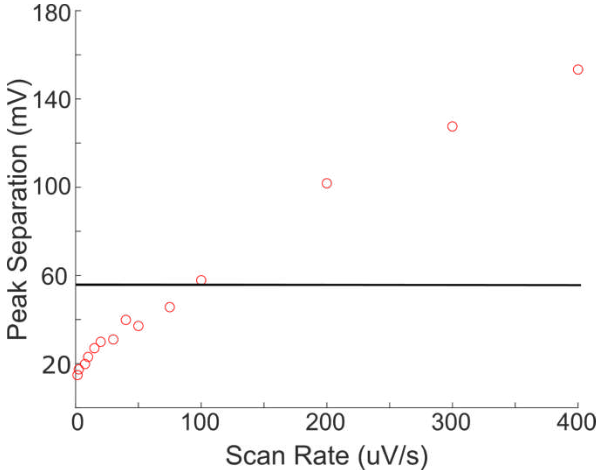

Figure 5.5. Anodic and cathodic peak separation vs scan rate, the black horizontal line is at 57 mV, indicated the peak separation for an electrochemically reversible process predicted by the Nernst equation.

When the potential window is extended to more negative potentials, unique features are observed. Figure 5.6 shows the previous CV and two linear sweep voltammetries (LSVs) showing good agreement between the CV and lithiation LSV, indicating reversible processes are occurring. However, below 1.5V vs. Li/Li$^+$ there is an increase in current, resulting in two new peak features at approximately 1.4V and 1.35V. Continuing more negative, there is a dramatic increase in current from approximately 1.1-1.0V vs. Li/Li$^+$. Following the lithiation LSV, the scan direction was reversed and a delithiation LSV was conducted. The shape of this LSV does not agree well with the narrower CV conducted prior, indicating that there is an irreversible process occurring below 1.5 V. In order to assess how this irreversibility affects the *iV* shape, and additional CV was conducted at 2.5 μV/s. Figure 5.6 shows a comparison of the first, narrow CV, both LSV steps, and the second CV. In this comparison, we can see a drastic change in CV shape, with a new cathodic feature at approximately, 2V, 1.85V, and 1.8V vs. Li/Li$^+$. Additionally, the low potential peaks present in the lithiation LSV are no longer present, indicating a loss of a redox process. Potential explanations of what is occurring here will be addressed in the Discussion section.

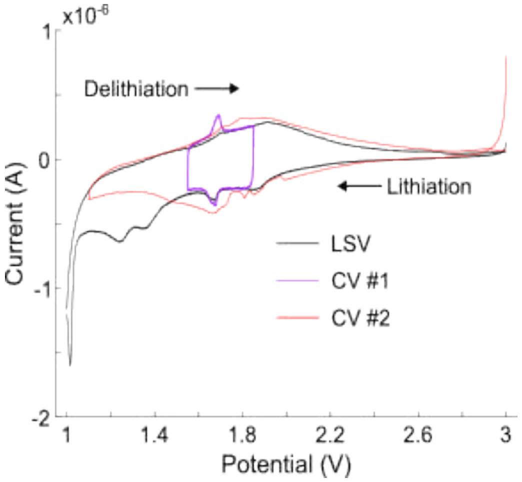

Figure 5.6 Comparison of LSVs and CVs cycled at 1.5 µV/s and 2.5 µV/s respectively.

5.5 Discussion

In this work, we conducted SSCV on the pseudocapacitive material, T-Nb_2O_5 to better understand the charge-storage mechanism. Through this technique we uncovered three unique features: 1. The peak separation of the anodic and cathodic peaks is lower than predicted through the Nernst equation. 2. SSCV reveals new peak features that haven't been observed and expands upon the accepted charge storage process. 3. The potential window T-Nb_2O_5 is cycled in plays a significant role in the reversibility of the charge storage mechanics.

First, we discuss possible processes occurring in T-Nb_2O_5 that result in the unique CV shape and why the peak separation is lower than the 57 mV predicted through the Nernst equation. One explanation of these features could be due to interlayer confinement effects. Boyd et al. conducted an *in-situ* investigation on birnessite, a layered mangenue oxide known for its pseudocapacitive properties, through CV and an electrochemical quartz crystal microbalance.[23] Through these two techniques, they uncovered that there is a continuous mass change in the active material when scanning through the potential window. This indicates a constant intercalation of cations into the unit cell prior to the redox peaks, resulting in the interlayer of the unit cells acting as an extension of the surface. This physical process could help describe the square iV curves commonly observed in pseudocapacitive materials through surface-limited charge transfer processes happening with intercalation, resulting in the current scaling linearly with scan rate. Additionally, this interlayer effect helps describe the lower than predicted peak separation we observe. If there is continuous intercalation of Li-ions into the bulk of T-Nb_2O_5, another layered material, throughout the CV, then Li-ions in the bulk of the material act as if absorbed to the surface of the electrode. If there are no diffusion considerations due to Li-ions being present in the material, the only limiting factor affecting the electrochemistry is the electron transfer, which would result in redox peaks being lower than the Nernst equation predicts. Self-assembled monolayers (SAMs) are an example of this, where redox active species are adsorbed onto the surface of the electrode, so the system is not diffusion limited. These systems display extremely symmetric CVs with very low peak separation.[18,24–26] Future work investigating the lithium ion insertion processes in T-Nb_2O_5 is necessary to identify the origin of these CV features.

SSCV also uncovers new peak features indicative of reduction and oxidation processes. The stored charge from the insertion of lithium ions into T-Nb_2O_5 is commonly represented as:

$$Nb_2O_5 + xLi^+ + xe^- \leftrightarrow Li_xNb_2O_5$$

with a theoretical capacity of 201.7 mAh/g.[19] However, this explanation of the lithium insertion and electron transfer only describes the CV response at faster scan rates, where there is only one clear reduction and oxidation peak present. By applying such a small potential change through

SSCV, additional peaks are shown that have yet to be addressed in literature, complicating the lithium insertion process. Figure 5.7 shows the LSV and corresponding moles of lithium inserted per formula unit of T-Nb_2O_5 with lines denoting x=0.5, 1, 1.5, 2, 2.5, and 3. We can see that these levels of lithiation correspond to potentials immediately following a reduction peak or are at the peak itself. It is because of this trend and presence of new peak features that we describe the lithium insertion into T-Nb_2O_5 as a series of the following discrete steps:

$$Nb_2O_5 + 0.5Li^+ + 0.5e^- \leftrightarrow Li_{0.5}Nb_2O_5$$

$$Nb_2O_5 + Li^+ + e^- \leftrightarrow LiNb_2O_5$$

$$Nb_2O_5 + 1.5Li^+ + 1.5e^- \leftrightarrow Li_{1.5}Nb_2O_5$$

$$Nb_2O_5 + 2Li^+ + 2e^- \leftrightarrow Li_2Nb_2O_5$$

$$Nb_2O_5 + 2.5Li^+ + 2.5e^- \leftrightarrow Li_{2.5}Nb_2O_5$$

$$Nb_2O_5 + 3Li^+ + 3e^- \leftrightarrow Li_3Nb_2O_5$$

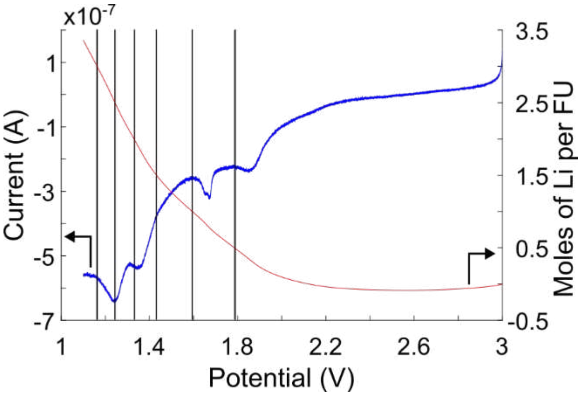

Figure 5.7. *iV* curve and corresponding moles of lithium inserted per formula unit for T-Nb_2O_5.

Continuing off the additional peak features observed when cycling to more negative potentials, there is also the issue of cycling irreversibility. As noted above, when cycled below 1.5V vs Li/Li^+, there are two peak features and a sharp current increase at approximately 1.1V. The two peak features are indicative of further reduction of T-Nb_2O_5 while the current spike resembles that of an irreversible reduction of electrolyte. Research has shown that commonly used carbonate solvents are reduced at approximately 1V vs. Li/Li^+.[27] Additionally, we can see similar features in the galvanostatic cycling of T-Nb_2O_5, shown in Figure 5.2, when cells were cycled below 1.2V, further supporting the hypothesis that there is an irreversible reaction due to electrolyte decomposition. Additionally, Figure A4.3 shows CV data for a T-Nb_2O_5 cell previously cycled with a constant current between 1V and 3V vs. Li/Li^+. We note significant differences in the CV shape for this cell when compared to the LSV data shown above, indicating that the reduction of electrolyte plays a significant role in the *iV* curves for T-Nb_2O_5. Lastly, we note previous research observed that there is an increase in irreversibility in T-Nb_2O_5 when cycled below *x* is greater than 2 in $Li_xNb_2O_5$.[28] We believe that future work is necessary to deconvolute the origin of irreversibility between crystallographic phase changes and electrolyte reduction to potentially allow multi-electron reduction in T-Nb_2O_5.

5.6 Conclusion

In this work, we synthesized T-Nb_2O_5 via solid-solid state reactions and conducted slow scan rate cyclic voltammetry (SSCV) to investigate the pseudocapacitive response to better understand electrochemical performance this material possesses. Through SSCV, we observed new reduction peaks at negative potentials that have yet to be observed due to *iR* drop and diffusion limitations that expand upon the lithiation and charge transfer processes in T-Nb_2O_5. These new peaks indicate that there are several charge transfer processes that can be seen due to the multi-electron reduction of niobium in the material. Additionally, SSCV reveals that the peak separation is below what is predicted for an electrochemical reversible process predicted through the Nernst equation. This feature could be due to continuous intercalation of Li-ions into the interlayer of T-Nb_2O_5 throughout the CV, where the interlayer is acting as an extension of the surface of the material. Li-ion insertion into the bulk of the material prior to the observed reduction peaks may help describe the capacitive, square *iV* curves commonly observed in pseudocapacitive materials. Lastly, we note an irreversible change in the CV if cycled to 1V vs. Li/Li$^+$, potentially due to reduction of the carbonate-based solvents or changes in the unit cell of T-Nb_2O_5. The work presented here helps shed light on the interesting charge storage mechanisms in pseudocapacitive materials and the development of high-energy, high-power materials for future energy storage materials.

5.7 References

(1) Evanko, B.; Boettcher, S. W.; Yoo, S. J.; Stucky, G. D. Redox-Enhanced Electrochemical Capacitors: Status, Opportunity, and Best Practices for Performance Evaluation. *ACS Energy Lett.* **2017**, *2* (11), 2581–2590. https://doi.org/10.1021/acsenergylett.7b00828.

(2) Winter, M.; Brodd, R. J. What Are Batteries, Fuel Cells, and Supercapacitors? *Chem. Rev.* **2004**, *104* (10), 4245–4269. https://doi.org/10.1021/cr020730k.

(3) van den Bergh, W.; Lokupitiya, H. N.; Vest, N. A.; Reid, B.; Guldin, S.; Stefik, M. Nanostructure Dependence of T-Nb_2O_5 Intercalation Pseudocapacitance Probed Using Tunable Isomorphic Architectures. *Adv. Funct. Mater.* **2020**, *2007826*, 1–11. https://doi.org/10.1002/adfm.202007826.

(4) Heubner, C.; Schneider, M.; Michaelis, A. Diffusion-Limited C-Rate: A Fundamental Principle Quantifying the Intrinsic Limits of Li-Ion Batteries. *Adv. Energy Mater.* **2020**, *10* (2), 1902523. https://doi.org/10.1002/aenm.201902523.

(5) Benedek, P.; Forslund, O.; Nocerino, E.; Yazdani, N.; Matsubara, N.; Sassa, Y.; Juranyi, F.; Medarde, M.; Telling, M. T. F.; Mansson, M.; Wood, V. Quantifying Diffusion through Interfaces of Lithium Ion Batteries Active Materials. *ACS Appl. Mater. Interfaces* **2020**. https://doi.org/10.1021/acsami.9b21470.

(6) Downie, L. E.; Krause, L. J.; Burns, J. C.; Jensen, L. D.; Chevrier, V. L.; Dahn, J. R. In Situ Detection of Lithium Plating on Graphite Electrodes by Electrochemical Calorimetry. *J. Electrochem. Soc.* **2013**, *160* (4), A588. https://doi.org/10.1149/2.049304jes.

(7) Guo, Z.; Zhu, J.; Feng, J.; Du, S. Direct in Situ Observation and Explanation of Lithium Dendrite of Commercial Graphite Electrodes. *RSC Adv.* **2015**, *5* (85), 69514–69521. https://doi.org/10.1039/C5RA13289D.

(8) Conway, B. E.; Birss, V.; Wojtowicz, J. The Role and Utilization of Pseudocapacitance for Energy Storage by Supercapacitors. *J. Power Sources* **1997**, *66* (1–2), 1–14. https://doi.org/10.1016/S0378-7753(96)02474-3.

(9) Conway, B. E.; Pell, W. G. Double-Layer and Pseudocapacitance Types of Electrochemical Capacitors and Their Applications to the Development of Hybrid Devices. *J. Solid State Electrochem.* **2003**, *7* (9), 637–644. https://doi.org/10.1007/s10008-003-0395-7.

(10) Augustyn, V.; Simon, P.; Dunn, B. Pseudocapacitive Oxide Materials for High-Rate Electrochemical Energy Storage. *Energy Environ. Sci.* **2014**, *7* (5), 1597–1614. https://doi.org/10.1039/C3EE44164D.

(11) Kim, J. W.; Augustyn, V.; Dunn, B. The Effect of Crystallinity on the Rapid Pseudocapacitive Response of Nb_2O_5. *Adv. Energy Mater.* **2012**, *2* (1), 141–148. https://doi.org/10.1002/aenm.201100494.

(12) Ding, H. Song, Z. Zhang, H. Zhang, H. Li, X. Niobium-Based Oxide Anodes toward Fast and Safe Energy Storage: A Review | Elsevier Enhanced Reader. *Mater. Today Nano* **2020**, *11*, 1–23. https://doi.org/10.1016/j.mtnano.2020.100082.

(13) Schäfer, H.; Gruehn, R.; Schulte, F. The Modifications of Niobium Pentoxide. *Angew. Chem. Int. Ed. Engl.* **1966**, *5* (1), 40–52. https://doi.org/10.1002/anie.196600401.

(14) Kato, K.; Tamura, S. Die Kristallstruktur von T-Nb_2O_5. *Acta Crystallogr. Sect. B* **1975**, *31* (3), 673–677. https://doi.org/10.1107/S0567740875003603.

(15) Augustyn, V.; Come, J.; Lowe, M. A.; Kim, J. W.; Taberna, P.-L.; Tolbert, S. H.; Abruña, H. D.; Simon, P.; Dunn, B. High-Rate Electrochemical Energy Storage through Li^+ Intercalation Pseudocapacitance. *Nat. Mater.* **2013**, *12* (6), 518–522. https://doi.org/10.1038/nmat3601.

(16) Lindström, H.; Södergren, S.; Solbrand, A.; Rensmo, H.; Hjelm, J.; Hagfeldt, A.; Lindquist, S.-E. Li+ Ion Insertion in TiO_2 (Anatase). 2. Voltammetry on Nanoporous Films. *J. Phys. Chem. B* **1997**, *101* (39), 7717–7722. https://doi.org/10.1021/jp970490q.

(17) Choi, C.; Ashby, D. S.; Butts, D. M.; DeBlock, R. H.; Wei, Q.; Lau, J.; Dunn, B. Achieving High Energy Density and High Power Density with Pseudocapacitive Materials. *Nat. Rev. Mater.* **2019**. https://doi.org/10.1038/s41578-019-0142-z.

(18) Bard, A. J.; Faulkner, L. R. *Electrochemical Methods : Fundamentals and Applications*; Wiley, 2001.

(19) Griffith, K. J.; Forse, A. C.; Griffin, J. M.; Grey, C. P. High-Rate Intercalation without Nanostructuring in Metastable Nb_2O_5 Bronze Phases. *J. Am. Chem. Soc.* **2016**, *138* (28), 8888–8899. https://doi.org/10.1021/jacs.6b04345.

(20) Li, R.; Liang, G.; Zhu, X.; Fu, Q.; Chen, Y.; Luo, L.; Lin, C. $Mo_3Nb_{14}O_{44}$: A New Li^+ Container for High-Performance Electrochemical Energy Storage. *ENERGY Environ. Mater.* **2021**, *4* (1), 65–71. https://doi.org/10.1002/eem2.12098.

(21) Jiang, J.; Li, Y.; Liu, J.; Huang, X.; Yuan, C.; Lou, X. W. (David). Recent Advances in Metal Oxide-Based Electrode Architecture Design for Electrochemical Energy Storage. *Adv. Mater.* **2012**, *24* (38), 5166–5180. https://doi.org/10.1002/adma.201202146.

(22) Itou, Y.; Ogihara, N.; Kawauchi, S. Role of Conductive Carbon in Porous Li-Ion Battery Electrodes Revealed by Electrochemical Impedance Spectroscopy Using a Symmetric Cell. *J. Phys. Chem. C* **2020**, *124* (10), 5559–5564. https://doi.org/10.1021/acs.jpcc.9b11929.

(23) Boyd, S.; Ganeshan, K.; Tsai, W.-Y.; Wu, T.; Saeed, S.; Jiang, D.; Balke, N.; van Duin, A. C. T.; Augustyn, V. Effects of Interlayer Confinement and Hydration on Capacitive Charge

Storage in Birnessite. *Nat. Mater.* **2021**, *20* (12), 1689–1694. https://doi.org/10.1038/s41563-021-01066-4.

(24) Gooding, J. J.; Mearns, F.; Yang, W.; Liu, J. Self-Assembled Monolayers into the 21st Century: Recent Advances and Applications. *Electroanalysis* **2003**, *15* (2), 81–96. https://doi.org/10.1002/elan.200390017.

(25) Ulman, A. Formation and Structure of Self-Assembled Monolayers. *Chem. Rev.* **1996**, *96* (4), 1533–1554. https://doi.org/10.1021/cr9502357.

(26) Lenhard, J. R.; Murray, R. W. Chemically Modified Electrodes. 13. Monolayer/Multilayer Coverage, Decay Kinetics, and Solvent and Interaction Effects for Ferrocenes Covalently Linked to Platinum Electrodes. *J. Am. Chem. Soc.* **1978**, *100* (25), 7870–7875. https://doi.org/10.1021/ja00493a014.

(27) Zhang, X.; Kostecki, R.; Richardson, T. J.; Pugh, J. K.; Ross, P. N. Electrochemical and Infrared Studies of the Reduction of Organic Carbonates. *J. Electrochem. Soc.* **2001**, *148* (12), A1341. https://doi.org/10.1149/1.1415547.

(28) Han, H.; Jacquet, Q.; Jiang, Z.; Sayed, F. N.; Jeon, J.-C.; Sharma, A.; Schankler, A. M.; Kakekhani, A.; Meyerheim, H. L.; Park, J.; Nam, S. Y.; Griffith, K. J.; Simonelli, L.; Rappe, A. M.; Grey, C. P.; Parkin, S. S. P. Li Iontronics in Single-Crystalline T-Nb_2O_5 Thin Films with Vertical Ionic Transport Channels. *Nat. Mater.* **2023**, *22* (9), 1128–1135. https://doi.org/10.1038/s41563-023-01612-2.

CHAPTER VI: OUTLOOK AND FUTURE DIRECTIONS: UNDERSTANDING STRUCTURAL FEATURES FOR HIGH POWER NIOBIUM-BASED ANODES

6.1 Introduction

Niobium-based anode materials are of interest for lithium-ion batteries (LIBs) because of their ability to store large amounts of lithium ions in the bulk of the material, providing larger capacities than electrochemical double layer capacitors.[1] Additionally, niobium-based anodes have been shown to possess significantly higher power densities than traditional graphite based anodes, allowing for fast (dis)charge capabilities.[2] For example, $Nb_{16}W_5O_{55}$ can store approximately 542 and 356 AhL^{-1} when charged at a C-rate of 1C and 20C (60-min and 3-min discharges respectfully) whereas graphite can store approximately 104 AhL^{-1} at a rate of 1C. Current commercial batteries often use graphite as the anode material, but graphite has a significant drawback: lithium tends to deposit on its surface at high (dis)charge rates.[3,4] This can lead to the growth of lithium dendrites during repeated cycling, which poses a risk of short-circuiting the cell and causing explosions.[5,6] Therefore, fundamental research on design principles for next-generation, safe, and high-rate anode materials is crucial. Furthermore, because these niobium electrodes store charge through lithium-ion intercalation and not conversion/alloy processes, the volume change when lithiated is significantly lower. Silicon is an example of a conversion electrode that undergoes a volume change of 310%, whereas niobium-based intercalation electrodes experience approximately 10% when lithiated. [2,7–9] The large volume changes when lithiated is important because large volume changes can result in strain and cracking in the electrode.[10,11] These processes lead to mechanical instability causing electrode fracturing and loss of active material, decreasing capacity and cyclability.[12,13] While these materials have the exciting electrochemical capabilities, there are still fundamental studies necessary to better understand the origins of these impressive charge storage processes to gain design principles for next-generation energy storage systems.

Several questions relating to the structure property relationships in niobium-based electrodes are presented here, with methods to investigate these processes being discussed in greater detail below. As discussed in Chapter II, the block size plays a crucial role in the electrochemical performance of W-R materials. However, the role block orientation plays on Li-ion diffusion and energy of potential storage sites is still unclear, with future research projects being addressed in section 6.2.

Chapter III and IV discuss two important methods to alter the electrochemical performance of two W-R crystallographic shear compounds, the 3×4 $Nb_{12}WO_{33}$ and 4×4 $Nb_{14}W_3O_{44}$, through elemental substitution, i.e., W substituted for Mo, and through the introduction of some form of disorder. These two methods raise questions as to what the relationship between these structural changes and improvements to electrochemical performance. Possible future research projects are addressed in section 6.2.

Chapter V discusses the pseudocapacitive material T-Nb_2O_5 examined through slow scan rate cyclic voltammetry. In this chapter, the slow scan rate revealed new peak features that have yet to be observed in literature. Additionally, the cathodic and anodic peak separation is below the 57 mV that the Nernst equation predicts for an electrochemically reversible system, indicating that the charge storage mechanism here is more complicated that traditionally assumed for pseudocapacitive materials. Section 6.3 addresses possible research methods to further understanding pseudocapacitive materials.

6.2 Future directions to understand structure-property relationships in Wadsley-Roth materials

While there have been computational and experimental investigations relating the structure property relationships in W-R crystallographic shear structures, the role the block structure plays in the electrochemical performances is still unclear. Work conducted by Cava et al. and expanded upon by Van der Ven et al. classified the structural arrangements of W-R structures. [14,15] Through this work, the wide variety of structural freedom is organized based on block size, relative shift between neighboring blocks as vector (direction and magnitude of shift), presence of a tetrahedra, and if there is a mixture of block sizes. With these classifications in mind, we can propose computational and experimental studies to investigate the role block orientation plays.

One study that could be conducted is a systematic investigation of two 3x4 compounds, $Nb_{12}WO_{33}$ and $TiNb_{24}O_{62}$, which both possess a tetrahedral site at the edge of the block though with different block arrangements, as shown in Figure 6. 1.

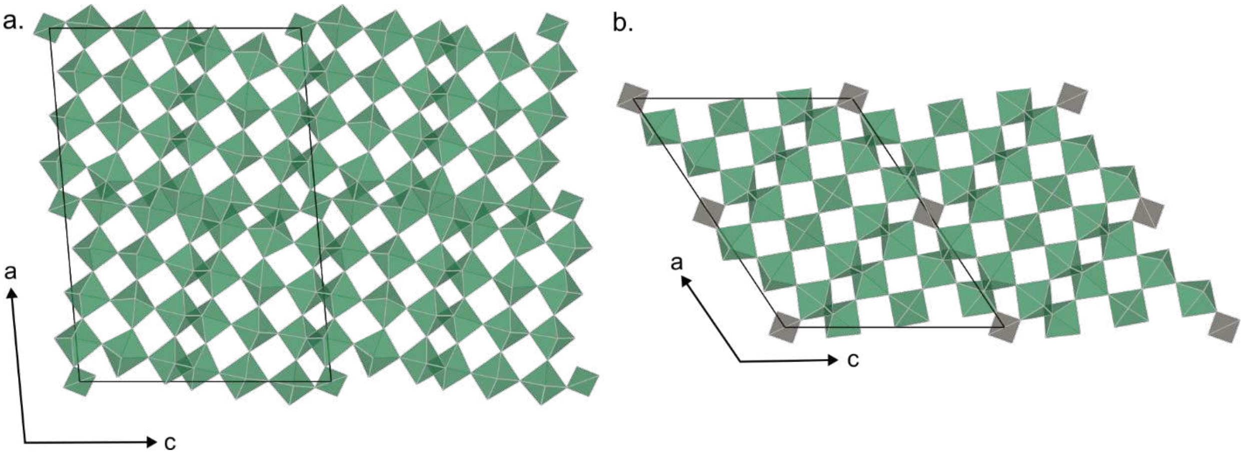

Figure 6. 1. Unit cell illustration of (a) $TiNb_{24}O_{62}$ and (b) $Nb_{12}WO_{33}$.

Samples will be synthesized via high temperature solid-state methods and characterized via powder x-ray diffraction (XRD), Raman spectroscopy, and scanning electron microscopy

(SEM) before constructing electrochemical cells. Galvanostatic cycling and electrochemical impedance spectroscopy (EIS) will be conducted to investigate differences in capacity, cyclability, and charge transfer resistances and diffusion coefficients. Computations should be conducted to assess for differences in activation barriers for lithium transport in the unit cell or changes in lithium binding energies, specifically focusing on the differences in block arrangements that may help explain experimental trends. An example computation would be nudged elastic band, such as those already conducted on $Nb_{12}WO_{33}$, highlighting the large activation energies lithium ions need to overcome to access sites along the block edge.[16]

6.3 How stacking faults can alter the electrochemical performance in W-R materials

Another question that arises from the work presented in Chapter III is how do structural defects, specifically stacking faults or Wadsley-defects, relate to the electrochemical performance. Early work conducted by Allpress, Sanders, and Wadsley have shown that W-R crystallographic shear compounds can possess intergrown phases and blocks that change the structures significantly. [17,18] One example present in these works is H-Nb_2O_5 (3×4 and 3×5 blocks) intergrown into $Nb_{12}WO_{33}$ (3×4 blocks), operating as stacking faults. $Nb_{12}WO_{33}$ can be represented as repeating rows A-A-A-A, and H-Nb_2O_5 can be represented as A-B-A-B-A, where A is 3×4 and B is 3×5 blocks. How these stacking orientations effect the electrochemical performances is an interesting question, especially considering recent work by Liu et al. where they synthesized both ordered and defective H-Nb_2O_5, assessed the electrochemical performances, and performed computations to ascertain the origins of the differences between samples.[19] Their results show that the defective samples possess stacking faults where the 3×4 and 3×5 blocks are rotated into different orientations when compared to the ordered samples and possess higher capacities, smaller volume changes upon lithiation, and are more reversible with additional cycling. Computations predict that the defective samples have more stable lithium ion binding sites, facilitating higher levels of intercalation while the perpendicular arrangements of blocks lower strain and minimize volume expansions. Lastly, Allpress and Roth investigated the effect of annealing on the concentration of Wadsley defects in the Nb-W-O system and found that by increasing annealing time at high-temperatures, the concentration of defects is reduced, setting the ground work for this proposed investigations.[20]

To investigate the role stacking faults play in the electrochemistry of W-R compounds, a series of intergrown $Nb_{12}WO_{33}$ (3×4 blocks) and H-Nb_2O_5 (3×4 and 3×5 blocks) samples with different degrees of faults will be synthesized following the solid-state methods provided by Allpress, Sanders, and Wadsley as referenced above. Advanced diffraction and spectroscopy techniques, such as x-ray absorption spectroscopy (XAS) and atomic pair distribution function (PDF) collected at synchrotron sources would assist in the characterization of defects. Additionally, high quality transmission electron microscopy (TEM) will be conducted to further evaluate the defects.[18,19,21,22] Following defect characterization, electrochemical cells will be assembled to conduct galvanostatic cycling and EIS experiments to compare capacity stored at different rates, cyclability, charge transfer resistances and diffusion coefficients as a function of stacking fault density. Computations should be conducted to analyze differences in activation energy barriers for lithium transport in the unit cells or changes in lithium binding energies that may help explain experimental trends.

6.4 Investigating the role the tetrahedral position plays in W-R materials

In a similar approach to 6.2, the role the tetrahedra site plays on the electrochemical performance is still unclear. In Chapters III and IV, Raman spectroscopy indicates that both molybdenum and tungsten prefer to occupy the tetrahedral sites and a subsequent improvement in discharge capacity is observed with molybdenum introduction. Additionally, work conducted by Seshadri et al. has shown that isostructural PNb_9O_{25} and VNb_9O_{25} possess significantly different electrochemical signatures with just one elemental change.[23] Experimental and computational investigations have shown that metals possessing higher oxidation state prefer to occupy the tetrahedral and block center environments.[7,24] Given the compositional flexibility of W-R materials, a series of syntheses of isovalent substitutions should be conducted to compare changes in electrochemical performance along with structural characterization and computational studies to identify the reasons for performance differences. Isovalent substitutions are preferred for this study because non-isovalent substitutions would introduce different transition metals with differing oxidations states; thus, changing the electronic structure of the intrinsic material. One potential series of substitutions involves expanding upon the work presented in the previous chapters, with a systematic investigation of W, Mo, and Cr substitutions into $Nb_{12}WO_{33}$. There is already literature on Cr introduction into W-R materials, with a Cr^{3+} and Nb^{5+} doped $Ti_2Nb_{10}O_{29}$ and fully substituted $CrNb_{11}O_{29}$.[25,26] Furthermore, $Nb_{12}WO_{33}$ is a good model system because there is a strong preference for transition metals with high oxidations state occupying the tetrahedral sites, while the larger block sizes of $Nb_{14}W_3O_{44}$ and $Nb_{16}W_5O_{55}$ each of a probability of cation disorder being present in the block center. [2,7,24]

In this study, $Nb_{12}WO_{33}$, $Nb_{12}MoO_{33}$, and $Nb_{12}CrO_{33}$ will be synthesized via high temperature solid-state methods and characterized via XRD, Raman spectroscopy, and SEM before being assembled into electrochemical cells. After cell fabrication, galvanostatic cycling and electrochemical impedance spectroscopy will be conducted to elucidate capacity stored at different rates, cyclability, charge transfer resistances and diffusion coefficients. Additionally, computations should be conducted to analyze differences in activation barriers for lithium transport in the unit cell or changes in lithium binding energies that may help explain experimental trends.

Another possible study to investigate the role the tetrahedra plays is to synthesize two structurally similar W-R shear structures, where one possesses a tetrahedral site while the other does not. For example, a systematic study could be conducted on $TiNb_{24}O_{62}$ and $Ti_2Nb_{10}O_{29}$, which are both 3×4 block sizes, and $TiNb_{24}O_{62}$ has a tetrahedral site in the unit cell while $Ti_2Nb_{10}O_{29}$ does not (Figure 6.2). It is worth noting that for both compounds, the oxidation states of Nb and Ti and 5+ and 4+ respectively, indicating that there should be no changes in electronegativity due to additional or fewer electrons.

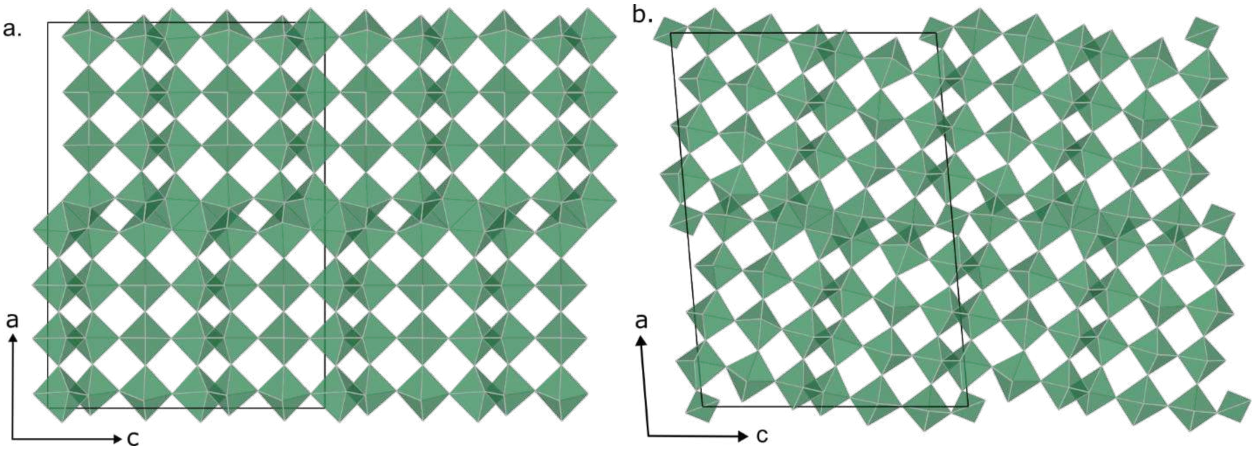

Figure 6.2. Unit cell illustrations of (a) $Ti_2Nb_{10}O_{29}$ and (b) $TiNb_{24}O_{62}$

6.5 Further elemental substitution of W-R materials

An additional question in W-R literature is what role do octahedral distortions play in the energy storage processes? It was hypothesized in work done by Morris et al. that the degree of distortions may play a role in changing lithium binding energies and therefore the electrochemistry in Nb-W-O materials.[7] Both niobium and tungsten have been classified as moderate Jahn-Teller distorters, while molybdenum has been classified as a strong distorter, where the strength of distorter is the degree off-center the metal center is.[27] We have seen an increase in capacity in both

3×4 $Nb_{12}WO_{33}$ and 4×4 $Nb_{14}W_3O_{44}$, when substituting the moderate distorter W for the strong distorter Mo, but it would be interesting to see if the trend continues. As discussed in Chapters III and IV, the transition metals along edge sites may experience metal-metal bonding, resulting in lower energy orbitals for electrons to occupy and more positive potential features appearing in the constant current and $\mathrm{d}Q/\mathrm{d}V$ plots.[23,28] We can continue to test the relationship between degree of distortion and electrochemical performance by synthesizing zirconium substituted 4×4 $Nb_{14}W_3O_{44}$, where zirconium has been classified as a weak distorter, shown in Figure 6.3.

In this study, $Nb_{14}W_3O_{44}$, $Nb_{14}Mo_3O_{44}$, and $Nb_{14}Zr_3O_{44}$ will be synthesized via high temperature solid-state methods and characterized via XRD and neutron diffraction to probe for the degree of octahedral distortions, along with Raman spectroscopy and SEM before being assembled into electrochemical cells. After cells are fabricated, the electrochemical performance will be assessed through different electrochemical techniques and the electrochemical performances will be compared. Additionally, the diffraction studies will guide computations to analyze differences in activation barriers for lithium transport in the unit cell or changes in lithium binding energies as a function of degree of distortions present, which will help explain experimental trends.

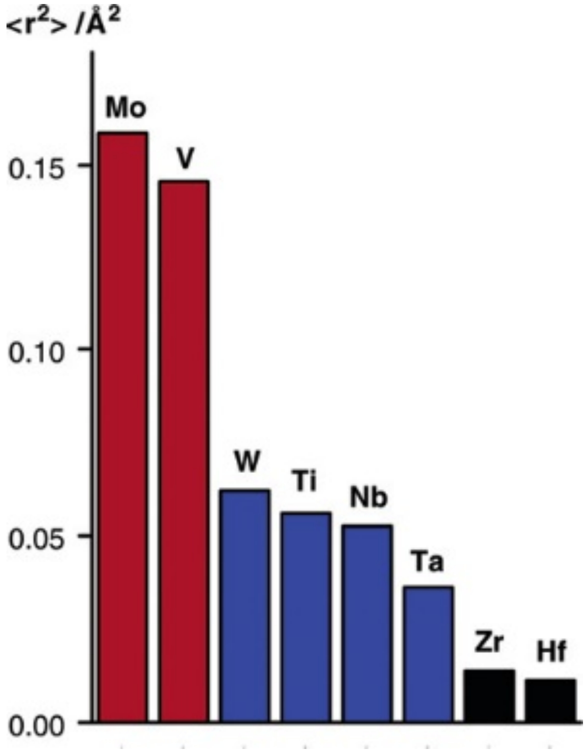

Figure 6.3. Average magnitude of the off-center distortions for individual d^0 transition metal cations. Reprinted with permission from Chem. Mater. *2006, 18, 14, 3176–3183*. Copyright 2006 American Chemical Society

6.6 Alternative methods to investigate Nb-based anode materials

Throughout the work presented here, ensemble level measurements were conducted through the fabrication of electrochemical coin cells. While these cells provide useful information on performance metrics necessary for next generation energy storage materials, the addition of conductive carbon and polymer additives adds to the complexity of the system. Optical microscopy has been shown to be a useful tool in deconvoluting the system to better understand the electrochemistry intrinsic to these storage systems by allowing for direct observation of the active material particles.[29–33] Some examples of optical microscopy being used to investigate energy storage materials are probing for particle volume changes during (de)lithiation, electrode delamination off the substrate, as well as dendrite formation.[32–35] Furthermore, many transition metals commonly used in metal oxide anodes are electrochromic, such as niobium and tungsten, undergoing color changes when reduced or oxidated. Traditional microscopy can be used to further investigate the electrochemical performance of these electrochromic materials by correlating the level of reduction (lithiation) to color change, gaining valuable information about the materials, with an illustration of the experimental set up shown in Figure 6.4.[36–40]

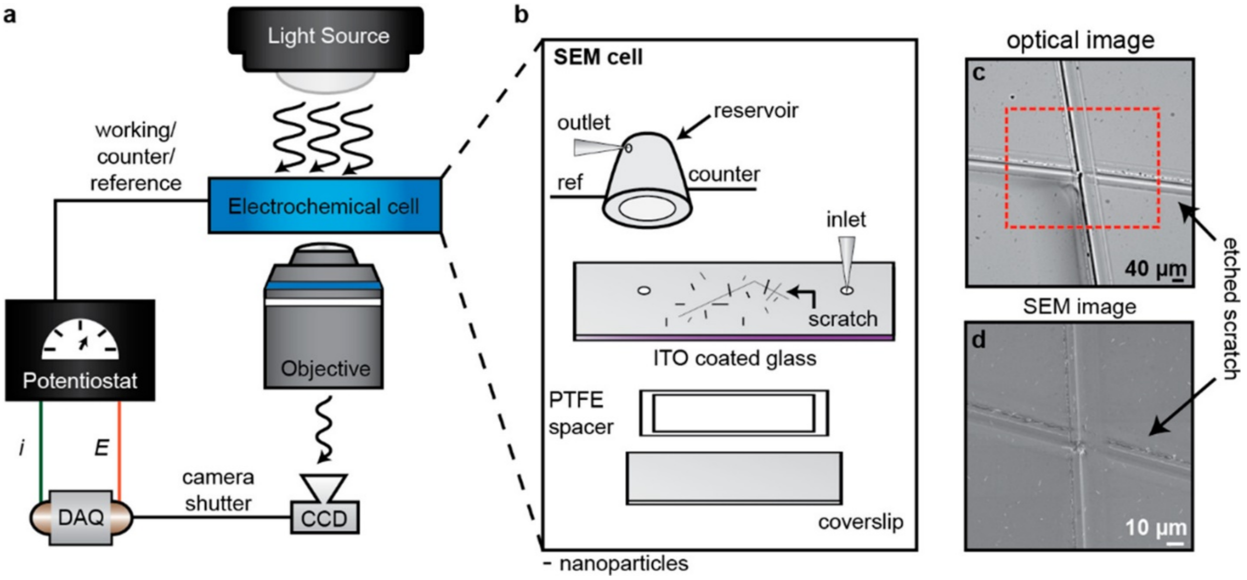

Figure 6.4. Experimental setup for electro-optical imaging and electron microscopy. (a) An optically transparent three-electrode electrochemical cell is mounted on a microscope and is illuminated from above. The light transmitted through the sample is collected by a microscope objective and imaged on an EM-CCD camera. The CCD camera and potentiostat are connected to a data acquisition card (DAQ). (b) Optically transparent electrochemical cell design, including Pt counter and Ag/AgCl reference electrodes. (c) Optical and (d) SEM image of a macroscopic scratch mark that is used for correlated optical and SEM imaging. Reprinted with permission from *Anal. Chem.* 2019, 91, 23, 14983–14991. Copyright 2019 American Chemical Society

An additional microscopy technique of interest is scanning electrochemical cell microscopy (SECCM), in which a micropipette is filled with electrolyte and quasi-counter reference electrode. This probe can move in the *xyz* directions, allowing for spatially resolved electrochemistry on individual electrode particles once the tip is moved down into contact with the working electrode and particles. In addition to localized electrochemistry, a transparent conductive substrate can be used to allow for microscopy to be coupled with electrochemical experiments, with an illustration of the setup shown in Figure 6.5. With the combination of localized electrochemistry and microscopy, single particle experiments can be conducted to gain a better understanding of structure property relationships, such has how particle size, orientation, and microstructure relates to capacity and charge storage.[41–43]

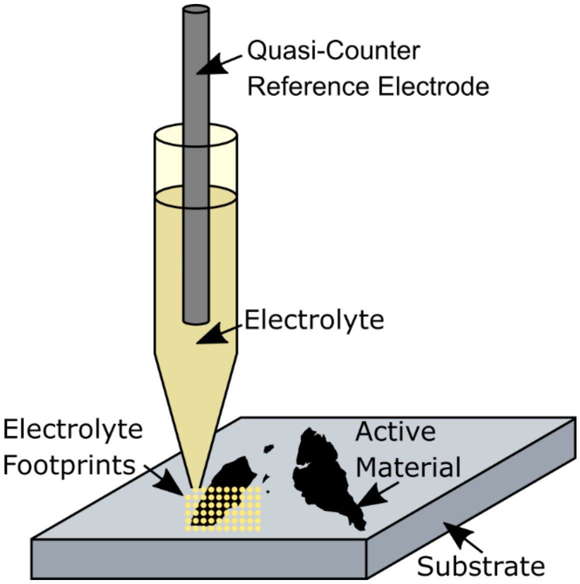

Figure 6.5. Illustration of SECCM in operation.

SECCM can also be utilized to investigate pseudocapacitive materials, with the micropipette tip allowing for high throughput investigations of these particles. Methods of fabricating traditional electrochemical cells or microelectrodes involves time intensive steps for each cell fabricated.[44,45] With the spatial freedom allowed by SECCM, multiple particles could be analyzed in the time it takes to build a single cell. Additionally, there have been calls in the field to adapt microelectrolytic techniques, stating "While such a systematic search can be quite cumbersome and time-consuming in real working conditions, recourse to time-resolved microelectrolytic techniques may alleviate and speed up the observation and understanding of the system functioning".[46,47] Recently, Roehrich and Sepunaru conducted EIS on individual Prussian blue pseudocapacitive nanoparticles.[48] These measurements showed electronic conductivity and ion transport differing up to an order of magnitude, even among particles from the same synthesis. The authors note particle size or morphology cannot describe the electrochemical observations, warranting future work. Furthermore, SECCM and EIS can be conducted on the pseudocapacitive materials, T-Nb_2O_5, noting the electrochromic nature of niobium would further add to the information gained through this technique. A combination study of optical microscopy, electron microscopy, electron diffraction, and electrochemistry can be conducted to identify macro and microstructural features that relate to pseudocapacitive charge storage mechanisms.

6.7 Additional methods to investigate pseudocapacitive materials

As shown in Chapter V, when cyclic voltammetry (CV) was conducted with slow scan-rates the anodic and cathodic peak separation is below 57 mV that the Nernst equation predicts for an electrochemically reversible system. This implies that electrochemical charge storage processes can behave different than those commonly used to attempt fit pseudocapacitive materials, and that different modelling techniques are needed to better understand the mechanisms present.[49–55]

One potential field of electrochemistry to utilize in order to better understand pseudocapacitive materials is self-assembled monolayers (SAMs) which are ordered molecular assemblies that form on the electrode surface through adsorption. Due to the chemisorption of the active species directly on the electrode, electrolyte interface, there are no diffusion limitations, with only charge-transfer limitations present in the system.[56–58] Furthermore, work conducted by Lenhard and Murray on understanding SAMs decay kinetics and solvent interactions of ferrocenes linked to platinum electrodes illustrates similar behavior when conducting CVs, shown Figure 6.6.[59] In this study, the ferrocenes adsorbed on the platinum surface displayed a peak separation of 22 mV when cycled at 200mV/s highlighting the non-Nernstian behavior of chemisorbed species on the electrode surface. Furthermore, the peak currents scale linearly with scan rate, like pseudocapacitive materials. With these behaviors in mind, adapting equations used to describe the physical processes of SAMs, in an attempt to understand the charge storage processes relating to pseudocapacitive materials should be pursued.[57]

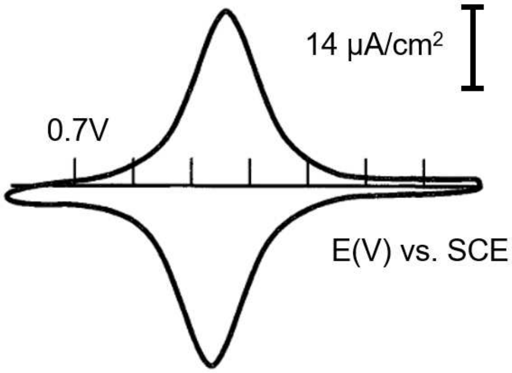

Figure 6.6. Cyclic voltammograms of electrodes with a SAM with a ferrocene attachment on a Pt electrode, with a standard calomel electrode (SCE) reference electrode. Reprinted with permission from *J. Am. Chem. Soc*, **100**, 7870 (1978). Copyright 1978, American Chemical Society.

6.8 Outlook

The future directions presented here are just a few possible methods to better understand the high-rate capabilities of niobium-based anode materials. Through investigating in detail, the role stacking faults play in increasing the capacity of the cells and potentially altering lithium-ion diffusion through the unit cells, synthetic methods can be tailored for optimization. Additionally, gaining a better understanding of how the block orientation plays on the electrochemical performance would build off previous work presented in Chapter II. Continuing to build off work presented in Chapters III and IV, investigating how to improve the electrochemical performance in W-R materials through chemical substitution and doping is a significant goal. This can be done through adding in substitutions that are more prone to distortions or lowering the potential in which the transition metals are reduced.

An additional method to investigate niobium-based materials is through optical microscopy. As noted above, many transition metals commonly used in battery materials are electrochromic, providing another method of probing the charge storage processes. Specifically, SECCM would be a high throughput method to investigate single particle lithium insertion mechanisms to identify particle morphology and size trends resulting in improved performances. Lastly, developing methods to investigate and model pseudocapacitive materials will greatly assist the field by providing more specific definitions of what pseudocapacitance is and what is occurring. Overall, these research projects can help answer important questions to further understand the structure-property relationships in high-rate niobium oxide materials, guiding design principles for next generation electrochemical energy storage materials.

6.9 References

(1) Evanko, B.; Boettcher, S. W.; Yoo, S. J.; Stucky, G. D. Redox-Enhanced Electrochemical Capacitors: Status, Opportunity, and Best Practices for Performance Evaluation. *ACS Energy Lett.* **2017**, *2* (11), 2581–2590. https://doi.org/10.1021/acsenergylett.7b00828.

(2) Griffith, K. J.; Wiaderek, K. M.; Cibin, G.; Marbella, L. E.; Grey, C. P. Niobium Tungsten Oxides for High-Rate Lithium-Ion Energy Storage. *Nature* **2018**, *559* (7715), 556–563. https://doi.org/10.1038/s41586-018-0347-0.

(3) Burns, J. C.; Stevens, D. A.; Dahn, J. R. In-Situ Detection of Lithium Plating Using High Precision Coulometry. *J. Electrochem. Soc.* **2015**, *162* (6), A959. https://doi.org/10.1149/2.0621506jes.

(4) Downie, L. E.; Krause, L. J.; Burns, J. C.; Jensen, L. D.; Chevrier, V. L.; Dahn, J. R. In Situ Detection of Lithium Plating on Graphite Electrodes by Electrochemical Calorimetry. *J. Electrochem. Soc.* **2013**, *160* (4), A588. https://doi.org/10.1149/2.049304jes.

(5) Vetter, J.; Novák, P.; Wagner, M. R.; Veit, C.; Möller, K.-C.; Besenhard, J. O.; Winter, M.; Wohlfahrt-Mehrens, M.; Vogler, C.; Hammouche, A. Ageing Mechanisms in Lithium-Ion Batteries. *J. Power Sources* **2005**, *147* (1), 269–281. https://doi.org/10.1016/j.jpowsour.2005.01.006.

(6) Ribière, P.; Grugeon, S.; Morcrette, M.; Boyanov, S.; Laruelle, S.; Marlair, G. Investigation on the Fire-Induced Hazards of Li-Ion Battery Cells by Fire Calorimetry. *Energy Environ. Sci.* **2012**, *5* (1), 5271–5280. https://doi.org/10.1039/C1EE02218K.

(7) Koçer, C. P.; Griffith, K. J.; Grey, C. P.; Morris, A. J. Cation Disorder and Lithium Insertion Mechanism of Wadsley–Roth Crystallographic Shear Phases from First Principles. *J. Am. Chem. Soc.* **2019**, *141* (38), 15121–15134. https://doi.org/10.1021/jacs.9b06316.

(8) McDowell, M. T.; Lee, S. W.; Nix, W. D.; Cui, Y. 25th Anniversary Article: Understanding the Lithiation of Silicon and Other Alloying Anodes for Lithium-Ion Batteries. *Adv. Mater.* **2013**, *25* (36), 4966–4985. https://doi.org/10.1002/adma.201301795.

(9) Beaulieu, L. Y.; Eberman, K. W.; Turner, R. L.; Krause, L. J.; Dahn, J. R. Colossal Reversible Volume Changes in Lithium Alloys. *Electrochem. Solid-State Lett.* **2001**, *4* (9), A137. https://doi.org/10.1149/1.1388178.

(10) Rhodes, K.; Dudney, N.; Lara-Curzio, E.; Daniel, C. Understanding the Degradation of Silicon Electrodes for Lithium-Ion Batteries Using Acoustic Emission. *J. Electrochem. Soc.* **2010**, *157* (12), A1354. https://doi.org/10.1149/1.3489374.

(11) Higa, K.; Srinivasan, V. Stress and Strain in Silicon Electrode Models. *J. Electrochem. Soc.* **2015**, *162* (6), A1111. https://doi.org/10.1149/2.0091507jes.

(12) Woodford, W. H.; Chiang, Y.-M.; Carter, W. C. “Electrochemical Shock” of Intercalation Electrodes: A Fracture Mechanics Analysis. *J. Electrochem. Soc.* **2010**, *157* (10), A1052. https://doi.org/10.1149/1.3464773.

(13) Zhao, K.; Pharr, M.; Vlassak, J. J.; Suo, Z. Fracture of Electrodes in Lithium-Ion Batteries Caused by Fast Charging. *J. Appl. Phys.* **2010**, *108* (7), 073517. https://doi.org/10.1063/1.3492617.

(14) Cava, R. J. Lithium Insertion in Wadsley-Roth Phases Based on Niobium Oxide. *J. Electrochem. Soc.* **1983**, *130* (12), 2345. https://doi.org/10.1149/1.2119583.

(15) Saber, M.; Reynolds, C.; Li, J.; Pollock, T. M.; Van der Ven, A. Chemical and Structural Factors Affecting the Stability of Wadsley–Roth Block Phases. *Inorg. Chem.* **2023**, *62* (42), 17317–17332. https://doi.org/10.1021/acs.inorgchem.3c02595.

(16) Koçer, C. P.; Griffith, K. J.; Grey, C. P.; Morris, A. J. Lithium Diffusion in Niobium Tungsten Oxide Shear Structures. *Chem. Mater.* **2020**. https://doi.org/10.1021/acs.chemmater.0c00483.

(17) Allpress, J. G.; Wadsley, A. D. Multiple Phase Formation in the Binary System Nb_2O_5-WO_3 VII. Intergrowth of H-Nb_2O_5 and $WNb_{12}O_{33}$. *J. Solid State Chem.* **1969**, *1* (1), 28–38. https://doi.org/10.1016/0022-4596(69)90005-X.

(18) Allpress, J. G.; Sanders, J. V.; Wadsley, A. D. Multiple Phase Formation in the Binary System Nb_2O_5–WO_3. VI. Electron Microscopic Observation and Evaluation of Non-Periodic Shear Structures. *Acta Crystallogr. B* **1969**, *25* (6), 1156–1164. https://doi.org/10.1107/S0567740869003669.

(19) Li, T.; Nam, G.; Liu, K.; Wang, J.-H.; Zhao, B.; Ding, Y.; Soule, L.; Avdeev, M.; Luo, Z.; Zhang, W.; Yuan, T.; Jing, P.; Gyu Kim, M.; Song, Y.; Liu, M. A Niobium Oxide with a Shear Structure and Planar Defects for High-Power Lithium Ion Batteries. *Energy Environ. Sci.* **2022**, *15* (1), 254–264. https://doi.org/10.1039/D1EE02664J.

(20) Allpress, J. G.; Roth, R. S. The Effect of Annealing on the Concentration of Wadsley Defects in the Nb_2O_5-WO_3 System. *J. Solid State Chem.* **1971**, *3* (2), 209–216. https://doi.org/10.1016/0022-4596(71)90030-2.

(21) Iijima, S.; Kimura, S.; Goto, M. High-Resolution Microscopy of Nonstoichiometric $Nb_{22}O_{54}$ Crystals: Point Defects and Structural Defects. *Acta Crystallogr. A* **1974**, *30* (2), 251–257. https://doi.org/10.1107/S0567739474000519.

(22) Li, D. X.; Kuo, K. H. High-Resolution Electron Microscopy of Defects in $W_4Nb_{26}O_{77}$. *J. Solid State Chem.* **1985**, *56* (2), 236–240. https://doi.org/10.1016/0022-4596(85)90061-1.

(23) Preefer, M. B.; Saber, M.; Wei, Q.; Bashian, N. H.; Bocarsly, J. D.; Zhang, W.; Lee, G.; Milam-guerrero, J.; Howard, E. S.; Vincent, R. C.; Melot, B. C.; Ven, A. V. D.; Seshadri, R.;

Dunn, B. S. Multielectron Redox and Insulator-to-Metal Transition upon Lithium Insertion in the Fast-Charging, Wadsley-Roth Phase PNb_9O_{25}. **2020**. https://doi.org/10.1021/acs.chemmater.0c00560.

(24) Cheetham, A. K.; Allen, N.C. Cation Distribution in the Complex Oxide, $W_3Nb_{14}O_{44}$; a Time-of-Flight Neutron Diffraction Study. *J Chem Soc Commun* **1983**, 3.

(25) Yang, C.; Yu, S.; Ma, Y.; Lin, C.; Xu, Z.; Zhao, H.; Wu, S.; Zheng, P.; Zhu, Z. Z.; Li, J.; Wang, N. Cr^{3+} and Nb^{5+} Co-Doped $Ti_2Nb_{10}O_{29}$ Materials for High-Performance Lithium-Ion Storage. *J. Power Sources* **2017**, *360*, 470–479. https://doi.org/10.1016/j.jpowsour.2017.06.026.

(26) Fu, Q.; Liu, X.; Hou, J.; Pu, Y.; Lin, C.; Yang, L.; Zhu, X.; Hu, L.; Lin, S.; Luo, L.; Chen, Y. Highly Conductive $CrNb_{11}O_{29}$ Nanorods for Use in High-Energy, Safe, Fast Charging and Stable Lithium-Ion Batteries. *J. Power Sources* **2018**, *397* (July), 231–239. https://doi.org/10.1016/j.jpowsour.2018.07.020.

(27) Ok, K. M.; Halasyamani, P. S.; Casanova, D.; Llunell, M.; Alemany, P.; Alvarez, S. Distortions in Octahedrally Coordinated d^0 Transition Metal Oxides: A Continuous Symmetry Measures Approach. *Chem. Mater.* **2006**, *18* (14), 3176–3183. https://doi.org/10.1021/cm0604817.

(28) Saber, M.; Behara, S. S.; Van der Ven, A. Redox Mechanisms, Structural Changes, and Electrochemistry of the Wadsley–Roth $Li_xTiNb_2O_7$ Electrode Material. *Chem. Mater.* **2023**, *35* (22), 9657–9668. https://doi.org/10.1021/acs.chemmater.3c02003.

(29) Colby Evans, R.; Ellingworth, A.; Cashen, C. J.; Weinberger, C. R.; Sambur, J. B. Influence of Single-Nanoparticle Electrochromic Dynamics on the Durability and Speed of Smart Windows. *Proc. Natl. Acad. Sci. U. S. A.* **2019**, *116* (26), 12666–12671. https://doi.org/10.1073/pnas.1822007116.

(30) Evans, R. C.; Nilsson, Z. N.; Sambur, J. B. High-Throughput Single-Nanoparticle-Level Imaging of Electrochemical Ion Insertion Reactions. *Anal. Chem.* **2019**. https://doi.org/10.1021/acs.analchem.9b03487.

(31) Evans, R. C.; Nilsson, Z.; Balch, B.; Wang, L.; Neilson, J. R.; Weinberger, C. R.; Sambur, J. B. Quantifying Capacitive-Like and Battery-Like Charge Storage Contributions Using Single-Nanoparticle Electro-Optical Imaging. *ChemElectroChem* **2020**, *7* (3), 753–760. https://doi.org/10.1002/celc.201902011.

(32) Otten, R. A.; Nieto, K.; Schulze, M. C.; Prieto, A. L. Quantification of Electrode Pulverization Enabled through Operando Video Microscopy of an Electrodeposited Antimony Anode. *ACS Appl. Eng. Mater.* **2023**, *1* (11), 3062–3068. https://doi.org/10.1021/acsaenm.3c00521.

(33) Merryweather, A. J.; Schnedermann, C.; Jacquet, Q.; Grey, C. P.; Rao, A. Operando Optical Tracking of Single-Particle Ion Dynamics in Batteries. *Nature* **2021**, *594* (7864), 522–528. https://doi.org/10.1038/s41586-021-03584-2.

(34) Guo, Z.; Zhu, J.; Feng, J.; Du, S. Direct in Situ Observation and Explanation of Lithium Dendrite of Commercial Graphite Electrodes. *RSC Adv.* **2015**, *5* (85), 69514–69521. https://doi.org/10.1039/C5RA13289D.

(35) Wood, K. N.; Kazyak, E.; Chadwick, A. F.; Chen, K.-H.; Zhang, J.-G.; Thornton, K.; Dasgupta, N. P. Dendrites and Pits: Untangling the Complex Behavior of Lithium Metal Anodes through Operando Video Microscopy. *ACS Cent. Sci.* **2016**, *2* (11), 790–801. https://doi.org/10.1021/acscentsci.6b00260.

(36) Heo, S.; Cho, S. H.; Dahlman, C. J.; Agrawal, A.; Milliron, D. J. Influence of Crystalline and Shape Anisotropy on Electrochromic Modulation in Doped Semiconductor Nanocrystals. *ACS Energy Lett.* **2020**, *5* (8), 2662–2670. https://doi.org/10.1021/acsenergylett.0c01236.

(37) Granqvist, C. G. Electrochromics for Smart Windows: Oxide-Based Thin Films and Devices. *Thin Solid Films* **2014**, *564*, 1–38. https://doi.org/10.1016/j.tsf.2014.02.002.

(38) Ong, G. K.; Saez Cabezas, C. A.; Dominguez, M. N.; Skjærvø, S. L.; Heo, S.; Milliron, D. J. Electrochromic Niobium Oxide Nanorods. *Chem. Mater.* **2020**, *32* (1), 468–475. https://doi.org/10.1021/acs.chemmater.9b04061.

(39) Yao, D. D.; Rani, R. A.; O'Mullane, A. P.; Kalantar-Zadeh, K.; Ou, J. Z. High Performance Electrochromic Devices Based on Anodized Nanoporous Nb_2O_5. *J. Phys. Chem. C* **2014**, *118* (1), 476–481. https://doi.org/10.1021/jp410097y.

(40) Salles, P.; Pinto, D.; Hantanasirisakul, K.; Maleski, K.; Shuck, C. E.; Gogotsi, Y. Electrochromic Effect in Titanium Carbide MXene Thin Films Produced by Dip-Coating. *Adv. Funct. Mater.* **2019**, *29* (17), 1809223. https://doi.org/10.1002/adfm.201809223.

(41) Xu, X.; Martín-Yerga, D.; Grant, N. E.; West, G.; Pain, S. L.; Kang, M.; Walker, M.; Murphy, J. D.; Unwin, P. R. Interfacial Chemistry Effects in the Electrochemical Performance of Silicon Electrodes under Lithium-Ion Battery Conditions. *Small* **2023**, *19* (40), 2303442. https://doi.org/10.1002/smll.202303442.

(42) Bentley, C. L.; Kang, M.; Unwin, P. R. Scanning Electrochemical Cell Microscopy (SECCM) in Aprotic Solvents: Practical Considerations and Applications. *Anal. Chem.* **2020**, *92* (17), 11673–11680. https://doi.org/10.1021/acs.analchem.0c01540.

(43) Daviddi, E.; Gonos, K. L.; Colburn, A. W.; Bentley, C. L.; Unwin, P. R. Scanning Electrochemical Cell Microscopy (SECCM) Chronopotentiometry: Development and Applications in Electroanalysis and Electrocatalysis. *Anal. Chem.* **2019**, *91* (14), 9229–9237. https://doi.org/10.1021/acs.analchem.9b02091.

(44) Salzer, L. D.; Diamond, B.; Nieto, K.; Evans, R. C.; Prieto, A. L.; Sambur, J. B. Structure–Property Relationships in High-Rate Anode Materials Based on Niobium Tungsten Oxide Shear Structures. *ACS Appl. Energy Mater.* **2023**, *6* (3), 1685–1691. https://doi.org/10.1021/acsaem.2c03573.

(45) Augustyn, V.; Come, J.; Lowe, M. A.; Kim, J. W.; Taberna, P.-L.; Tolbert, S. H.; Abruña, H. D.; Simon, P.; Dunn, B. High-Rate Electrochemical Energy Storage through Li + Intercalation Pseudocapacitance. *Nat. Mater.* **2013**, *12* (6), 518–522. https://doi.org/10.1038/nmat3601.

(46) Costentin, C. Electrochemical Energy Storage: Questioning the Popular $v/v^{1/2}$ Scan Rate Diagnosis in Cyclic Voltammetry. *J. Phys. Chem. Lett.* **2020**, *11* (22), 9846–9849. https://doi.org/10.1021/acs.jpclett.0c02667.

(47) Ventosa, E. Why Nanoelectrochemistry Is Necessary in Battery Research? *Curr. Opin. Electrochem.* **2021**, *25*, 100635. https://doi.org/10.1016/j.coelec.2020.09.002.

(48) Roehrich, B.; Sepunaru, L. Impedimetric Measurement of Exchange Currents and Ionic Diffusion Coefficients in Individual Pseudocapacitive Nanoparticles. *ACS Meas. Sci. Au* **2024**. https://doi.org/10.1021/acsmeasuresciau.4c00017.

(49) Conway, B. E.; Gileadi, E. Kinetic Theory of Pseudo-Capacitance and Electrode Reactions at Appreciable Surface Coverage. *Trans. Faraday Soc.* **1962**, *58* (0), 2493–2509. https://doi.org/10.1039/TF9625802493.

(50) Vassiliev, S. Yu.; Levin, E. E.; Nikitina, V. A. Kinetic Analysis of Lithium Intercalating Systems: Cyclic Voltammetry. *Electrochimica Acta* **2016**, *190*, 1087–1099. https://doi.org/10.1016/j.electacta.2015.12.172.

(51) West, K.; Jacobsen, T.; Zachau-Christiansen, B.; Atlung, S. Determination of the Differential Capacity of Intercalation Electrode Materials by Slow Potential Scans. *Electrochimica Acta* **1983**, *28* (1), 97–107. https://doi.org/10.1016/0013-4686(83)85091-9.

(52) Conway, B. E. Two-Dimensional and Quasi-Two-Dimensional Isotherms for Li Intercalation and *Upd* Processes at Surfaces. *Electrochimica Acta* **1993**, *38* (9), 1249–1258. https://doi.org/10.1016/0013-4686(93)80055-5.

(53) Tsutomu Ohzuku, Ahsuhi Ueda. Phenomenological Expression of Solid-State Redox Potentials of $LiCoO_2$, $LiCo_{1/2}Ni_{1/2}O_2$, and $LiNiO_2$ Insertion Electrodes. *J. Electrochem. Soc.* **1997**, *144* (8).

(54) Angerstein-Kozlowska, H.; Klinger, J.; Conway, B. E. Computer Simulation of the Kinetic Behaviour of Surface Reactions Driven by a Linear Potential Sweep: Part I. Model 1-Electron Reaction with a Single Adsorbed Species. *J. Electroanal. Chem. Interfacial Electrochem.* **1977**, *75* (1), 45–60. https://doi.org/10.1016/S0022-0728(77)80071-5.

(55) Srinivasan, S.; Gileadi, E. The Potential-Sweep Method: A Theoretical Analysis. *Electrochimica Acta* **1966**, *11* (3), 321–335. https://doi.org/10.1016/0013-4686(66)87043-3.

(56) Gooding, J. J.; Mearns, F.; Yang, W.; Liu, J. Self-Assembled Monolayers into the 21st Century: Recent Advances and Applications. *Electroanalysis* **2003**, *15* (2), 81–96. https://doi.org/10.1002/elan.200390017.

(57) Bard, A. J.; Faulkner, L. R. *Electrochemical Methods : Fundamentals and Applications*; Wiley, 2001.

(58) Ulman, A. Formation and Structure of Self-Assembled Monolayers. *Chem. Rev.* **1996**, *96* (4), 1533–1554. https://doi.org/10.1021/cr9502357.

(59) Lenhard, J. R.; Murray, R. W. Chemically Modified Electrodes. 13. Monolayer/Multilayer Coverage, Decay Kinetics, and Solvent and Interaction Effects for Ferrocenes Covalently Linked to Platinum Electrodes. *J. Am. Chem. Soc.* **1978**, *100* (25), 7870–7875. https://doi.org/10.1021/ja00493a014.

APPENDEX 1: SUPPORTING INFORMATION FOR CHAPTER II

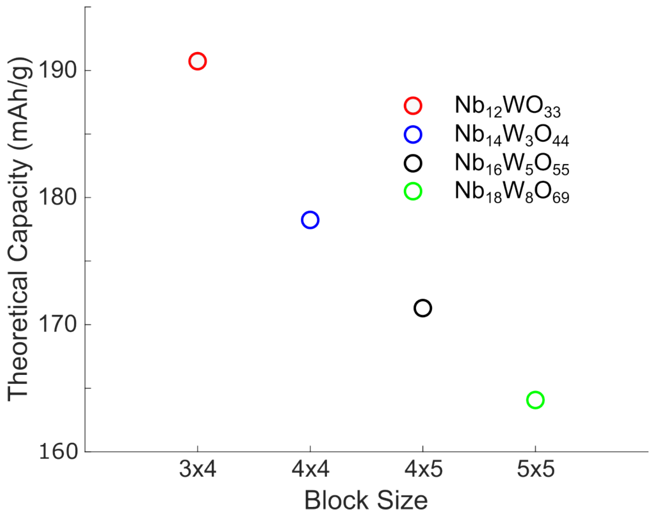

Figure A1.1. Theoretical capacity versus block size assuming 1 Li^+/TM for (3×4)-$Nb_{12}WO_{33}$, (4×4)-$Nb_{14}W_3O_{44}$, and (4×5)-$Nb_{16}W_5O_{55}$.

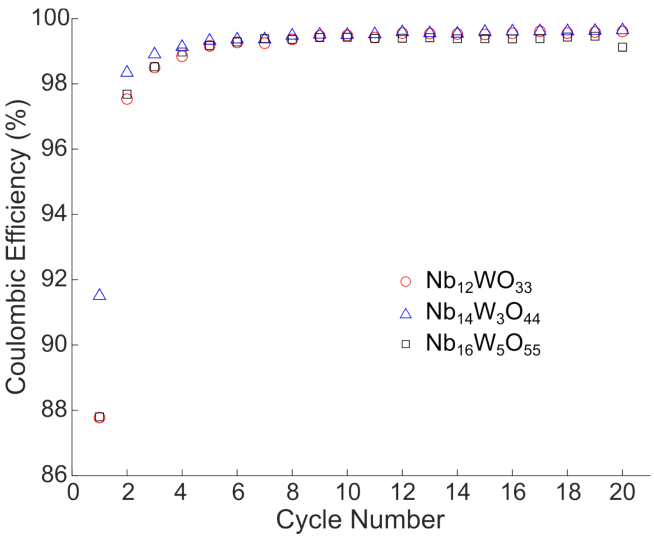

Figure A1.2. Comparison of coulombic efficiencies versus cycle number for (3×4)-$Nb_{12}WO_{33}$, (4×4)-$Nb_{14}W_3O_{44}$, and (4×5)-$Nb_{16}W_5O_{55}$.

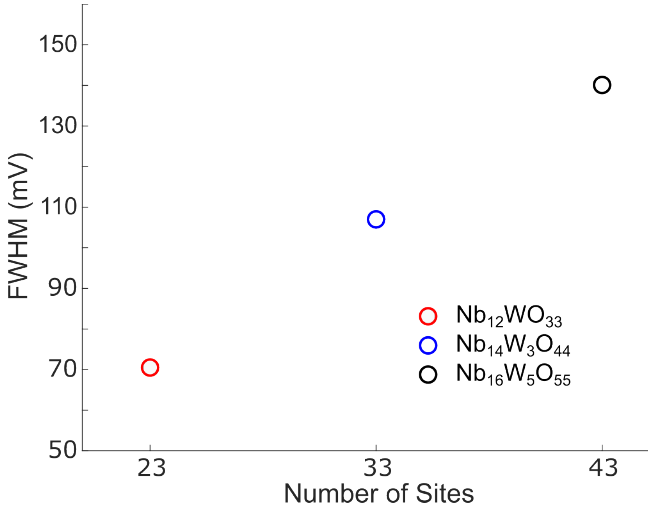

Figure A1.3. Full width at half maximum (FWHM) of the Region II peaks in Figure 2.2d-f of the main text versus the total number of Li-ion binding sites in the unit cell. The total number of sites was obtained from reference S1.

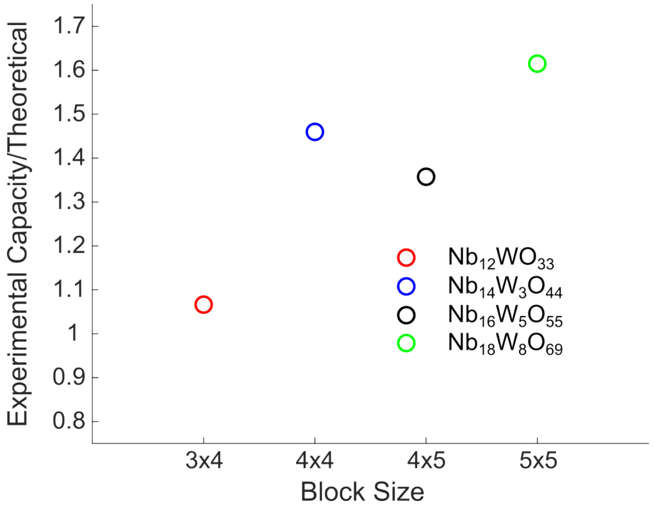

Figure A1.4. Ratio of experimental to theoretical capacity upon first discharge for (3×4)-$Nb_{12}WO_{33}$, (4×4)-$Nb_{14}W_3O_{44}$, (4×5)-$Nb_{16}W_5O_{55}$, and (5×5)-$Nb_{18}W_8O_{69}$. The data for (5×5)-$Nb_{18}W_8O_{69}$ was obtained from reference S2 at a rate of C/2.

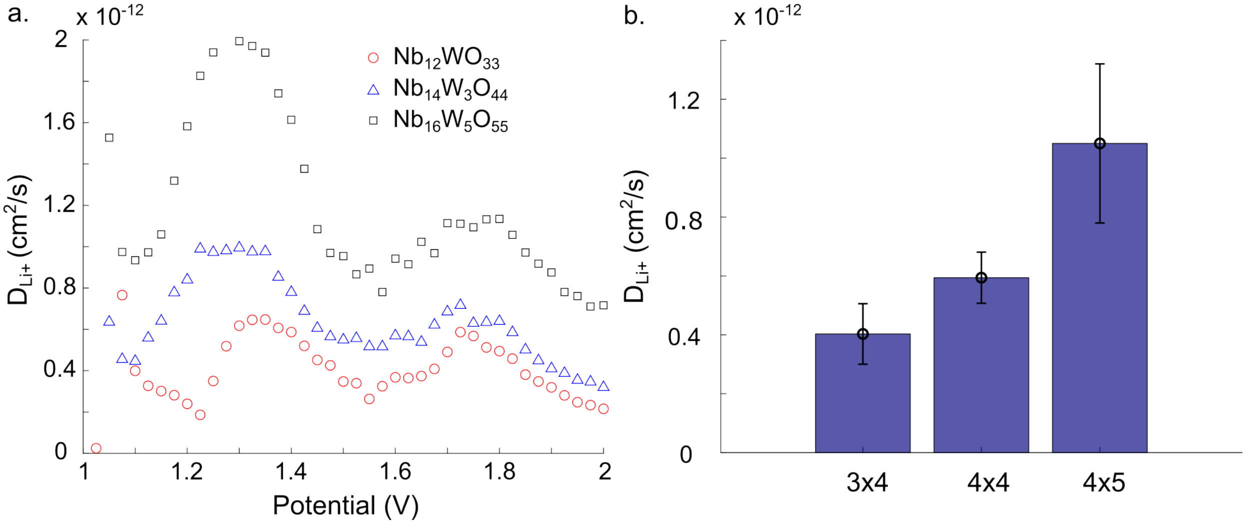

Figure A1.5. (a) D_{Li+} versus applied potential, as determined via PITT measurements for the anodic sweep. (b) Average D_{Li+} over the potential range of 1.4-1.6 V.

A1.1 REFERENCES

(S1) Koçer, C. P.; Griffith, K. J.; Grey, C. P.; Morris, A. J. Cation Disorder and Lithium Insertion Mechanism of Wadsley–Roth Crystallographic Shear Phases from First Principles. *J. Am. Chem. Soc.* **2019**, *141* (38), 15121–15134. https://doi.org/10.1021/jacs.9b06316.

(S2) Griffith, K. J.; Grey, C. P. Superionic Lithium Intercalation through 2×2 nm^2 Columns in the Crystallographic Shear Phase $Nb_{18}W_8O_{69}$. *Chem. Mater.* **2020**, *32* (9), 3860-3868. https://doi.org/10.1021/acs.chemmater.9b05403.

APPENDEX 2: SUPPORTING INFORMATION FOR CHAPTER III

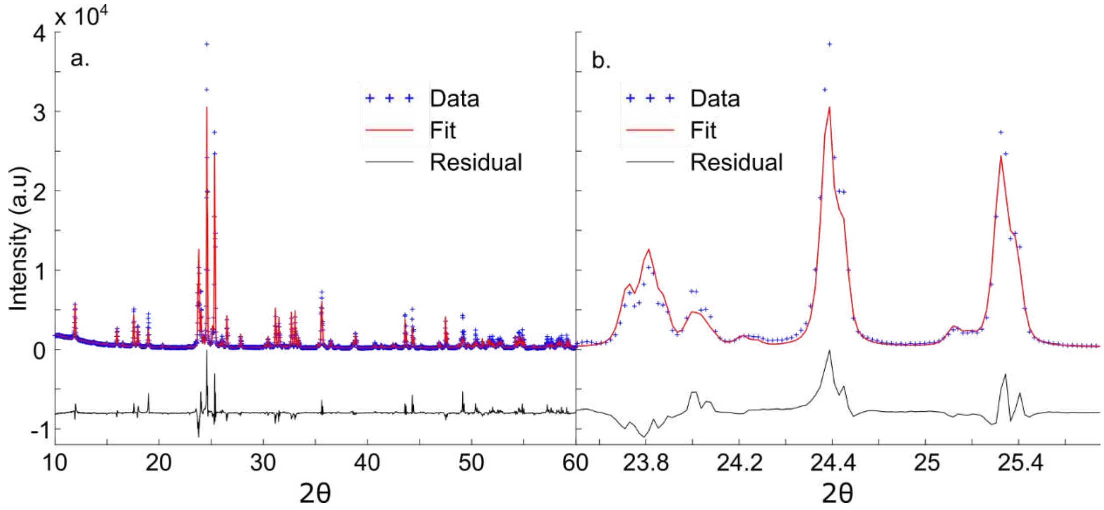

Figure A2.1. (a) Rietveld refinement of the slowly synthesized $Nb_{12}WO_{33}$ using the C2/m space group and refining the lattice parameters, with a R_{wp} of 20.452. (b) Zoomed in range highlighting the refinement more closely matches the peak positions than the models from the ICSD.

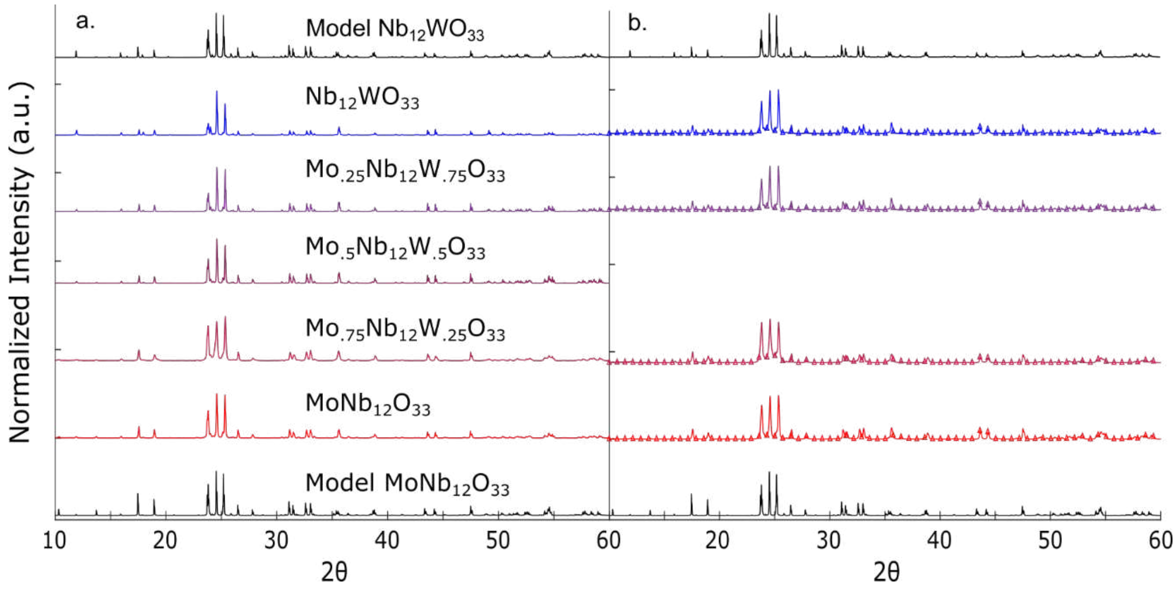

Figure A2.2. Comparison of simulated and experimental diffraction patterns for (a) $Mo_xNb_{12}W_{1-x}O_{33}$ and (b) D-$Mo_xNb_{12}W_{1-x}O_{33}$

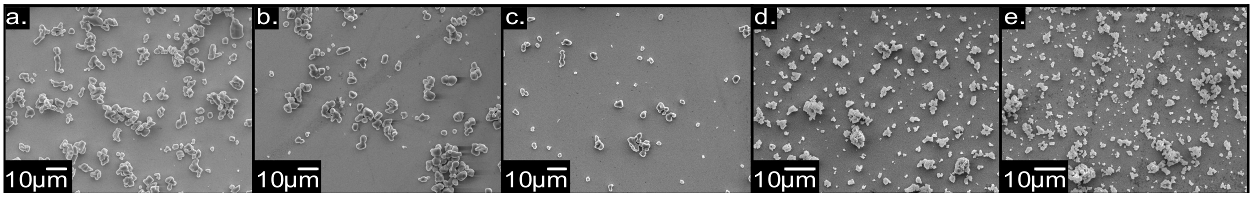

Figure A2.3. SEM images of (a) $Nb_{12}WO_{33}$, (b) $Mo_{.25}Nb_{12}W_{75}O_{33}$, (c) $Mo_{.5}Nb_{12}W_{.5}O_{33}$, (d) $Mo_{.75}Nb_{12}W_{.25}O_{33}$, and (e) $MoNb_{12}WO_{33}$

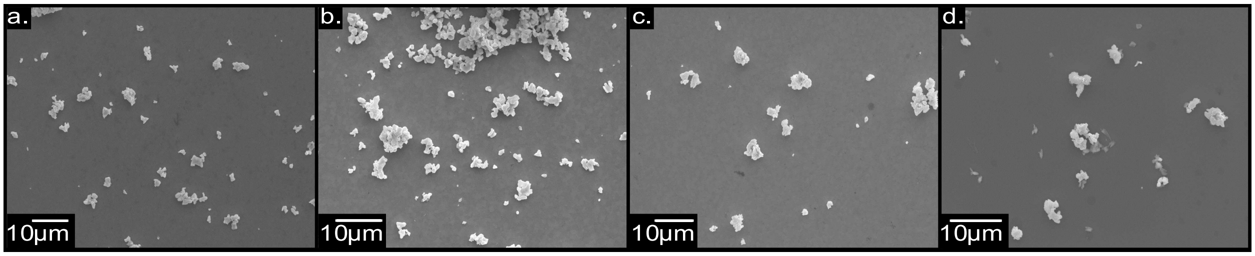

Figure A2.4. SEM images of (a) D-$Nb_{12}WO_{33}$, (b) D-$Mo_{.25}Nb_{12}W_{75}O_{33}$, (c) $Mo_{.75}Nb_{12}W_{.25}O_{33}$, and (d) $MoNb_{12}WO_{33}$

Table A2.1. Major and minor particle lengths for $Mo_xNb_{12}W_{1-x}O_{33}$

	$Nb_{12}WO_{33}$	$Mo_{.25}Nb_{12}W_{75}O_{33}$	$Mo_{.5}Nb_{12}W_{.5}O_{33}$	$Mo_{.75}Nb_{12}W_{.25}O_{33}$	$MoNb_{12}WO_{33}$
Major Axis (μm)	3.99 ±1.4 (n=106)	3.61±1.2 (n=93)	3.23±1.1 (n=92)	1.03±0.29 (n=101)	1.02±0.35 (n=100)
Minor Axis (μm)	2.61±0.68 (n=106)	2.68±0.77 (n=93)	2.35±0.72 (n=92)	0.77±0.22 (n=101)	0.78±0.29 (n=100)

Table A2.2. Major and minor particle lengths for D-$Mo_xNb_{12}W_{1-x}O_{33}$

	D-$Nb_{12}WO_{33}$	D-$Mo_{.25}Nb_{12}W_{75}O_{33}$	D-$Mo_{.75}Nb_{12}W_{.25}O_{33}$	D-$MoNb_{12}WO_{33}$
Major Axis (μm)	1.54 ± 0.52 $(n = 71)$	1.35 ± 0.44 $(n = 76)$	1.20 ± 0.38 $(n = 42)$	1.13 ± 0.30 $(n = 24)$
Minor Axis (μm)	0.993 ± 0.30 $(n = 71)$	0.940 ± 0.83 $(n = 76)$	0.855 ± 0.27 $(n = 71)$	0.711 ± 0.21 $(n = 24)$

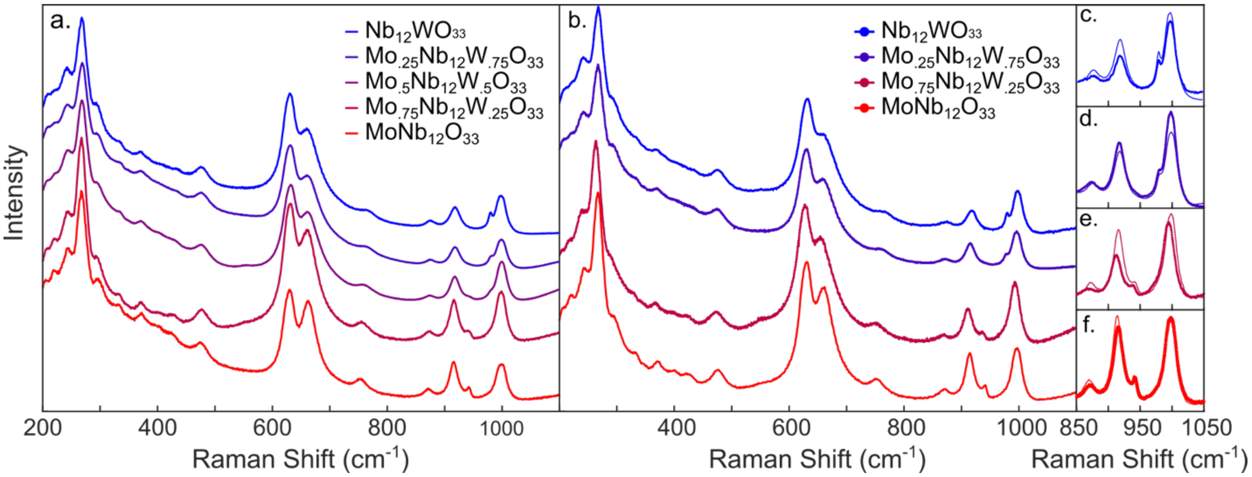

Figure A2.5. Comparison of Raman spectra for (a) $Mo_xNb_{12}W_{1-x}O_{33}$ and (b) D-$Mo_xNb_{12}W_{1-x}O_{33}$. (c-f) shows a focused Raman spectra comparing $Mo_xNb_{12}W_{1-x}O_{33}$ and D-$Mo_xNb_{12}W_{1-x}O_{33}$ (denoted by the dotted line)

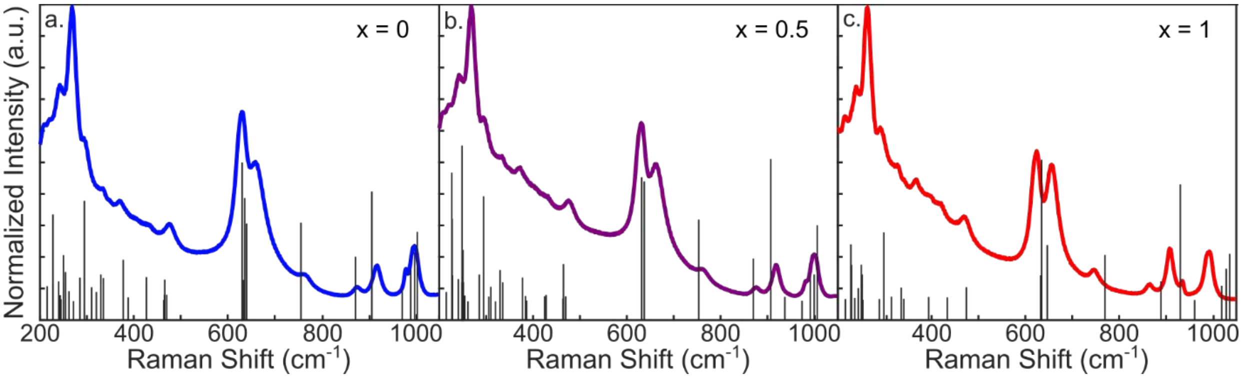

Figure A2.6. Experimental Raman spectra and simulated vibrational modes (black vertical sticks) for (a) $Nb_{12}WO_{33}$, (b) $Mo_{.5}Nb_{12}W_{.5}O_{33}$, and (c) $MoNb_{12}O_{33}$.

The low energy spectral region from 200 to 800 cm^{-1} contains a high density of simulated vibrational modes that could account for the prominent Raman peaks at approximately 270 cm^{-1}, 480 cm^{-1} and 630-650 cm^{-1}. Unfortunately, assigning these low frequency modes to specific lattice vibrations is challenging due to the structural complexity of the unit cells. The high frequency modes (800-1000 cm^{-1}) exhibit clearer atomic displacements (as shown in Figure A2.6), facilitating their assignment. Here we assign seven simulated vibrational modes to experimental Raman peaks in $Mo_xNb_{12}W_{1-x}O_{33}$ compounds for the first time (see Table A2.3). The simulated mode at 906 cm^{-1} corresponds to Nb-O-Nb vibrations along the block edge, specifically O3, O4, O5, and O6 (Figure A2.7). All compounds exhibit peaks in this region due to the common 12 Nb atoms in the unit cell. Similarly, the simulated mode at 998 cm^{-1} can be assigned to block center Nb-O-Nb vibrations involving O8, O9, and O11.

Some experimental Raman modes remain unassigned or appear significantly shifted from the theoretically predicted values, especially for $MoNb_{12}O_{33}$. Nearly all experimentally observed Raman peaks in Figure A2.6 can be linked to lattice vibrations except for the prominent peak at 650 cm^{-1}. This peak appears in all compounds, indicating the feature is not specific to Mo or W atoms. Hence, we suspect that this feature is likely associated with Nb-O vibrations in the block center.

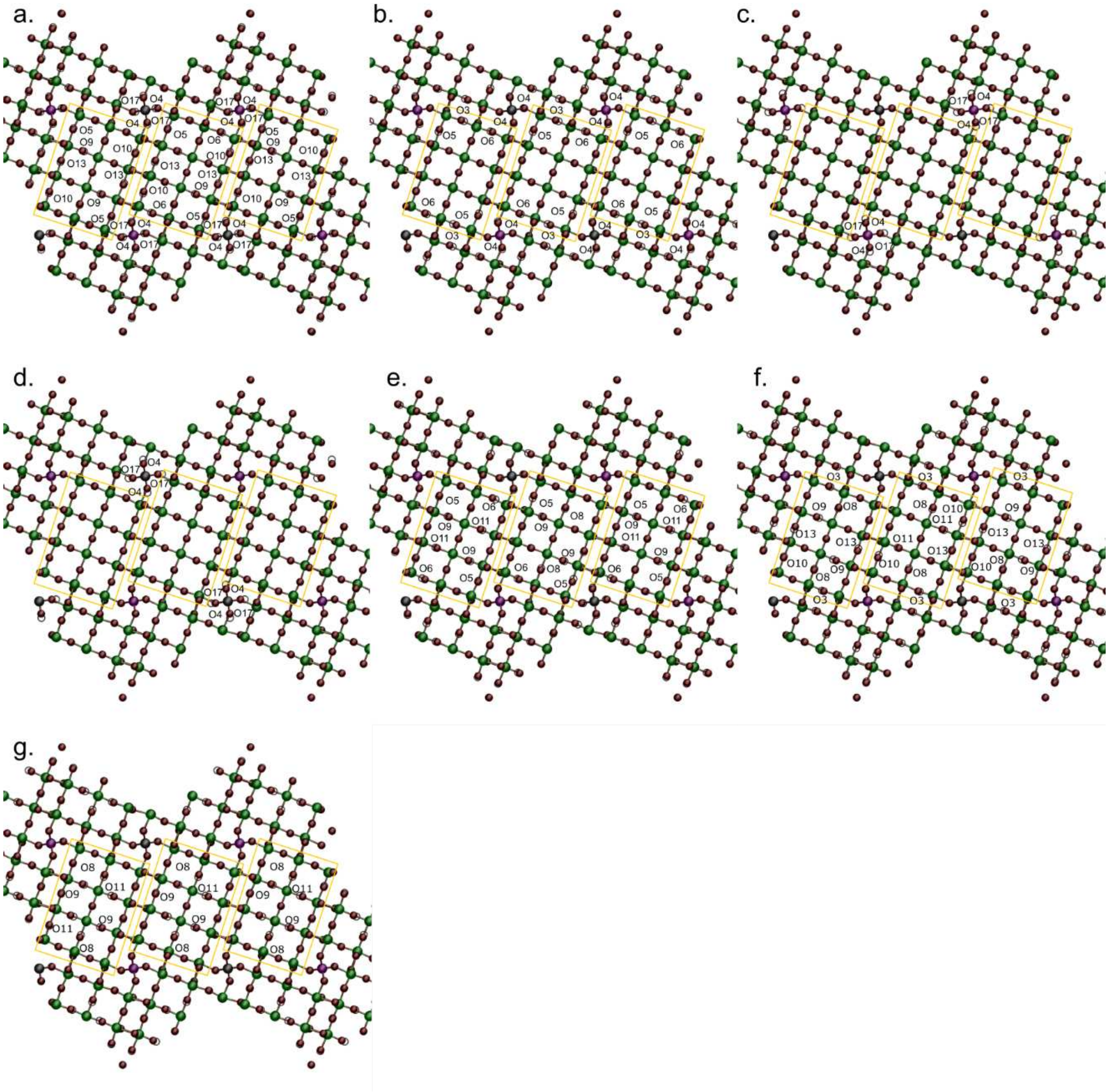

Figure A2.7. Assigned vibrational modes for the simulated Raman spectra (a) 256, (b) 258, (c) 262, (d) 263, (e) 266, (f) 271, and (g) 273.

Table A2.3. Assigned computational Raman vibrational modes for $Mo_{.5}Nb_{12}W_{.5}O_{33}$

Mode #	Raman Shift (cm^{-1})	Primary Atoms Involves	Description
256	869	O4, O17	Primarily vibrations around tetrahedra
258	906	O3, O5, O6	Block center vibrations
262	936	O4, O17	Oxygen vibration around Mo
263	972	O4, O17	Oxygen vibration around W
266	990	O5, O6, O9, O11	Mixed block edge and center vibrations
271	998	O3, O9, O10, O13	Mixed block edge and center vibrations
273	1004	O8, O9, O11	Block center vibrations

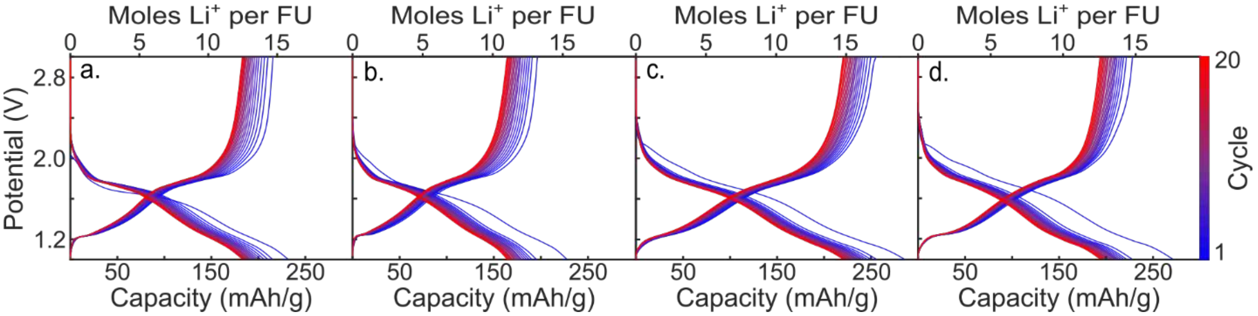

Figure A2.8. Constant Current plots at a rate of C/3 for (a) D-Nb$_{12}$WO$_{33}$, (b) D-Mo$_{.25}$Nb$_{12}$W$_{.75}$O$_{33}$, (c) D-Mo$_{.75}$Nb$_{12}$W$_{.25}$O$_{33}$, and (d) D-MoNb$_{12}$O$_{33}$.

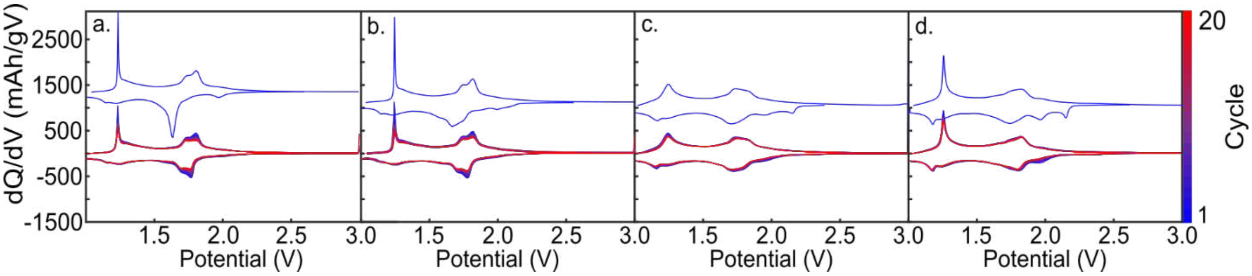

Figure A2.9. dQ/dV plots for (a) D-Nb$_{12}$WO$_{33}$, (b) D-Mo$_{.25}$Nb$_{12}$W$_{.75}$O$_{33}$, (c) D-Mo$_{.75}$Nb$_{12}$W$_{.25}$O$_{33}$, and (d) D-MoNb$_{12}$O$_{33}$.

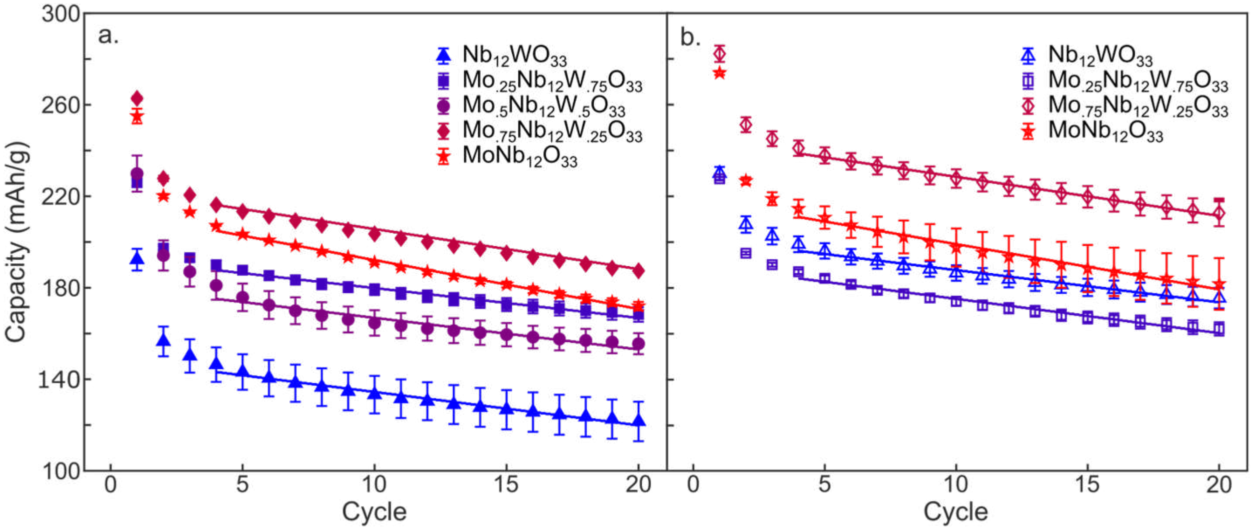

Figure A2.10. Shows the average discharge capacity for each cycle for (a) Mo$_x$Nb$_{12}$W$_{1-x}$O$_{33}$, the slope of capacity decay fits cycles 4-20 and is -1.60, -1.38, -1.57, -1.82, and -2.24 mAhg^{-1}/cycle for x=0, 0.25, 0.5, 0.75 and 1 respectively. (b) Shows the average discharge capacity for each cycle for D-Mo$_x$Nb$_{12}$W$_{1-x}$O$_{33}$, the slope of capacity decay fits cycles 4-20 and is -1.40, -1.49, -1.70, and -1.98 mAhg^{-1}/cycle for x=0, 0.25, 0.75 and 1 respectively.

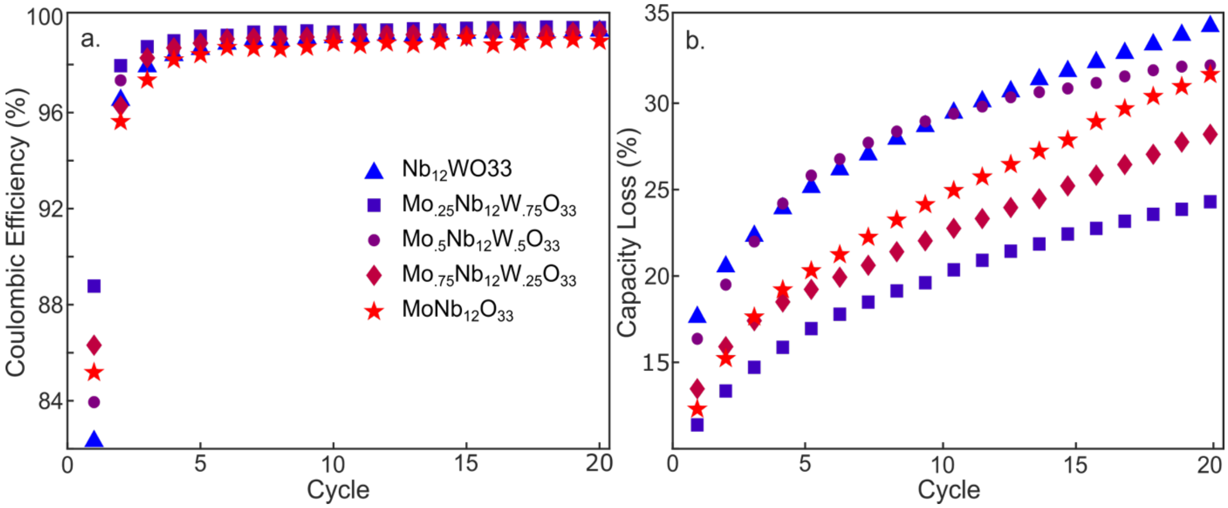

Figure A2.11. Average (a) coulombic efficiency of $Mo_xNb_{12}W_{1-x}O_{33}$ and (b) percent capacity loss relative to cycle 1.

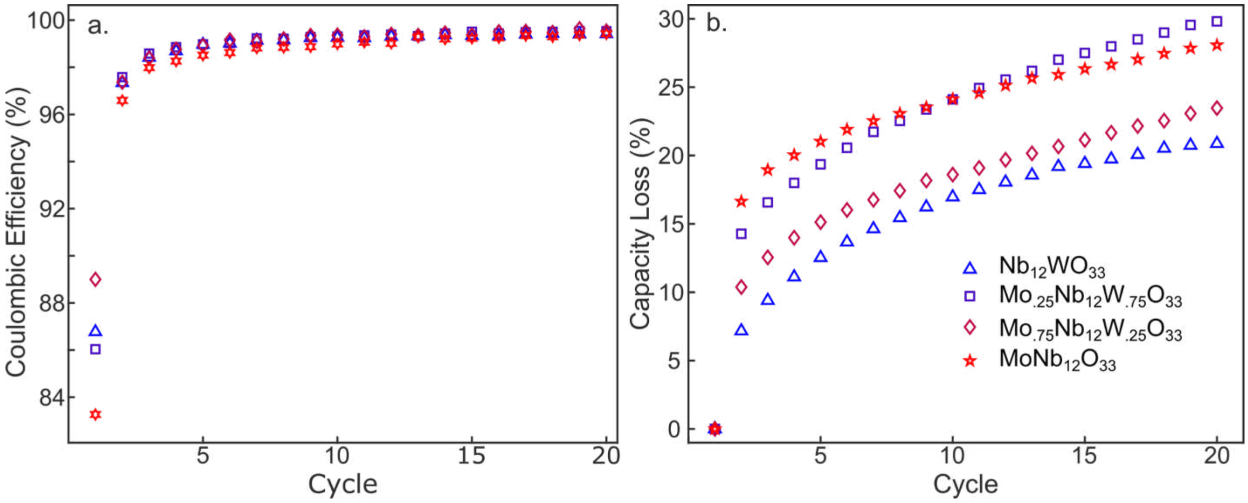

Figure A2.12. (a) Average coulombic efficiency for D-$Mo_xNb_{12}W_{1-x}O_{33}$. (b) Average capacity loss relative to the first cycle for D-$Mo_xNb_{12}W_{1-x}O_{33}$

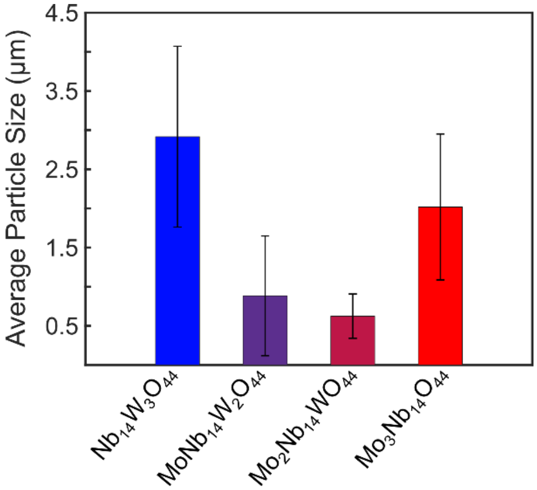

Figure A3.1. Particle size analysis of $Nb_{14}W_3O_{44}$ (n=42), $MoNb_{14}W_2O_{44}$ (n=105), $Mo_2Nb_{14}WO_{44}$ (n=104), and $Mo_3Nb_{14}O_{44}$ (n=110).

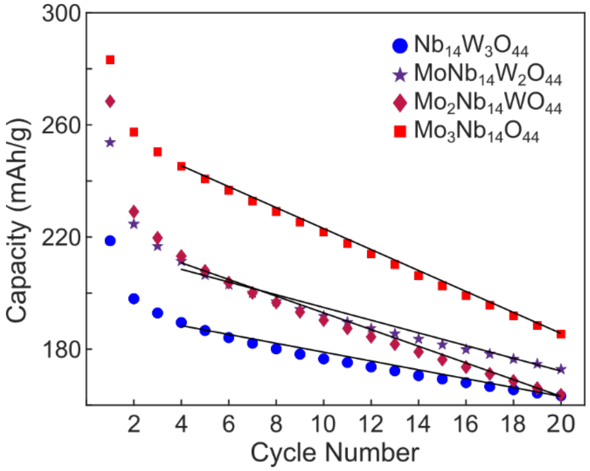

Figure A3.2.The average discharge capacity for each cycle for $Mo_xNb_{14}W_{3-x}O_{44}$, the capacity decay is denoted by the black line and is -1.58, -2.27, -2.98, and -3.74 $mAhg^{-1}$/cycle for x= 0, 1, 2, and 3 respectively.

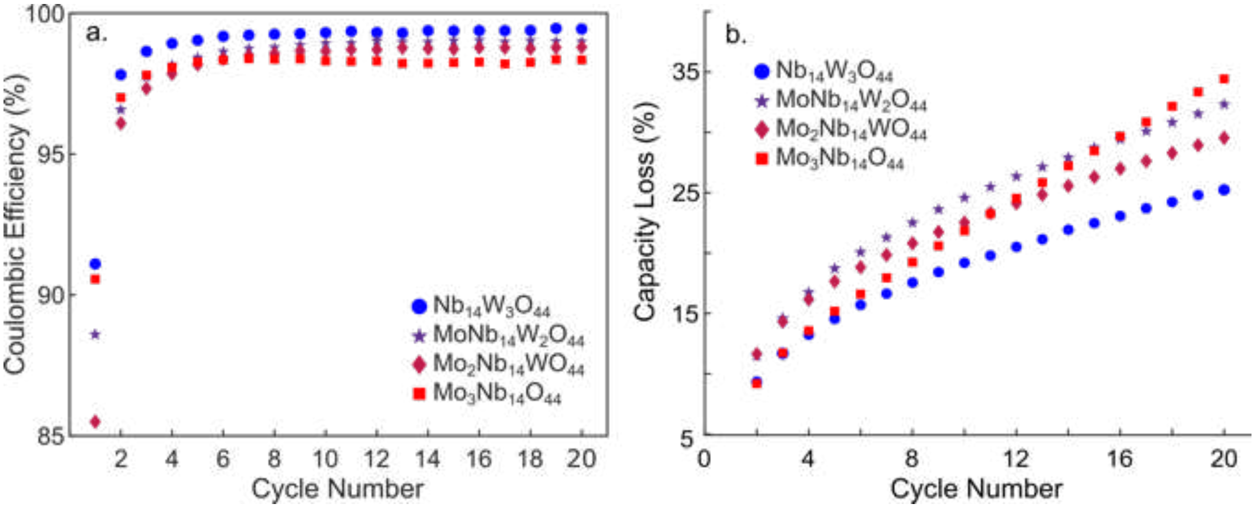

Figure A3.3. (a) Average coulombic efficiency for $Mo_xNb_{14}W_{3-x}O_{44}$. (b) Average capacity loss relative to the first cycle for $Mo_xNb_{14}W_{3-x}O_{44}$.

APPENDEX 4: SUPPORTING INFORMATION FOR CHAPTER V

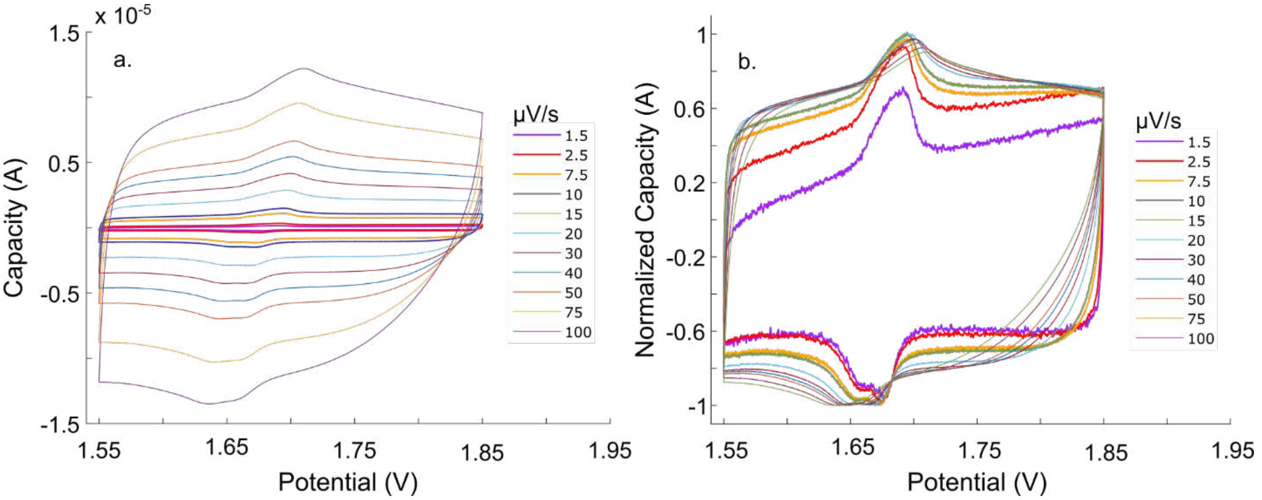

Figure A4.1. (a) Variable scan rate cyclic voltammetry on a T-Nb_2O_5 half-cell. (b) Cyclic voltammetry normalized with respect to the maximum cathodic current.

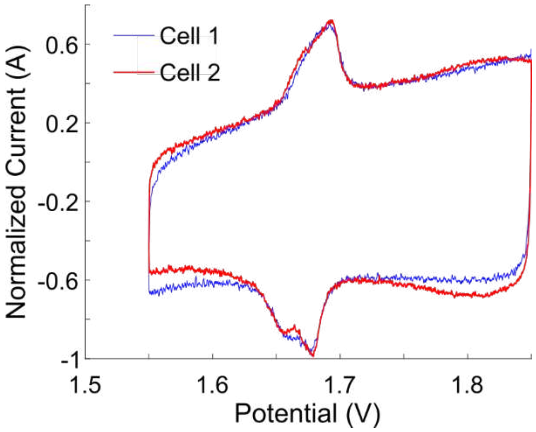

Figure A4.2. Comparison of two electrochemical cells cycled at 1.5 μV/s vs. Li/Li^+.

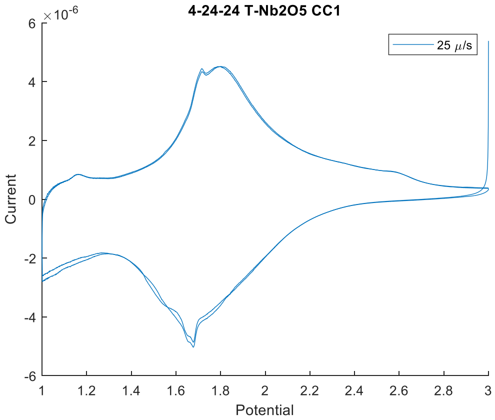

Figure A4.3. Cyclic voltammetry of a T-Nb_2O_5 cell with 1M $LiPF_6$ in EC:DMC electrolyte.